

**The Pennsylvania State University**  
**The Graduate School**

**STAR FORMATION ACROSS GALACTIC ENVIRONMENTS**

A Dissertation in  
The Department of Astronomy and Astrophysics  
by  
Jason Young

© 2012 Jason Young

Submitted in Partial Fulfillment  
of the Requirements  
for the Degree of

Doctor of Philosophy

December 2012

The dissertation of Jason Young was reviewed and approved\* by the following:

Caryl Gronwall  
Senior Scientist and Professor of Astronomy  
Dissertation Advisor, Chair of Committee

Michael Eracleous  
Professor of Astronomy

Robin Ciardullo  
Professor of Astronomy

Leisa Townsley  
Senior Scientist in Astronomy

Christopher House  
Associate Professor of Geosciences

Donald Schneider  
Department Head

\*Signatures are on file in the Graduate School.

# Abstract

I present here parallel investigations of star formation in typical and extreme galaxies. The typical galaxies are selected to be free of active galactic nuclei (AGN), while the extreme galaxies host quasars (the most luminous class of AGN). These two environments are each insightful in their own way; quasars are among the most violent objects in the universe, literally reshaping their host galaxies, while my sample of AGN-free star-forming galaxies ranges from systems larger than the Milky Way to small galaxies which are forming stars at unsustainably high rates. The current paradigm of galaxy formation and evolution suggests that extreme circumstances are key stepping stones in the assembly of galaxies like our Milky Way. To test this paradigm and fully explore its ramifications, this dual approach is needed.

My sample of AGN-free galaxies is drawn from the KPNO International Spectroscopic Survey. This H $\alpha$ -selected, volume-limited survey was designed to detect star-forming galaxies without a bias toward continuum luminosity. This type of selection ensures that this sample is not biased toward galaxies that are large or nearby. My work studies the KISS galaxies in the mid- and far-infrared using photometry from the IRAC and MIPS instruments aboard the Spitzer Space Telescope. These infrared bands are particularly interesting for star formation studies because the ultraviolet light from young stars is reprocessed into thermal emission in the far-infrared ( $24\mu\text{m}$  MIPS) by dust and into vibrational transitions features in the mid-infrared ( $8.0\mu\text{m}$  IRAC) by polycyclic aromatic hydrocarbons (PAHs). The work I present here examines the efficiencies of PAH and thermal dust emission as tracers of star-formation rates over a wide range of galactic stellar masses. I find that the efficiency of PAH as a star-formation tracer varies with galactic stellar mass, while thermal dust has a highly variable efficiency that does not systematically depend on galactic stellar mass.

Complementing this study of normal star-forming galaxies, my study of quasar host galaxies utilizes narrow- and medium-band images of eight Palomar-Green (PG) quasars from the WFPC2 and NICMOS instruments aboard the Hubble Space Telescope. Using images of a point-spread function (PSF) star in the same filters, I subtract the PSF of the quasar from each of the target images. The residual light images clearly show the host galaxies of the respective quasars. The narrow-band images were chosen to be

centered on the H $\beta$ , [O II], [O III], and Pa $\alpha$  emission lines, allowing the use of line ratios and luminosities to create extinction and star formation maps. Additionally, I utilize the line-ratio maps to distinguish AGN-powered line emission from star formation powered line emission with line-diagnostic diagrams. I find star formation in each of the eight quasar host galaxies in my study. The bulk star-formation rates are lower than expected, suggesting that quasar host galaxies may be dynamically more advanced than previously believed. Seven of the eight quasar host galaxies in this study have higher-than-typical mass-specific star-formation rates. Additionally, I see evidence of shocked gas, supporting the hypotheses presented in earlier works that suggest that AGN activity quenches star formation in its host galaxy by disrupting its gas reservoir.

# **Table of Contents**

# List of Figures

# **List of Tables**

# Acknowledgments

This work would not have been possible without the gracious direction, advice, and assistance of my numerous collaborators. In particular, I would like to thank Caryl Gronwall and Michael Eracleous for their near daily mentoring of my academic progress and intellectual development.

Additionally, I would like to thank my collaborators John Salzer and Jessica Rosenberg, as well as our colleague Matt Ashby, for their support and suggestions regarding the KISS project, and my collaborators Ohad Shemmer, Robin Ciardullo, Hagai Netzer, Dieter Lutz, and Eckhard Sturm for laying the groundwork that made the quasar host galaxy project possible. Also, I would like to give a special thanks to Robin Ciardullo for his willingness to field any question I have ever posed to him.

My collaborators and I are grateful to Kristin C. Peterson for editorial work in the preparation of this document and its constituent papers. I am also personally grateful to Kristin for supporting me through her advice and companionship during my work on these projects and their compilation into this thesis.

Support for this work was provided by NASA through grant number HST- GO-11222.01-A from the Space Telescope Science Institute, which is operated by AURA, Inc., under NASA contract NAS 5-26555.

This work made use of images and/or data products provided by the NOAO Deep Wide-Field Survey (Jannuzi and Dey 1999; Jannuzi et al. 2005; Dey et al. 2005), which is supported by the National Optical Astronomy Observatory (NOAO). NOAO is operated by AURA, Inc., under a cooperative agreement with the National Science Foundation.

IRAF is distributed by the National Optical Astronomy Observatories, which are operated by the Association of Universities for Research in Astronomy, Inc., under cooperative agreement with the National Science Foundation.

This research has made use of the NASA/IPAC Infrared Science Archive, operated by the Jet Propulsion Laboratory, California Institute of Technology, under contract with the National Aeronautics and Space Administration.

The Institute for Gravitation and the Cosmos is supported by the Eberly College of Science and the Office of the Senior Vice President for Research at the Pennsylvania State University.

# Chapter 1

## Nearby Star-Forming Galaxies in the Mid- and Far-Infrared

### 1.1 Introduction

In an effort to refine existing metrics of star-formation rate, I present an analysis of mid- and far-infrared photometry of 85 low-redshift H $\alpha$ -bright star-forming galaxies detected by the KPNO International Spectroscopic Survey (KISS; ?), also reported in ?. Because H $\alpha$  selection is not biased toward continuum-bright objects, the KISS sample spans a wide range of stellar masses ( $10^8$ – $10^{12} M_{\odot}$ ), H $\alpha$  luminosities ( $10^{39}$ – $10^{43}$  erg/s), mid-infrared  $8.0\mu\text{m}$  luminosities ( $10^{41}$ – $10^{44}$  erg/s), and [Bw-R] colors (1.0–2.4). Far-infrared luminosity in Spitzer MIPS bandpasses and mid-infrared polycyclic aromatic hydrocarbon (PAH) emission in Spitzer IRAC bandpasses indicate star formation. I improve empirical calibrations of two such bandpasses, IRAC  $8.0\mu\text{m}$  and MIPS  $24\mu\text{m}$ , as indicators of star-formation rate by fitting galactic luminosities in these bands against H $\alpha$ -derived extinction-corrected star-formation rates from the KISS sample, and find correlations that are broadly consistent with earlier work. I use novel multiwavelength data to find a strong, color-independent correlation between stellar mass and IRAC  $3.6\mu\text{m}$  luminosity. Using this surrogate for stellar mass, I measure mass-specific star-formation rates and find that [ $3.6\mu\text{m}$ ]–[ $24\mu\text{m}$ ] color may be used as a specific star-formation rate indicator, but [ $3.6\mu\text{m}$ ]–[ $8.0\mu\text{m}$ ] color shows at best a tenuous relationship with specific star-formation rate. Finally, I calibrate a mass dependence in the efficiency of  $8.0\mu\text{m}$  luminosity as a star-formation rate indicator.

### 1.2 Observations

#### 1.2.1 KISS H $\alpha$ -Selected Sample

The KISS field I focus on in this work is located in the NOAO Deep Wide Field Survey (NDWFS; ?) in Boötes (?). The KISS objects were selected from objective-prism spectra to have redshifts  $< 0.095$  and H $\alpha$  emission  $5\sigma$  above their median spectral continua. Objective-prism spectra are preferable to slit spectra for estimating total H $\alpha$  luminosity for extended objects because they capture all of the flux from the object rather than the

small fraction that would fall on a slit. A redshift (volume) limit rather than a magnitude limit ensures that the sample is not biased toward galaxies that are intrinsically bright in the continuum. One consideration of volume-limited H $\alpha$  surveys is a bias toward low extinction, however, as mentioned above, this bias makes extinction correction in the H $\alpha$  measurements less of a concern.

In the KISS Boötes field, 131 H $\alpha$  emission line objects were identified. The initial detections were followed up with higher resolution spectroscopy using the Hobby Eberly Telescope (HET), the KPNO 2.1 meter, the MDM 2.4 meter, and the Lick 3 meter telescopes (?????). Using the higher resolution spectra, 28 AGN and LINER galaxies were rejected through an extinction-corrected [N II] $\lambda$ 6583/H $\alpha$  versus [O III] $\lambda$ 5007/H $\beta$  line diagnostic diagram (??). Even though AGN hosts may be sites of star-forming activity, we are unable to disentangle AGN H $\alpha$  emission from that of star-forming activity, making the SFR measurement from such a galaxy unreliable. The 98 remaining objects are the sample from which this study is drawn. Metal abundance estimates were computed for all galaxies using emission-line ratios of strong lines by employing the coarse abundance method described in ? and ?. The H $\alpha$  luminosities referenced in this paper shall hereafter refer to H $\alpha$  luminosities that are measured from objective-prism data and are extinction-corrected using reddening estimates from follow-up spectra.

The greatest uncertainty in this calculation is the extinction correction. The objective-prism H $\alpha$  measurements are used to compute SFRs for the objects in this study because the objective-prism spectra encompass all of the light from the target. However, the Balmer Decrement ( $c_{H\beta}$ ) measurements from the follow-up spectra represent the extinction averaged over only the regions encompassed by the slit used in the follow-up spectra. Thus, this uncertainty has a systematic component in that, for objects of large angular size, where only a smaller fraction of the object was encompassed in the slit, the correction applied is more likely to deviate from the true value. To take this into account, the uncertainties in the H $\alpha$  measurements were weighted by the inverse of the angular size of their respective galaxies.

### 1.2.2 H $\alpha$ Star-Formation Rates

To calibrate mid- and far-infrared broadband photometry as star-formation rate indicators, I use extinction-corrected H $\alpha$  luminosity as a benchmark indicator. Because the stars contributing with any significance to the ionizing flux have short lifetimes (< 20 Myr), extinction-corrected H $\alpha$  luminosity is an indicator of current star formation and is relatively independent of star-formation history. ? provides an H $\alpha$  luminosity to SFR calibration using solar abundances and a Salpeter IMF (0.1 - 100 M $_{\odot}$ ):

$$\text{SFR} [\text{M}_{\odot}/\text{yr}] = 7.9 \times 10^{-42} L_{\text{H}\alpha} [\text{erg/s}] \quad (1.1)$$

$$\log (\text{SFR} [\text{M}_{\odot}/\text{yr}]) = -7.517 + \log (L_{\text{H}\alpha} [\text{L}_{\odot}]) \quad (1.2)$$

Other works, such as ?, study extinguished H $\alpha$  luminosity in linear combination with mid- or far-infrared luminosity. While extinguished H $\alpha$  samples the ultraviolet luminosity that is unabsorbed by dust, infrared indicators complement extinguished H $\alpha$

because they sample the ultraviolet luminosity that is absorbed by dust. With the proper calibration, a linear combination of the two can estimate total SFR as a sum of extinguished and unextinguished SFRs.

Because of the exquisite follow-up spectra available for this diverse sample of objects, I chose to use H $\alpha$  measurements corrected for extinction through the comparison of Balmer decrements to lab measured values, thereby turning the H $\alpha$  measurements into estimates of total SFR, both extinguished and unextinguished. I then use these total SFRs to evaluate mid- and far-infrared luminosities as indicators of total SFR.

### 1.2.3 Spitzer

The Spitzer data used in this project came from the Spitzer Deep Wide-Field Survey (?) and The Spitzer Program to Observe the NDWFS Field in Boötes (Soifer et al. 2004). Spitzer IRAC<sup>6</sup> 3.6 $\mu\text{m}$ , IRAC 4.5 $\mu\text{m}$ , IRAC 5.8 $\mu\text{m}$ , and IRAC 8.0 $\mu\text{m}$  mosaics from the Spitzer Deep Wide-Field Survey cover 86 of the 98 KISS star-forming galaxies; I detect 84 of these galaxies. The archival MIPS data from Soifer et al. (2004) provides this project with archival Spitzer MIPS<sup>7</sup> 24 $\mu\text{m}$  band coverage for 81 KISS star-forming galaxies; 79 are detected. Although MIPS 70 $\mu\text{m}$  and MIPS 160 $\mu\text{m}$  imaging exists for the KISS galaxies, the object-to-noise contrast is such that the detection rate is less than fifty percent in these bands. As a result, discussion of MIPS 70 $\mu\text{m}$  and MIPS 160 $\mu\text{m}$  photometry is not included in this work.

While photometry in all four IRAC bands and the MIPS 24 $\mu\text{m}$  band is tabulated in Table 1.1, I focus on IRAC 3.6 $\mu\text{m}$ , IRAC 8.0 $\mu\text{m}$ , and MIPS 24 $\mu\text{m}$  because of their relevance to star formation studies. Luminosity in the IRAC 8.0 $\mu\text{m}$  band comes from a combination of sources (?). The primary contributors in the IRAC 8.0 $\mu\text{m}$  band are vibrational emission lines of PAHs and the thermal tail of the old stellar population. Luminosity in the MIPS 24 $\mu\text{m}$  band, on the other hand, samples only thermal dust (?). The IRAC 3.6 $\mu\text{m}$  band is believed to sample primarily the thermal tail of the old stellar population. By studying these fluxes in tandem, I distinguish these different sources of luminosity and provide better calibrated SFR indicators. The IRAC 4.5 $\mu\text{m}$  and 5.8 $\mu\text{m}$  bands are less useful for this particular purpose because they contain weaker PAH bands and more contamination from the stellar continuum than the 8.0 $\mu\text{m}$  band.

While similar research has been conducted previously (??????), never before has such a statistically representative population been studied over so diverse a range of wavelengths and in tandem with high-resolution optical spectra. Moreover, unlike other studies sampling small regions within galaxies (??), the objective-prism spectra ensure that KISS SFRs are global SFRs and can be directly compared to integrated broadband SFR indicator candidates, such as IRAC 8.0 $\mu\text{m}$  and MIPS 24 $\mu\text{m}$  luminosities.

The Spitzer Deep Wide-Field Survey provides IRAC mosaics that are calibrated, co-added, and science ready. For the MIPS 24 $\mu\text{m}$  photometry I used archival Post Basic Calibrated Data mosaics. Typically, 2-4 Spitzer MIPS observations exist for each object, although a small number have only one observation. I co-added these observations to construct postage-stamp images after aligning them with centroiding software from the

---

<sup>6</sup>IRAC Data Handbook: <http://ssc.spitzer.caltech.edu/irac/dh/>

<sup>7</sup>MIPS Data Handbook: <http://ssc.spitzer.caltech.edu/mips/dh/>

NOAO Image Reduction and Analysis Facility (IRAF), and then performed photometry using apertures adjusted by hand to encompass each object simultaneously in the IRAC  $3.6\mu\text{m}$  and  $8.0\mu\text{m}$  and MIPS  $24\mu\text{m}$  images. The aperture radii ranged from  $8''$  to  $91''$  with an average of  $19''$ . Because the KISS galaxies are extended sources, I performed no aperture corrections.

This method of aperture determination has the significant advantage over automated methods that I was able to encompass unusually and irregularly shaped objects while still excluding nearby objects. Additionally, because the wavelength scale differs by almost a factor of ten between MIPS  $24\mu\text{m}$  and IRAC  $3.6\mu\text{m}$ , most automated methods would have difficulty with the varying PSF scales. As a check, I compared the IRAC magnitudes determined with this method to those listed in the catalog in ?; typically, they were within two tenths of a magnitude.

#### 1.2.4 NDWFS Optical Imaging

Because the KISS Boötes field was chosen to overlap with the heavily studied NDWFS Boötes field (?), deep optical images exist for the majority of the KISS galaxies in the Boötes field. In particular, this study makes use of Bw, R, and I band data for 79 of the 98 star-forming galaxies to calculate stellar masses for these galaxies using well-known mass-to-light relations (?), with which I calibrate  $3.6\mu\text{m}$  luminosity as a stellar mass indicator.

I performed photometry on these images using the same apertures that were used for photometry on the Spitzer IRAC and MIPS images. In some cases, the apertures needed to be re-tuned because the higher angular resolution of the NDWFS images revealed nearby contaminating objects, such as foreground stars and other galaxies, which were blended with a KISS galaxy in the Spitzer images. In these cases, I repeated the Spitzer photometry with the aperture adjusted to avoid the contamination.

Because the KISS galaxies are emission-line selected, emission lines potentially contribute a fair fraction of the light measured in the broadband optical photometry. This is problematic for my study because the mass-to-light relations in ? only apply to light from stellar populations. To remove the emission-line contamination from the broadband photometry, I scaled the H $\alpha$  equivalent widths measured in the object prism spectra along with the equivalent widths for H $\beta$ , [S II] $\lambda6717$ , [N II] $\lambda6583$ , [O II] $\lambda3727$ , and [O III] $\lambda5007$  lines measured in follow-up spectra (??) by the filter transmission at the redshifted wavelength of their respective lines, and then subtracted their contributions from the Bw and R band photometry.

### 1.3 Analysis

#### 1.3.1 Mid- and Far-Infrared Correlations with Total SFR

Because PAH features dominate non-stellar  $8.0\mu\text{m}$  flux by more than a factor of 100 above warm dust emission, and nearly a factor of 10 above the stellar continuum (??, see their Figures 8 and 10),  $8.0\mu\text{m}$  luminosity by itself ought to act as a SFR indicator (e.g., ?). To calibrate  $8.0\mu\text{m}$  luminosity as an indicator, I used extinction-corrected H $\alpha$

luminosity as a reference indicator.

Figure 1.1(a) plots H $\alpha$ -measured SFR against 8.0 $\mu\text{m}$  luminosity for the KISS galaxies that have 8.0 $\mu\text{m}$  measurements, along with an error-weighted linear regression determined using the method described in ?. The points have been color coded for log(O/H) + 12 metallicity when available from follow-up spectroscopy; a color key is to the right of the plot. The strength of this simple yet direct method of SFR estimation can clearly be seen.

There is, however, significant contamination from the red tail of the late-type stellar continuum in the 8.0 $\mu\text{m}$  bandpass. Because SED models (?) indicate that the IRAC 3.6 $\mu\text{m}$  bandpass samples the old stellar population almost exclusively, a dust-only 8.0 $\mu\text{m}$  luminosity can be created by using the 3.6 $\mu\text{m}$  luminosity to estimate and remove the stellar contribution in the 8.0 $\mu\text{m}$  band. As in ?, I adopt a coefficient  $\beta$  with a value of 0.232 to be the ratio of the stellar luminosity in the 8.0 $\mu\text{m}$  band to the stellar luminosity in the 3.6 $\mu\text{m}$  band. This ratio is derived from the Starburst99 model (?), and as the stellar SED in the mid-infrared regime is not a strong function of stellar age, it is likely to be a reasonable approximation. The dust-only 8.0 $\mu\text{m}$  luminosity shall henceforth be referred to as 8.0 $\mu\text{m}$  (dust). This technique is also used in other work (????), although the adopted value of  $\beta$  differs between authors, 0.22–0.29 in ? and 0.26 in ?, for instance. Figure 1.1(b) plots SFR against 8.0 $\mu\text{m}$  (dust), along with line of best fit. The fitted empirical relations are:

$$\log (\text{SFR} [\text{M}_\odot \text{ yr}^{-1}]) = \text{coeff} + \text{coeff} \times \log (\text{L}_{8.0\mu\text{m}} [\text{L}_\odot])) \quad (1.3)$$

$$\log (\text{SFR} [\text{M}_\odot \text{ yr}^{-1}]) = \text{coeff} + \text{coeff} \times \log (\text{L}_{8.0\mu\text{m}(\text{dust})} [\text{L}_\odot]) \quad (1.4)$$

I list the fitted coefficients for these relations in Table 1.2, along with the analogous coefficients from other work (??). Although different authors generally agree on the exponential coefficient for this relationship, typically giving it a value around 0.8–0.9, there is great disparity in the linear coefficient. It should be noted that the samples were collected by fairly different means. ? use a magnitude-limited sample favoring large galaxies. They note this, and mention that if several dwarf galaxies had been included in their fit, the slope of their relation would have been different—closer to the one found in this work. ? fit their relations to HII regions in M81, but PAH emission may be sensitive to filling factors and other physical effects that would make whole galaxy relations differ from relations based on individual HII regions. The filling factor phenomenon, as well as other physical explanations for problems with PAH emission as a direct SFR indicator, are discussed below. I note that the greater intrinsic scatter of my data, expected from a more uniform sample selection method, results in over a decade of variance in this relation.

Alternatively, some works (???) conclude that 24 $\mu\text{m}$  far-infrared thermal dust emission correlates with ionizing photons both on the galactic scale and on the scale of star-forming complexes. This band is longward of stellar emission, thus avoiding the somewhat model-dependent correction needed when examining 8.0 $\mu\text{m}$  luminosity. I plot in Figure 1.1(c) extinction-corrected H $\alpha$  SFR against 24 $\mu\text{m}$  luminosities for 81 KISS galaxies, along with a line of best fit. The best fit is:

$$\log (\text{SFR} [\text{M}_\odot \text{ yr}^{-1}]) = \text{coeff} + \text{coeff} \times \log (\text{L}_{24\mu\text{m}} [\text{L}_\odot]) \quad (1.5)$$

I chose not to use a piecewise indicator because these data do not unambiguously indicate any breaks in the luminosity relation seen in other work (??, etc.), possibly due to the greater intrinsic scatter in the KISS sample (as discussed below). Additionally, ? point out that one motivation for a piecewise indicator is the Luminous Infrared Galaxy (LIRG) mode of star formation at the high luminosity end ( $\text{L}_{24\mu\text{m}} \gtrsim 5 \times 10^{43} \text{ erg/s}$ ); this volume-limited sample has no LIRGs and only four objects with luminosities in this range, making a piecewise relation with a break at this luminosity both unwarranted and impossible to constrain in this study.

While there this relationship has over a decade of intrinsic scatter, the correlation holds over three decades in  $24\mu\text{m}$  luminosity. Nevertheless, I note that the relations I described involving  $24\mu\text{m}$  luminosity can only be expected to apply over the range of  $24\mu\text{m}$  luminosities studied here ( $10^{40}$  to  $7.5 \times 10^{43} \text{ erg/s}$ ).

### 1.3.2 Masses of KISS Galaxies

The correlations presented above are promising, but without greater insight into the nature of the galaxies being plotted it is unclear if they can be used as reliable SFR indicators for different kinds of galaxies across a range of redshifts. In particular, the total luminosity of a galaxy in any given band depends heavily on how large it is; a more massive galaxy will, on average, be brighter in all bands than a less massive galaxy. This is particularly problematic when trying to calibrate observational relations because even if the causal relationship between SFR and mid- and far-infrared luminosity did not exist, one might still expect the data described in the previous subsections to correlate with each other simply because larger galaxies are statistically more likely to be bright in  $\text{H}\alpha$  as well as in the mid- and far-infrared bands.

To this end, I measured the stellar masses of the KISS galaxies using well-established mass-to-light ratios (?). Using galactic stellar masses, I report mass-specific quantities in Section 1.3.3. The mass-to-light ratios in ? that I used are based on Sloan Digital Sky Survey photometry and population synthesis models. Using I band photometry from NDWFS data (?), I write the logarithmic stellar mass of a galaxy as its logarithmic I band luminosity plus a linear function of [B-R] color:

$$\log (\mathcal{M} [\text{M}_\odot]) = \log (\text{L}_I [\text{L}_\odot]) - 0.405 + 0.518 \times [\text{B} - \text{R}], \quad (1.6)$$

I note here that ? report that their optical mass-to-light relations have an uncertainty of  $\sim 0.1$  dex, and that I have propagated this uncertainty forward through the equations that follow.

Figure 1.2 represents with a black histogram the masses of the 81 KISS galaxies for which I band data exist. I have corrected the B and R magnitudes for the  $\text{H}\alpha$ ,  $\text{H}\beta$ ,  $[\text{N II}]$ ,  $[\text{S II}]$ ,  $[\text{O II}]$ , and  $[\text{O III}]$  lines based on the objective-prism and follow-up spectra, as described in Section 1.2.4. For comparison, I have represented with a red histogram the stellar masses of galaxies from the The GALEX Ultraviolet Atlas of Nearby Galaxies (?), also computed from broadband photometry using mass-to-light ratios from ?. The

masses of galaxies in ? are distributed into two categories, roughly corresponding to late- and early-type galaxies. As can be seen in Figure 1.2, the distribution of masses of KISS galaxies follows very closely that of the late-type galaxies from ?. Also included in Figure 1.2 are several Local Group galaxies; the KISS mass distribution spans these objects.

The use of optical magnitudes to track stellar mass requires at least two bands to allow for a color dependence, needed primarily because the luminosity of a stellar population changes with age. Because  $3.6\mu\text{m}$  is well into the Rayleigh-Jeans tail, even for M stars, the mid-infrared colors of stellar populations are not a strong function of age or metallicity, and are even less affected by dust obscuration and reddening than H and K bands. For these reasons, earlier work (???) used  $3.6\mu\text{m}$  images of their targets to remove the stellar contribution from their  $8.0\mu\text{m}$  images.

In Figure 1.3, I plot  $3.6\mu\text{m}$  absolute magnitudes against masses for all 81 KISS galaxies. The relationship between these quantities can be easily seen in the data. A best fit trend line yields the relation:

$$M_{3.6\mu\text{m}} = \text{coeff} + \text{coeff} \times \log(M [M_\odot]) \quad (1.7)$$

For the purposes of computing stellar masses from observations I rewrite this relation as:

$$\log(M [M_\odot]) = \text{coeff} + \text{coeff} M_{3.6\mu\text{m}} \quad (1.8)$$

Note that I chose to work with  $3.6\mu\text{m}$  absolute magnitudes rather than luminosities because the simpler conversion from easily measured and frequently quoted magnitudes to absolute magnitudes is likely to make this relationship appealing for future researchers.

This observationally affirms  $3.6\mu\text{m}$  magnitude as a marker of the stellar mass independent of a color correction. This relation is of the same level of precision as quoted by ?,  $\pm 0.2$  dex in the near-infrared. At the high luminosity end, the data contain several outliers which deviate from the fit by as much as 1.5 dex, although close examination of Figure 1.3 will show that the majority of objects with masses up to  $10^{11}M_\odot$  remain within 0.2 dex.

One issue with such a calibration is the presence of the  $3.3\mu\text{m}$  PAH feature in the IRAC  $3.6\mu\text{m}$  band. The strong and relatively scatter-free correlation seen in Figure 1.3 indicates that this PAH feature is either weak or scales consistently with galactic stellar mass. Dust models (??) as well as observations (???) indicate that the  $3.3\mu\text{m}$  feature is weak, supporting the former view.

With this relation in mind, I use  $3.6\mu\text{m}$  absolute magnitudes as a surrogate for stellar mass hereafter. Doing so allows me to compute masses for the KISS galaxies for which I do not have optical NDWFS photometry. Additionally, by using  $3.6\mu\text{m}$  absolute magnitudes I avoid using masses with uncertainties compounded from three different photometric measurements (Bw, R, and I).

### 1.3.3 Analysis of Mass-Dependent Quantities

As discussed in Section 1.3.2, galaxy masses are needed to determine the physical significances of the correlations presented in Section 1.3.1. ? utilize galaxy stellar masses by

comparing star-formation rate per stellar mass, or specific star-formation rate (SSFR), to mid-infrared colors for a subset of dwarf galaxies in the KISS sample. Specifically, they demonstrate that  $[3.6\mu\text{m}]-[8.0\mu\text{m}]$  color correlates poorly with SSFR.

I confirm these results using the expanded sample of KISS galaxies in Figure 1.4(a), where I plot SSFRs versus  $[3.6\mu\text{m}]-[8.0\mu\text{m}]$ . Because  $8.0\mu\text{m}$  luminosity tracks PAH emission and  $3.6\mu\text{m}$  luminosity tracks stellar masses, the  $[3.6\mu\text{m}]-[8.0\mu\text{m}]$  color is mass-specific PAH emission. This figure shows no trend whatsoever, with a Spearman rank-order coefficient of 0.033 and a 12% probability of correlation, suggesting that the PAH correlations presented in Section 1.3.1 are due to chiefly luminosities at all wavelengths scaling roughly with galaxy size. Likewise, I detect little or no trend in Figure 1.4(b), which compares SSFR with  $[3.6\mu\text{m}]-[24\mu\text{m}]$  color, with a Spearman rank-order coefficient of -0.017 and a 6% probability of correlation, suggesting that the warm dust correlations in Section 1.3.1 are also primarily driven by galaxy size. In order to better understand this issue, I must examine the efficiency of PAH emission as a star-formation indicator as a function of mass.

Using  $8.0\mu\text{m}$  (dust) as a measure of PAH emission and extinction-corrected  $\text{H}\alpha$  as a measure of total SFR, in Figure 1.5(a) I construct a PAH efficiency from the ratio of these luminosities and plot this ratio against  $3.6\mu\text{m}$  absolute magnitude as a surrogate for mass. This is physically motivated as there are many mechanisms that might cause PAH reprocessing to become less efficient in low mass or low metallicity galaxies, a selection of which are discussed below. Likewise, I use  $24\mu\text{m}$  per extinction-corrected  $\text{H}\alpha$  as a measure of warm dust reprocessing efficiency and plot this against  $3.6\mu\text{m}$  absolute magnitude in Figure 1.5(b).

In Figure 1.5(a), it is evident that high mass galaxies show a higher PAH to SFR ratio; they are more efficient at reprocessing ultraviolet light into PAH emission. This is consistent with the results of ?, who find that galaxies with brighter  $3.6\mu\text{m}$  luminosities have redder  $[3.6\mu\text{m}]-[8.0\mu\text{m}]$  colors. I calibrate PAH emission as a nonlinear SFR indicator with the following relation:

$$\log(L_{8.0\mu\text{m}(\text{dust})} [\text{L}_\odot]) - \log(L_{\text{H}\alpha} [\text{L}_\odot]) = \text{coeff} + \text{coeff} \times M_{3.6\mu\text{m}} \quad (1.9)$$

$$\log(\text{SFR} [\text{M}_\odot \text{ yr}^{-1}]) = \log(L_{8\mu\text{m}(\text{dust})} [\text{L}_\odot]) + \text{coeff} \times M_{3.6\mu\text{m}} + \text{coeff} \quad (1.10)$$

In contrast, there is very little relationship between the ratio of  $24\mu\text{m}$  luminosity to extinction-corrected  $\text{H}\alpha$  luminosity and this stellar mass surrogate,  $3.6\mu\text{m}$  luminosity, with a Spearman rank-order coefficient of .018 and a 6.6% probability of correlation. This ratio varies by more than two powers of ten across the sample, independent of mass, leading me to conclude that the efficiency of warm dust reprocessing is simply very different for different galaxies.

## 1.4 Discussion

The above correlations directly relating infrared luminosities to star-formation rates are statistically significant and broadly in agreement with earlier work (?????) (see Table 1.2). However, the correlations show a much larger relative scatter, especially in the MIPS  $24\mu\text{m}$  relations. Because of its  $\text{H}\alpha$  selection, KISS samples a broad range of star-

forming galaxies, especially when compared with the samples of earlier authors, such as ?, who selected bright galaxies, ? and ?, who studied star-forming regions in nearby galaxies, or ?, who studied dwarf galaxies. Although the direct relations presented here have more scatter, they are more representative of H $\alpha$ -bright galactic populations by virtue of drawing upon an H $\alpha$ -selected volume-limited sample. Moreover, the extinction-corrected objective-prism H $\alpha$  measurements give this sample total SFRs, while other work often samples only parts of the target galaxies with slit spectra.

Neither 24 $\mu\text{m}$  warm dust nor 8.0 $\mu\text{m}$  PAH correlate linearly with SFR (In log-log space, this means that their relationship does not have a slope of one.). This point has also been noted before (???) and does not come as a surprise for either calibration. The ultraviolet light that makes calibrating PAH emission as a SFR indicator possible also complicates the matter by destroying PAHs. ? and ? note that PAH emission is strongest on the rims of HII regions, and speculate that the radiation environment in the centers of star-forming complexes is simply too harsh for PAH molecules to survive. The exponential coefficient of less than one (around 0.9) in the PAH to SFR relation is, then, hardly unexpected as large galaxies with vigorous star formation are more likely to have many HII regions than one monolithic region. This would increase the surface area to volume ratio, and with it the PAH reprocessing efficiency. This line of reasoning is supported by the decreased scatter of low mass galaxies around the PAH efficiency trend line in Figure 1.5(a), as large galaxies are likely to contain large complex star-forming regions with diverse surface area to volume ratios.

? quite sensibly note that 8.0 $\mu\text{m}$  luminosity is sensitive to both star-formation history and metallicity since PAH molecules contain carbon. I speculate, as they suggest, that galaxies with higher metallicities or richer star-formation histories might be more PAH rich and have larger ultraviolet covering factors. This is in keeping with the findings in ?, and would also explain the trend in Figure 1.5(a), as there is an extremely tight mass-metallicity relationship.

Conversely, warm dust far-infrared emission is observed deeper in HII regions rather than near the edges as PAH emission. It is also not as sensitive to metallicity (?). The data show warm dust luminosity, via MIPS 24 $\mu\text{m}$  emission, to be nearly linear with SFR. In some respects this makes it a superior tracer of SFR, but, unlike PAH emission, mass-specific star-formation rates and mass-specific warm dust luminosity show no correlation, as seen in Figure 1.4(b). The wide variation in warm dust to H $\alpha$  ratios seems to indicate that the galaxies in this sample have diverse dust and star-forming complex characteristics, with warm dust behavior that is not easily characterized by two parameter models.

Interestingly, the greatest scatter in Figure 1.1(c) is seen at the high SFR end with high metallicity galaxies. ? speculate that any warm dust calibration would break down in the high luminosity regime due to self absorption, and possibly cooler SEDs. Additionally, as warm dust emission is found near the centers of HII regions, optical depth and line-of-sight play a role in efficiency determination of warm dust emission, unlike PAH emission which is found near the edges, so one would expect that large galaxies with complex star-formation structures (arms, etc.) might be more susceptible to variations in SFR/infrared relations due to geometric effects.

## 1.5 Conclusions

I find that, for an H $\alpha$ -selected sample of star-forming galaxies, both IRAC 8.0 $\mu\text{m}$  and MIPS 24 $\mu\text{m}$  luminosities track SFR as measured by H $\alpha$  emission. These calibrations broadly agree with earlier work (?????). The physical mechanisms for these indicators, ultraviolet-excited PAH vibrational line emission and warm dust thermal emission, are well understood.

I find that IRAC 3.6 $\mu\text{m}$  luminosity tracks stellar mass extremely well, and I calibrate this color-independent mass indicator. Using IRAC 3.6 $\mu\text{m}$  absolute magnitude as a surrogate for mass, I find that the efficiency with which PAH molecules reprocess ultraviolet to mid-infrared light is a function of galactic mass, with more massive galaxies being more efficient, a result which is broadly in agreement with ?. I calibrate this efficiency to absolute magnitude relation, making PAH emission more accessible as a robust SFR indicator. I also find that the efficiency with which warm dust reprocesses ultraviolet to far-infrared light varies widely from galaxy to galaxy.

In future work, fitting the SEDs of KISS galaxies will allow myself and my colleagues to characterize the typical SEDs of star-forming galaxies. Existing SED models are limited in wavelength; the panchromatic coverage of KISS will allow us to extend that range significantly. For example, the model presented in (?) does not extend past the near-infrared; with KISS I can estimate the PAH and dust contributions to the infrared SEDs of high-redshift star-forming galaxies observable with ALMA and Herschel.

Table 1.1. Spitzer IRAC &amp; MIPS Photometry

KISS ID	IRAC $3.6\mu m$ (mag)	IRAC $4.5\mu m$ (mag)	IRAC $5.8\mu m$ (mag)	IRAC $8.0\mu m$ (mag)	MIPS $24\mu m$ (mag)
2289	12.82	12.68	11.89	9.35	...
2291	13.90	13.80	13.21	10.75	...
2292	14.07	14.03	13.23	11.80	8.95
2293	13.41	13.21	12.37	9.70	5.53
2295	12.07	11.94	10.32	8.30	5.40
2297	15.05	14.83	13.98	12.93	8.29
2298	14.47	14.34	13.62	10.93	8.77
2299	14.82	14.63	13.89	11.85	9.25
2300	16.04	15.69	15.89	14.14	9.22
2302	15.32	15.40	14.17	13.65	10.50
2303	15.63	15.53	14.91	13.02	9.83
2304	14.39	14.26	13.77	11.62	9.55
2305	14.11	14.00	13.20	10.77	8.44
2306	12.91	12.87	11.57	9.80	7.49
2307	14.16	14.07	13.51	11.29	8.97
2308	13.60	13.50	12.92	10.66	8.56
2309	14.13	14.08	13.88	13.41	9.27
2313	13.58	13.49	12.62	10.39	8.14
2316	13.93	13.82	12.28	10.38	8.03
2318	15.05	14.88	14.48	12.04	8.91
2319	14.89	14.70	14.21	12.02	9.54
2320	13.19	13.13	12.28	11.06	8.21
2322	14.35	14.20	13.89	12.53	9.25
2323	13.96	13.86	12.96	10.96	8.33
2324	14.28	14.19	13.42	10.91	8.64
2325	13.16	13.07	11.96	10.30	7.93
2327	15.98	15.31	16.66	12.83	9.84
2328	14.22	13.92	13.63	11.38	9.14
2329	14.56	14.40	13.92	11.46	9.25
2330	14.28	14.17	13.58	10.95	9.01
2332	12.71	12.65	11.85	10.20	7.41
2333	14.46	14.35	13.77	11.38	9.03
2334	14.45	14.30	13.69	11.53	9.04
2335	11.89	11.80	10.55	8.62	5.65
2337	12.50	12.42	11.19	9.21	6.89
2338	15.79	15.52	14.81	12.64	7.79
2339	14.72	14.64	13.54	11.69	9.40
2344	12.96	12.97	12.01	10.78	7.72
2345	13.29	13.17	12.74	10.31	8.00
2346	15.46	15.44	14.29	13.50	9.00
2347	12.68	12.60	11.41	9.72	6.19
2348	11.97	11.89	10.36	8.44	5.87
2349	14.24	13.92	12.89	11.23	6.13
2353	13.33	13.18	12.37	9.73	7.12
2354	15.33	15.20	14.96	12.29	9.67

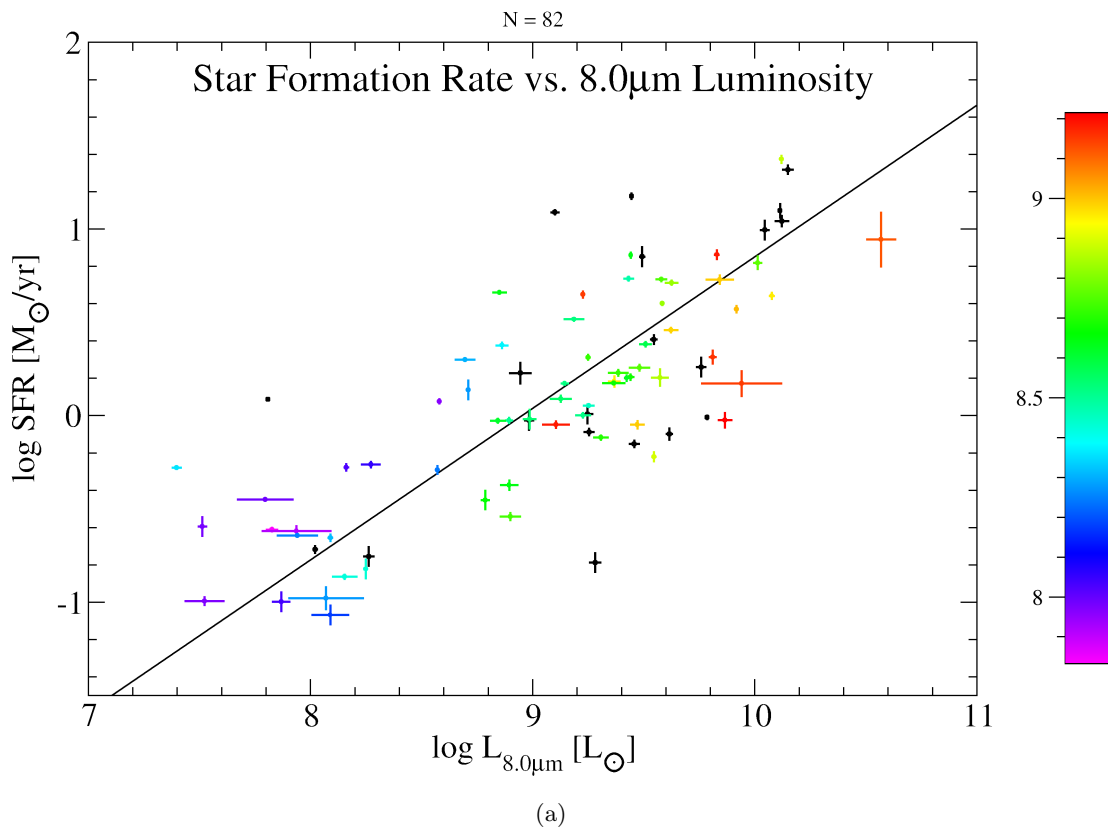


Figure 1.1: H $\alpha$ -derived SFR versus 8.0 $\mu\text{m}$  luminosity, with a line of best fit. Points are color coded by  $\log(\text{O/H}) + 12$  metallicity, with a color key to the right of the plot. Metallicity increases with 8.0 $\mu\text{m}$  luminosity and SFR, suggesting that larger galaxies are simply more luminous in all bands (discussed in Section 1.3.3).

Table 1.2. SFR Calibration Coefficients

Source	Indicator	a	b
This Work	$L_{8.0\mu m}$	coeff	coeff
This Work	$L_{8.0\mu m(dust)}$	coeff	coeff
?	$L_{8.0\mu m}$	-10.03±0.03	1.09 ±0.06
?	$L_{8.0\mu m}$	-7.9±0.3	0.87 ±0.03
This Work	$L_{24\mu m}$	coeff	coeff
?	$L_{24\mu m}$	-7.8±0.2	0.89±0.05
?	$L_{24\mu m}$	-8.20	0.81
?	$L_{24\mu m}$	-8.75	0.87
?	$L_{24\mu m}$	-7.3±0.5	0.82±0.01

<sup>2</sup> Listed above are the coefficients of a logarithmic fitting of the form  $\log \text{SFR}[\text{M}_\odot] = a + b \times \log L$ , where L is the indicator luminosity listed.

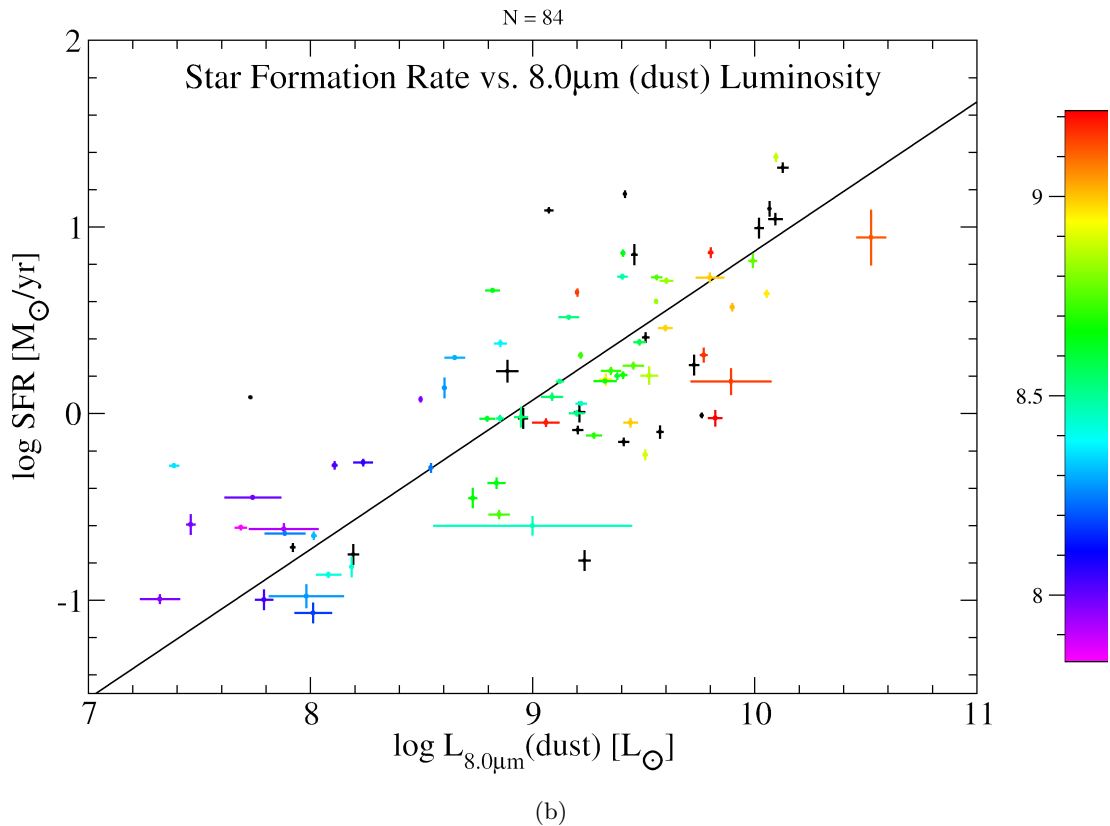


Figure 1.1: Same as Figure 1.1(a), but for 8.0μm (dust) luminosity

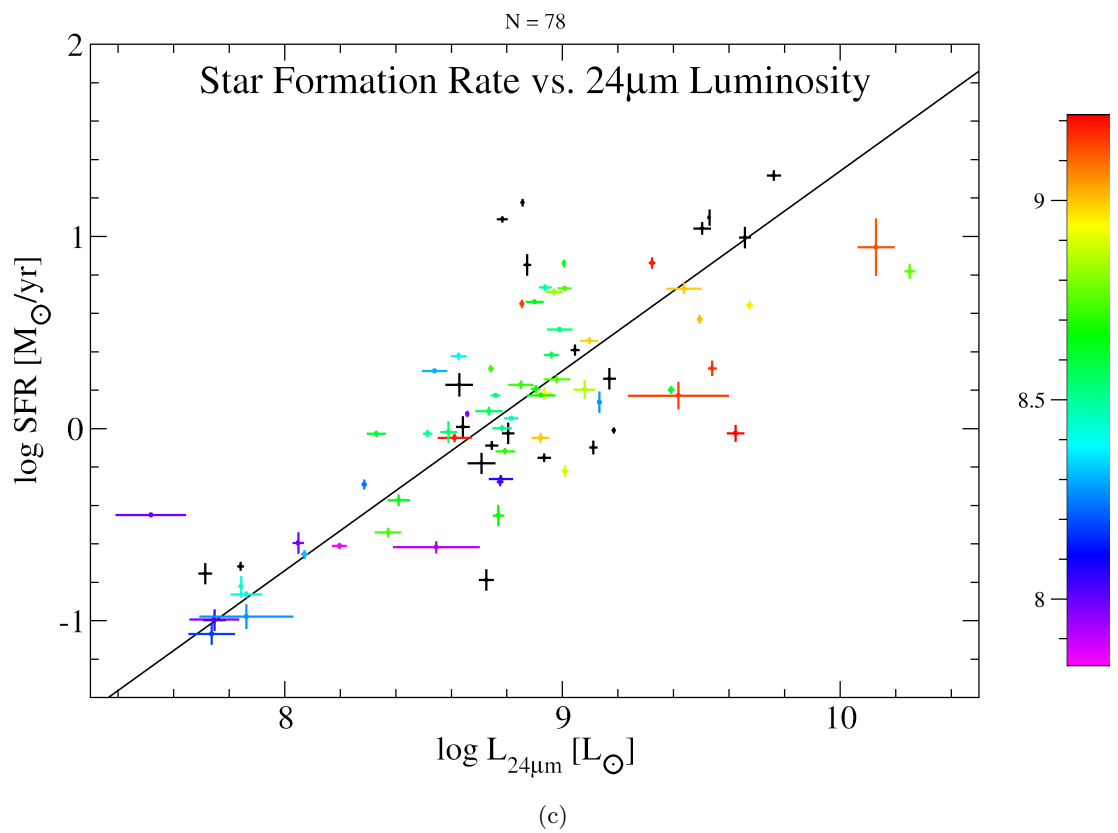


Figure 1.1: Same as Figure 1.1(a), but for  $24\mu\text{m}$  luminosity

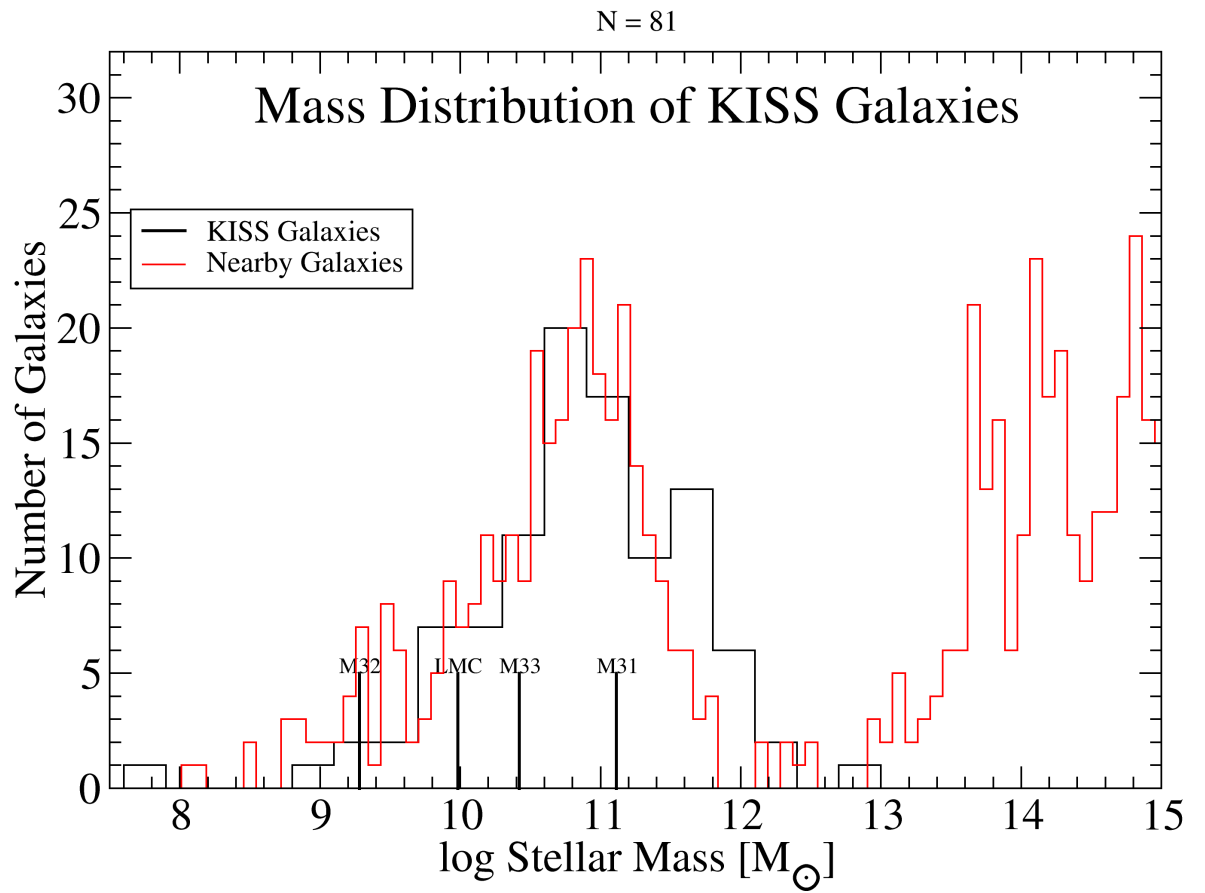


Figure 1.2: Distribution of stellar masses of the KISS galaxies (black) and Nearby Galaxies (red); note that M31 falls near the upper end of the distribution. Masses are derived from Bw, R, and I band NDWFS photometry (?) using mass-to-light relations described in ?.

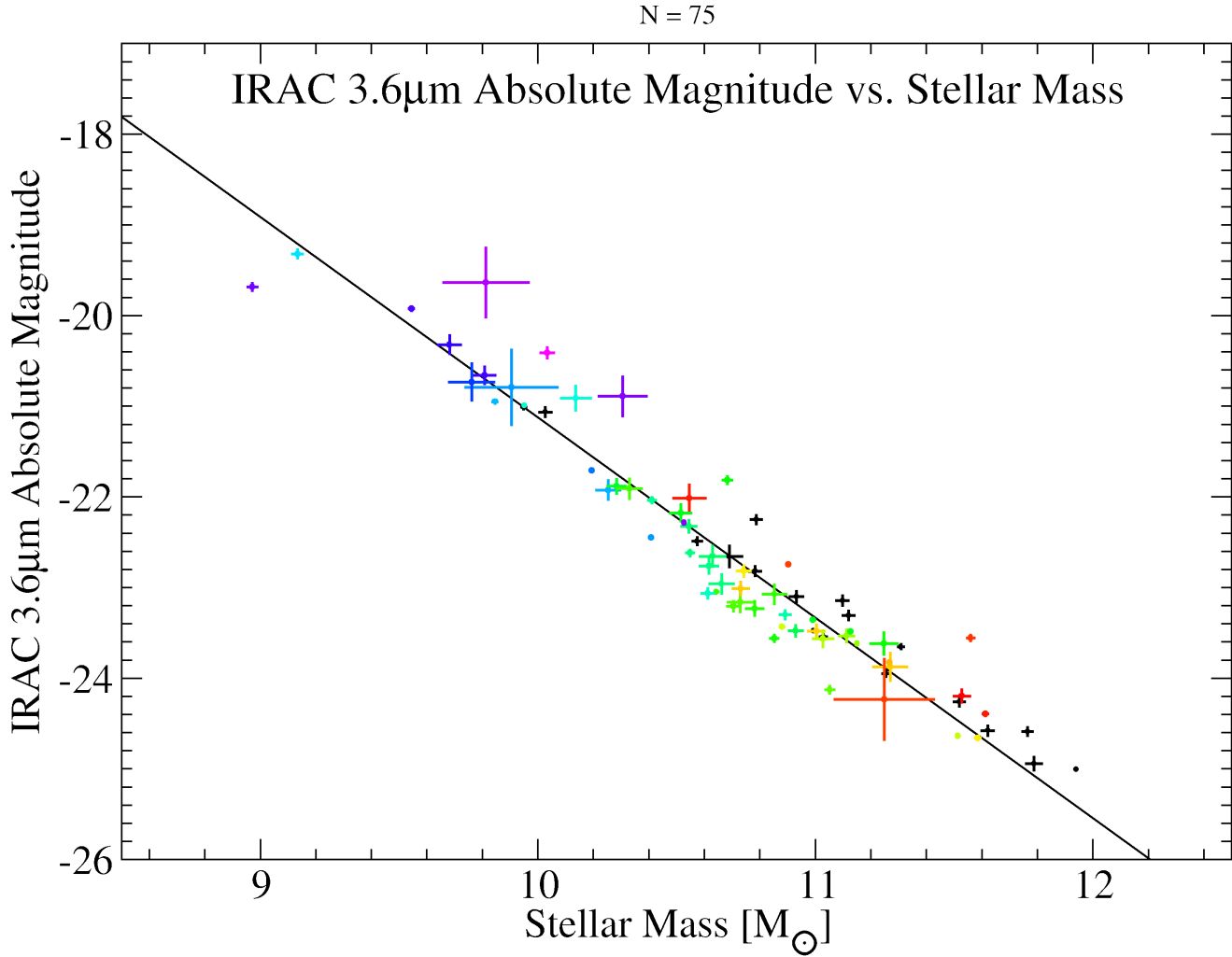


Figure 1.3: 3.6 $\mu$ m absolute magnitude versus stellar mass for 81 KISS galaxies. The high correlation justifies the use of 3.6 $\mu$ m luminosity as a surrogate for mass. Color indicates metallicity, as in earlier figures. Note that there is a strong mass/metallicity trend, but also that there are several exceptional galaxies with high metallicities but relatively low masses.

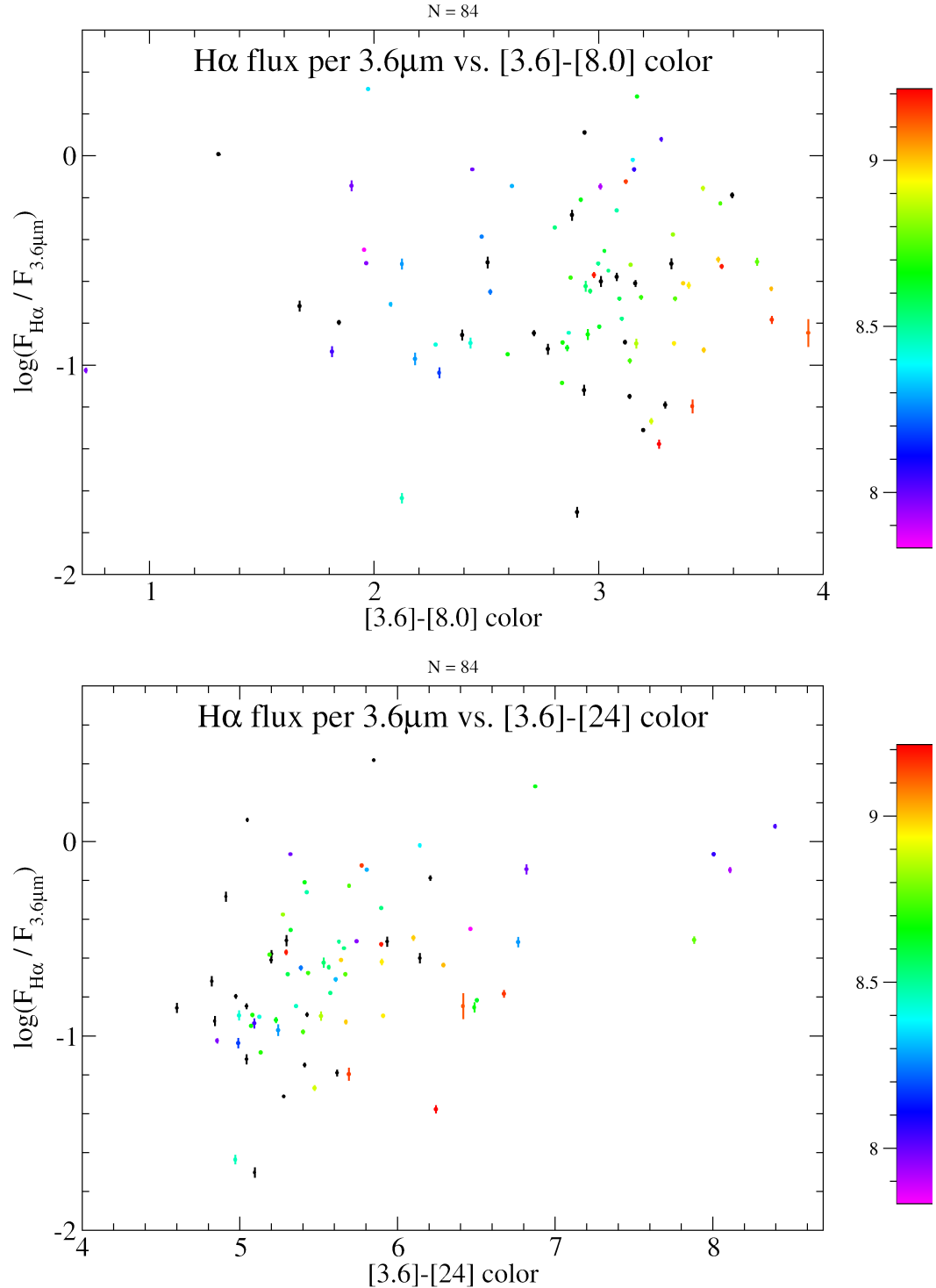


Figure 1.4: (a) Extinction-corrected H $\alpha$  per 3.6  $\mu\text{m}$  flux versus  $[3.6\mu\text{m}]-[8.0\mu\text{m}]$  color; essentially SSFR versus specific  $8.0\mu\text{m}$  luminosity. (b) Extinction-corrected H $\alpha$  per 3.6  $\mu\text{m}$  flux versus  $[3.6\mu\text{m}]-[24\mu\text{m}]$  color; essentially SSFR versus specific  $24\mu\text{m}$  luminosity per mass. Spearman rank-order analyses of (a) and (b), discussed in Section 1.3.3, indicate no trend whatsoever, implying that SFR to infrared luminosity relations are due to mass/size effects.

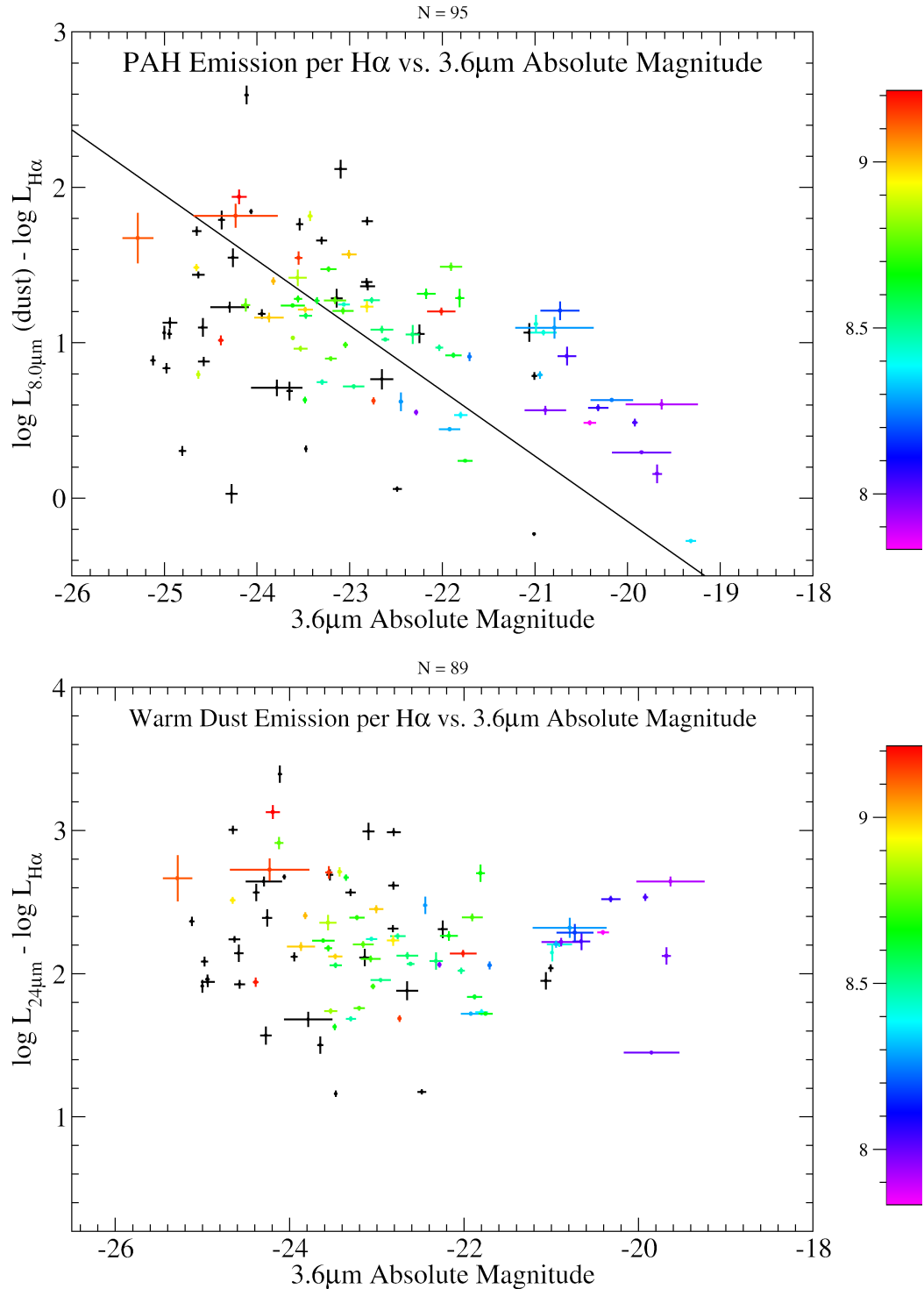


Figure 1.5: (a) 8.0 $\mu$ m luminosity per H $\alpha$  luminosity versus 3.6 $\mu$ m absolute magnitude, with a line of best fit. (b) 24 $\mu$ m luminosity per H $\alpha$  luminosity versus 3.6 $\mu$ m absolute magnitude.

# Chapter 2

## Emission Line Observations of Quasar Host Galaxies

### 2.1 Introduction

Studies of mature, inactive galaxies as well as numerical simulations suggest that AGN activity and star formation coincide, making quasar hosts the likely places for the assembly of the stellar populations seen in large elliptical galaxies. In this work, which is also presented in ?, I use calibrated narrow-band emission line ( $H\beta$  and  $Pa\alpha$ ) WFPC2 and NICMOS images as maps for total star formation rate. The main challenge in imaging quasar host galaxies is the separation of the quasar light from the galaxy light, especially in the case of  $z \approx 0.1$  quasars in WFPC2 images where the PSF radius closely matches the expected host galaxy scale radius. To this end, I present a novel technique for image decomposition and subtraction of quasar light, which I have validated through extensive simulations using artificial quasar+galaxy images. The other significant challenge in mapping and measuring star-forming regions is correcting for extinction, which I address using extinction maps created from the  $Pa\alpha/H\beta$  ratio. To determine the source of excitation, I utilize  $H\beta$  along with  $[O\text{ III}]\lambda 5007$  and  $[O\text{ II}]\lambda 3727$  images in diagnostic emission line ratio diagrams.

### 2.2 Sample Selection and Observing Strategy

My collaborators, with Dr. Eracleous as Principle Investigator, made the observations described herein before I joined the project. For the sake of completeness, I shall describe the methodology behind the observations, and then proceed to describe the analysis I developed to utilize the data they collected.

Aiming to select quasars that were likely to be hosted by galaxies with large, easily observable star-forming regions, we drew our target quasars from the Spitzer IRS sample of ? based on PAH emission, a suspected star-formation indicator (see Chapter 1 for details). Additionally, it was required that our targets have redshifts such that the  $Pa\alpha$  line fell within one of the narrow-band NICMOS filters. Among the objects that meet these criteria, the eight nearest ( $z < 0.15$ ) and brightest ( $V < 16.5$ ) quasars are the

targets for this project. These are listed in Table 2.1 along with their basic properties.

As discussed above, the galaxy to quasar contrast is likely to be highest in narrow-band images centered on emission lines. Our work focused on narrow-band images centered on Pa $\alpha$ , H $\beta$ , and [O III] $\lambda$ 5007, and [O II] $\lambda$ 3727 lines. By selection, the Pa $\alpha$  lines of our targets fell within one of the NICMOS narrow-band filters, listed in Table 2.2. To observe our targets in the optical bands, we used the WFPC2 camera. By using the ramp filters, we were able to select narrow-bands centered at the observed wavelengths of the desired emission lines. The ramp filters chosen are also listed in Table 2.2. Since the wavelength range of a ramp filter is set by the position of the object on the detector, most of our observations had to be made with one of the WF detectors rather than the PC detector. In several cases, one of the emission lines serendipitously fell within the FQUVN filter; this filter was used in these cases. In two cases our quasar had previously been observed for a similar project (?). For these objects, PG 0026+129 and PG 1307+085, we used archival [O III] $\lambda$ 5007 images.

Observing both the Pa $\alpha$  and H $\beta$  lines gives this project two fairly direct measures of star-formation rates, and allows me to correct for reddening. Also, relative intensities of the [O III] $\lambda$ 5007, [O II] $\lambda$ 3727, and H $\beta$  lines allows me to distinguish between line emission stimulated by star-forming activity and line emission stimulated by the ultraviolet radiation of the quasars themselves using the line ratio-diagnostic methods described in ?, and discussed further in Section 2.8.1.

Additionally, we observed the quasars in medium-band filters, giving us continuum images of the host galaxies. To obtain the infrared continuum images, we observed each quasar in a medium band filter centered on a wavelength near the Pa $\alpha$  line. Specifically, we used the NICMOS2 F237M and NICMOS3 F222M filters. Due to the failure of the NICMOS instrument, PG 1626+554 was not observed in the near-infrared. To obtain the optical continuum images of these quasar host galaxies, we observed each quasar in the F467M filter. This filter covers a line-free continuum between the [O II] $\lambda$ 3727 and H $\beta$  lines and provides suitable continuum for both lines. Additionally, the ? observations of PG 0026+129 and PG 1307+085 provided us with narrow-band (F588N) continuum images which capture the continuum near the [O III] $\lambda$ 5007 and H $\beta$  lines.

Because our targets are located at redshifts  $\approx 0.1$ , the plate scales of our images are typically 2 kpc  $\approx 1''$ . At this scale, these quasar host galaxies are generously contained within the fields of view of the PC, WF2-4, NICMOS2, and NICMOS3 detectors ( $36'' \times 36''$ ,  $80'' \times 80''$ ,  $19''2 \times 19''2$ , and  $51''2 \times 51''2$ , respectively).

Additionally, we observed the star GS 60200264 as a PSF template in a number of the filters. Due to the large number of filters used in this project, we could not observe the PSF star in each of the filters in which we observed the quasars; in some cases the PSF star was only observed in a filter close to the wavelength range used for a quasar.

The PC, WF, NICMOS2, and NICMOS3 detectors have plate scales of  $0''0455$ ,  $0''0995$ ,  $0''0756$ , and  $0''202845$ , respectively, leaving the PSF of the HST undersampled in all of our images. Sub-pixel dithering allows the recovering of some of this lost angular resolution using the method described in (??). We broke up each of our observations, both of the quasars and of the PSF star, into subexposures dithered by sub-pixel amounts using the default WFPC2-BOX pattern. This is a standard dither pattern with half-pixel sampling in both directions in the PC and WF detectors, and with dithers that

are large enough to optimize hot pixel and bad column rejection while minimizing the field of view loss. In all cases the subexposures were combined using the MultiDrizzle software package described in Section 2.3.1 and (??).

## 2.3 Reduction of Images

In addition to providing the raw data, STScI also processes WFPC2 data through a standard calibration pipeline (?). For this project, I chose to use the data products calibrated by this pipeline, after verifying that the reduction steps were suitable for my purposes. In most cases, this pipeline performs bias subtraction, dark subtraction, shutter correction, and writes photometric keywords to the image headers. The ramp filter images are an exception to this; prior to 2009, ramp filter images were not flat fielded by the standard pipeline. Following the instructions given by the instrument team <sup>8</sup>, I multiplied my ramp filter images by a flat field image taken in a nearby narrow- or medium-band filter. In practice, the narrow- or medium-band filters with wavelengths closest to those used by our ramp filter observations were the FQUVN and F467M filters.

The STScI pipeline is not, however, able to correct for charge transfer inefficiency in the WFPC2 instrument. The visible effect is that bright sources have a comet-like streak in the direction of charge transfer; this direction is different for different detectors, but remains the same between exposures. This phenomenon is well documented (??), but cannot be corrected in images. Instead, I note with an arrow the orientation of the streak in all of my images to avoid confusion with morphological features. Additionally, all of the image processing steps described in Sections 2.4, 2.6, and 2.7 were designed to exclude pixels near the streak.

STScI provides an analogous pipeline for NICMOS data (?); I chose to use post calibrated NICMOS data as well. This pipeline performed the bias subtraction, dark subtraction, and flat fielding, computed the noise and data quality images, and added photometric keywords to the image header. The only additional calibration step that I preformed was removing time variable quadrant bias or pedestal effect from my images, which I did using the pedsky software (?) provided by STScI. This effect is constant within a quadrant but varies from one readout to the next in an unpredictable way; it can be effectively removed using pedsky.

With the images reduced, the only processing step that remained before PSF subtraction was combining of the dithered subexposures, which I describe below.

### 2.3.1 MultiDrizzling

As noted above, to improve the sampling rate of the final images, the observations were dithered by subpixel increments, and the calibrated data products were combined using the MultiDrizzle software provided by STScI (??). MultiDrizzle regains the sampling of the HST PSF lost because of the large pixels of WFPC2. Optimally, MultiDrizzle combines subexposures at a sampling rate of twice their intrinsic pixel scale. For example, the PC detector has a pixel scale of  $0''.0455$  per pixel. MultiDrizzling PC images taken

---

<sup>8</sup>HST Calibration of LRF Data: [http://www.stsci.edu/hst/wfpc2/analysis/lrf\\_calibration.html](http://www.stsci.edu/hst/wfpc2/analysis/lrf_calibration.html)

with the correct drizzling pattern would allow one to create images with a pixel scale of approximately  $0.^{\prime\prime}02$  per pixel.

Our WFPC2 data include images taken with the PC detector as well as all three of the WF detectors ( $0.^{\prime\prime}0995$  per pixel); our NICMOS data were taken with NICMOS2 ( $0.^{\prime\prime}0756$  per pixel) and NICMOS3 ( $0.^{\prime\prime}202845$  per pixel). Each set of subexposures was drizzled more than once at different sampling rates (i.e. pixel scales) to produce different drizzle products that I use at different stages of the analysis. Experimentation with PSF subtraction (see Section 2.4) suggested that the most accurate PSF estimation was achieved with each image drizzled to its intrinsic resolution. For instance, NICMOS images drizzled to the resolution of the PC detector are oversampled by a factor of 2-4, yielding spurious brightness gradients and miscalculated PSF scale factors. With the PSF scale factors calculated using images drizzled to their native resolutions, each image was then redrizzled to the resolution of the PC detector for systematic comparison (see Section 2.6).

With the multidrizzling complete, my image processing steps were concluded, allowing the subtraction of the PSF of the quasars from the combined images.

## 2.4 PSF Subtraction

One of the most crucial parts of this work was the PSF scale factor determination. Because the light profile of a typical galaxy at  $z \approx 0.15$  is only slightly broader than the HST PSF, it is essential that the subexposures be aligned with extreme precision. Any misalignment will result in artificial broadening of the quasar PSF. To achieve this end, I ran MultiDrizzle iteratively every time I produced a drizzle product. In each iteration the subexposures were drizzled, the centroids of the quasars in the separately drizzled images were checked, corrections were made to the astrometry, and the images were drizzled again. This cycle was repeated until all the centroids fell within  $10^{-3}$  pixels of their target coordinates. Experimentation showed that the PSF subtraction was far more effective using these drizzle products than using products drizzled only once. Below I describe in detail the procedures I devised to determine the PSF scale factor and remove the unresolved quasar image from the image of the host galaxy.

Historically, different methods have been used to correctly map the normalized HST PSF. ? and ? observed a field star and used that as a PSF template. ? did the same, but also used continuum images of the quasars themselves as the PSF template in some cases. This approach was motivated by the realization that the quasar-to-galaxy contrast is so high in the continuum that rescaling the ? continuum images to the shorter exposure times and the narrow-band filters used in ? left essentially quasar-PSF-only images with very little light from the host galaxy. Both of these methods have the significant advantage that they exactly map the HST PSF at the same epoch and detector position of the quasar observations, rather than relying on theoretical PSF models. For this reason, my team also observed a PSF star in many of the ramp and narrow-band filters in which we made quasar observations, and we observed each quasar in a continuum filter in the optical and near-infrared.

Earlier works (e.g. ?) iteratively align and scale the PSF images in a three parameter fit: an x-axis alignment, a y-axis alignment, and a PSF intensity scale factor. As

described above, my iterative drizzling ensures that the PSF image as well as the quasar images are aligned with the image centers. This leaves the PSF scale factor as the only undetermined parameter.

The decomposition of the observed light profile is represented in the upper half of Figure 2.1 with a diagrammatic quasar PSF, host galaxy, and combined (observed) light profile. The goal of this processing step is to find a scale factor value that rescales the model (star) PSF to match the height of the quasar PSF component of the observed quasar image. The primary challenges are that the relative contributions of the quasar PSF and the galaxy light profile are not known *a priori*, and that the width of the WFPC2 PSF is only slightly sharper than the expected typical galaxy profile at  $z \approx 0.15$ .

Determining the scale factor with absolute certainty without prior knowledge of the galaxy light profile is impossible. Instead, the best solution is to make as few assumptions about the galaxy light profile as possible, and use those assumptions to place a lower limit on the galaxy luminosity. Utilizing the fact that the central black holes that power quasars are found in the nuclei of galaxies, ? assume that the galaxy light profile must decrease monotonically in the central few pixels around the quasar PSF; their residual light profiles may not have a central inflection.

The limiting case imposed by this assumption is a flat-topped profile. To achieve this limiting case, ? adopt a scale factor which makes the central pixel in the residual image have the same value as the average of the surrounding pixels. ? make the same basic assumption, that the galaxy's light profile must decrease monotonically, and they construct a model of a PSF plus host galaxy, which they fit to the data. In these cases the residual (galaxy) image after PSF removal is a lower limit on the galaxy flux; if the PSF scale factor were increased, it would violate the monotonicity condition.

In this work I present a PSF subtraction method which is also a lower limit on the galaxy flux, but which comes closer to the true galaxy light profile than the methods present in ? and ?. I assume that the galaxy light profile is cuspy; that is, as one moves away from the center of the light profile the post-subtraction residual descends no more rapidly than it did in more central pixels. The PSF scale factor is used for each of the quasar images is the value which just guarantees that this constraint of cuspyness is enforced. This method is graphically represented in the lower half of Figure 2.1, which shows the observed and galaxy-only light profiles seen in the top half of Figure 2.1, along with residual light profiles estimated using this method and the method presented in ?. Note that these diagrams are visual aids only; for actually light profiles, see Figure 2.2.

Mathematically, this amounts to a positive second radial derivative of the surface brightness with a negative radial first derivative. Because computing derivatives from discretely sampled data is numerically unstable, I avoided relying heavily on a small number of pixels by considering multiple radial directions from the center of the image and computing a scale factor for each direction. Then, I characterize this population of potential scale factors with a median and a standard deviation around the median. I adopt the median minus the standard deviation as my chosen scale factor; this choice is justified in that this type of scale factor represents a hard lower limit on the flux of the galaxy, so the lowest reasonable scale factor is the one most likely to be accurate. I then adopt the standard deviation around the median as the uncertainty in the scale factor.

This is graphically demonstrated in Figure 2.2, a gallery of azimuthally averaged light

profiles of observed quasars prior to PSF subtraction, their corresponding PSF stars, and the residual light profiles. The light profiles of the quasars before PSF subtraction are only slightly broader than the profiles of the PSF stars. The key element of our technique is visible in lack of inflection points in the residual light profiles; that is, they do not flatten near the center.

Of course, star-forming clumps, spiral arms, or any other lumpiness in the light profile would cause a galaxy to violate this condition. For this reason I only demand that this condition be satisfied in the central few pixels.

Having observed both PSF stars and continuum quasar images, I experimented with both types of PSF templates. My experiments showed that the PSF star images consistently produced superior results. In particular, while the subtracted images produced with these two different templates were qualitatively similar, the use of the quasar continuum image as a PSF template is more prone to obvious over subtractions, which were clearly discernible by large areas of negative pixels. Negative pixel values are the first and most readily visible diagnostic of a failed PSF subtraction as they are completely non-physical. With this simple test, I easily determined that using stars as PSF templates is a superior technique. This result is not surprising given that I am able to detect the host galaxies in the continuum images (see Section 2.9 and Tables 2.3 and 2.4 for details of the detections), indicating that the continuum-image light profiles are broader than, and thus poor analogs for, quasar PSFs themselves.

PSF-subtracted images of each of my quasar host galaxies in each of the filters used are shown in Figure 2.3.

## 2.5 Artificial Galaxy Simulations

As seen in Figure 2.3, the PSF subtraction technique described above produces visually plausible residual galaxy images. Nevertheless, visual inspection is, by itself, an insufficient diagnostic. Because the quasar is so much brighter than the galaxy (???), especially in the central pixels of the optical images, there is typically a wide range of PSF scale values that produce visually and physically plausible residuals. An additional test is needed to confirm that this method, while theoretically sound, works in practice. Indeed, the numerical and methodological uncertainties in any PSF subtraction technique warrant rigorous diagnostics.

To this end, I repeated the PSF subtraction procedure with 1000 simulated galaxies in each of the continuum filters, and then verified my technique by recovering their original profiles. In each simulation I constructed an image with a quasar component and a galaxy component, varying the quasar and galaxy brightness and galaxy morphology over the range of physically plausible values to ensure that my technique is general enough.

The primary component of my simulated data is the light profiles of the quasars themselves. For this I used an image of the PSF star in the WFPC2 and NICMOS filters rescaled to the appropriate magnitude. The magnitude was chosen randomly from the range of actual magnitudes of my quasars in Johnson filters similar to the filters used for my continuum observations. My quasars range from magnitude 14.5 to 16.5 in the B filter, so I adopted that as the range for my simulated quasars in the F467M filter.

Similarly, my quasars range from magnitude 14 to 15.5 in the K filter, so I adopted that range for my simulated quasars in the F237M and F222M filters.

I used the IRAF task “mkobjects” to generate artificial galaxy light profiles. The “mkobjects” task allows the user to vary the functional form of the light profile, as well as a range of light profile parameters, such as scale radius, ellipticity, and position angle, and overall brightness. To ensure that this technique is effective for all reasonable galaxy profiles, I varied the profile parameter values over ranges large enough to encompass all likely possibilities.

For this work I created galaxies with both exponential disk and De Vaucouleurs profiles superimposed on each other to simulate the bulges and the disks of host galaxies. I varied the intensities of the bulge and disk components, ranging from bulge-only galaxies (ellipticals, the most likely quasar host morphology) to bulge-disk galaxies.

I varied the scale radius for the bulge of each galaxy over the range that is physically plausible. For my most distant quasar, PG 1307+085, 7 pixels on the PC detector is 0.9 kpc; for my nearest quasar, PG 1244+026, 250 pixels on the PC detector is 10.3 kpc. Therefore, I chose 7 to 250 pixels as the range for the scale radii of the bulges of my simulated galaxies. The disk component was assigned a scale radius randomly in the range from one half to twice the scale radius of the bulge. The axis ratio of the bulge was chosen randomly between 0.6 and 1, and for the disk between 0.3 and 1. The position angle of the bulge and the disk were chosen randomly but were always equal (i.e., they were always aligned).

While there are many sources of noise in astronomical images, my analysis presented in Section 2.7 indicates that the dominant source of noise in my data is photon/counting noise rather than sky or read noise. To emulate this, “mkobjects” employs a stochastic algorithm which ensures that the images are not just perfectly smooth light profiles. Additionally, I seeded the random number generator with the machine system time, ensuring the uniqueness of the noise of each simulated object.

The bulge magnitude of each simulated galaxy was set based on its simulated quasar’s magnitude. To relate the quasar magnitude to the bulge magnitude I invoke several established relationships. First, I assume that the central black holes are accreting at the Eddington Limit, the theoretical maximum physical accretion rate of a black hole found by balancing the outward radiation pressure to the inward gravitational pressure. Actual central black hole accretion rates span a wide range, but, as the theoretical upper limit on accretion, the Eddington Limit represents a worst-case-scenario for the PSF subtraction because it results in the lowest galaxy-to-quasar contrast. By verifying the PSF subtraction method in the worst-case-scenario, I prove its applicability to the real quasars presented in this work. Next, I connect the black hole mass to spheroid magnitude using known central black hole mass to host spheroid magnitude relations (?) and the “standard” quasar S.E.D. (?). Then, a random number from -1 to 1, based on the rms scatter in the ? relationship, was added to the bulge magnitude to simulate actual scatter in the relation between quasar magnitude and bulge magnitude. Finally, the disk magnitude was set to be the bulge magnitude plus a random number from -1 to 1. Thus, my simulated galaxies range from bulge-dominated to disk-dominated systems, in keeping with the observed properties of quasar host galaxies (??).

To verify my results, I then repeated the PSF subtraction procedure, described above

in Section 2.4, on my simulated galaxies. In this analysis the quantity of merit is the ratio of the PSF scale factor, computed using the method in Section 2.4, to the true scale factor, seeded into the simulated image. In Figure 2.4 I plot histograms of this ratio for the three continuum filters used (F467M, F222M, and F237M). These histograms peak strongly around a value of unity, indicating that in most of the 1000 simulations this procedure comes very close to recovering the true PSF scale factors.

More importantly, the histograms in Figure 2.4 are asymmetric in that, to the extent that the scale factor is miscalculated, it is far more likely to be slightly over estimated than underestimated. As discussed in Section 2.4, an overestimated scale factor results in an unrealistically faint residual (galaxy) image, while an underestimated scale factor results in an unrealistically bright residual (galaxy) image. Because my simulations report only small occurrences of scale factor underestimation, the galaxy detections reported in this work are confident. Specifically, when I take the median value of the underestimated scale factors for the simulated F222M, F237M, and F467M images I get 0.99, 0.99, and 0.98, respectively. These values represent the confidence in the simulated quasar host galaxy detections. When I take the median value of the overestimated scale factors for the simulated F222M, F237M, and F467M images I get 1.006, 1.03, and 1.1, respectively. These values represent the photometric uncertainties in the simulated quasar host galaxies. I stress here that these are worst-case-scenario estimates for the uncertainties, as I have assumed Eddington Limit accretion rates and continuum galaxy-to-quasar contrast ratios, which are lower than the emission line contrast ratios in ? and ?. Given that, the PSF subtraction uncertainty for each real image presented here is computed based on image statistics, described in Section 2.4.

## 2.6 Analysis of Host Galaxies After PSF Subtraction

### 2.6.1 Continuum Subtraction

The analysis in the following sections utilizes emission line strengths and line-ratios. For these reasons, it is necessary to remove any stellar continuum contribution in my galaxy-only images. The medium-band NICMOS filters used to make the near-infrared continuum observations were chosen to be adjacent to the Pa $\alpha$  emission line. Because the calibrated Pa $\alpha$  images are in units of flux ( $\text{erg s}^{-1} \text{cm}^{-2}$ ) and the near-infrared continuum images are in units of flux density ( $\text{erg s}^{-1} \text{cm}^{-2} \text{\AA}^{-1}$ ), to remove the continuum contribution to the Pa $\alpha$  images I simply subtracted the continuum images multiplied by the Pa $\alpha$  filter width. Because this method relies straightforwardly on the well measured properties of the NICMOS filters, the uncertainties in the continuum-subtracted Pa $\alpha$  images rely only on the uncertainties in the Pa $\alpha$  images and the near-infrared continuum images.

For the optical emission line images, the optical continuum images only provide an intensity map for the optical continuum at the wavelength of the emission line, so the continuum scale factor could not be determined a priori. Instead, I derived the continuum scale factors by imposing the constraint that there be no negative residuals after continuum subtraction. Specifically, my algorithm considered parts of the galaxies that were above the noise (as determined by the standard deviation of the background)

in both the emission line and continuum images, and computed a scale factor such that the faintest parts of the emission line image would be exactly zero after continuum subtraction. This simple yet robust condition proved to be enough to tightly constrain the continuum subtraction scale factor since, in most cases, the removal of the quasar PSF left relatively little flux in at least some areas of each of the host galaxies. In practice, the continuum contribution was very small in the emission line optical images, less than 0.1% on average.

As with the subtraction of the quasar PSF (see discussion in Section 2.4), the optical emission line only images represent lower limits. I estimate the uncertainty in this continuum-subtraction scale factor from the background noise in the images, since the noise represents the limit to which I can demand non-negative pixel values.

In this manner I constructed galaxy-only, emission line only images, and all references to host galaxy images hereafter refer to these continuum subtracted images.

### 2.6.2 Extinction Correction

As discussed in Sections 2.1 and 2.2, I determine in Section 2.8.1 the nature of emission line regions in the quasar host galaxies using emission line ratio diagnostics. Extinction due to interstellar dust poses a significant difficulty in the line-ratio diagnostic analysis because it affects bluer wavelengths of light more severely than red wavelengths (?). Without proper extinction correction, the emission line ratios used in this analysis would take on non-physical or, worse, physical but misleading values.

To correct for dust extinction, I employed maps of the ratio of H $\beta$  to Pa $\alpha$  in my galaxy-only images. For each pixel that was above the background noise in both the H $\beta$  and Pa $\alpha$  images I computed the H $\beta$  to Pa $\alpha$  ratio. The background noise was computed as the standard deviation of the background of the image. Background statistics were computed using parts of the image more than 50 pixels from the center (beyond even the most extended of the targets) and not occupied by known image defects (such as the NICMOS chip boundary).

The values were then binned and averaged, rejecting pixels where either H $\beta$  or Pa $\alpha$  were below the noise in their corresponding images, or where the measured line ratio exceeded the intrinsic T=10,000 K line ratio of  $I_0(\text{H}\beta)/I_0(\text{Pa}\alpha) = 2.146$  (?). The bins were sized on a case-by-case basis to be just large enough to include at least one legal pixel value; they were set to  $1 \times 1$  initially, and then expanded iteratively as square top-hats until at last one usable pixel fell within the bin. Although this strategy degrades the angular resolution of the H $\beta$  / Pa $\alpha$  map, it is absolutely necessary because the emission line images, and thereby every measured quantity in the sections that follow, depend heavily on the extinction correction, especially near the severely extinguished galactic centers.

I used the line ratio maps in tandem with the average extinction law that ? derive in terms of  $A_\lambda/A_V$ . Taking the  $A_\lambda/A_V$  values they tabulate for the case of  $R_V = A_V/\text{E(B-V)} = 3.1$ , I compare my H $\beta$  to Pa $\alpha$  values to the intrinsic value  $I_0(\text{H}\beta)/I_0(\text{Pa}\alpha) = 2.146$  to find  $A_V$  for each pixel as follows:

$$A_{H\beta} = A_V \left[ \frac{A_{H\beta}}{A_V} \right] = -2.5 \log \left( \frac{I(H\beta)}{I_0(H\beta)} \right) \quad (2.1)$$

$$A_{Pa\alpha} = A_V \left[ \frac{A_{Pa\alpha}}{A_V} \right] = -2.5 \log \left( \frac{I(Pa\alpha)}{I_0(Pa\alpha)} \right) \quad (2.2)$$

$$A_V = \frac{-2.5 \log \left( \frac{I(Pa\alpha)}{I(H\beta)} \frac{I_0(H\beta)}{I_0(Pa\alpha)} \right)}{\left[ \frac{A_{Pa\alpha}}{A_V} \right] - \left[ \frac{A_{H\beta}}{A_V} \right]} \quad (2.3)$$

where  $I(\lambda)$  is the observed flux at a chosen wavelength and  $I_0(\lambda)$  is the intrinsic (unextinguished) flux. With these  $A_V$  values, I created maps of  $A_V$  for each of my quasar host galaxies, shown in Figure 2.5. Using these maps, I corrected each image of each quasar for extinction:

$$\log I_0(\lambda) = \log I(\lambda) + \frac{A_V}{2.5} \left[ \frac{A_\lambda}{A_V} \right] \quad (2.4)$$

where  $A_\lambda/A_V$  was obtained from the ? extinction law.

In this way an extinction corrected version of each image was created for all the PSF-subtracted, galaxy-only, emission line images, which are hereafter referred to as extinction-corrected images.

## 2.7 Analysis of Uncertainties

Understanding uncertainties is important in any observation, but particularly important in observations such as this where the target's signal is overwhelmed by a much stronger signal; in this case, the signal of a quasar. This situation is complicated by the large number of steps and large number of images, described in Section 2.6, used to produce an emission line image of a quasar host galaxy. The uncertainty map in each final science image depends on the uncertainty maps of as many as ten drizzled images, each propagated through all the processing steps needed to produce the final science images, namely quasar PSF subtraction, continuum subtraction, and reddening correction. For example, the uncertainty map for a final  $[O\text{ II}]\lambda 3727$  science image utilizes the uncertainty map of the drizzled  $[O\text{ II}]\lambda 3727$  image, the optical continuum image for continuum subtraction, the  $H\beta$  and  $Pa\alpha$  image for reddening correction, the infrared continuum image for continuum subtraction of the  $Pa\alpha$  image, and the corresponding PSF star image for each of the quasar images.

Prior to any of these processing steps, the typical photometric uncertainties associated with counting statistics are the primary source of uncertainty in the raw images. My narrow-band space-based observations are relatively background free, making background noise and uncertainties from background subtraction a small component of my net uncertainties. Unfortunately, the process of drizzling the raw images creates correlated noise, making simple Poissonian estimators of uncertainties inapplicable. Because the effective exposure time of a pixel in a drizzled image depends on the relative align-

ments of the undrizzled images, the change in plate scale from before and after drizzling, and the choice of drizzle kernel used, MultiDrizzle produces a weight map image which is essentially an exposure time map of the drizzled image (??). Formally, the uncertainty for an image that is in units of counts is the square root of each pixel value; since this project's images are in counts-per-second, I assign to each pixel in the uncertainty map the square root of the ratio of that pixel in counts-per-second to the value of the corresponding pixel in the exposure time map as the value in an uncertainty map image. For quasar-image pixels which are negative due to noise or bias subtraction, I take the absolute value.

The first step, the removal of the quasar PSF to produce galaxy-only images, draws its uncertainties from three sources: the uncertainty map for the drizzled quasar+galaxy image, the uncertainty map for the corresponding PSF star image, and the uncertainty in the scale factor used to rescale the PSF star image to match the PSF of the quasar (see Section 2.4 for a complete discussion of the meaning and calculation of this scale factor). For each pixel in the galaxy-only image I write the equation:

$$I(\text{galaxy}) = I(\text{drizzled}) - S_{PSF} I(\text{PSF}) \quad (2.5)$$

where  $I(\text{galaxy})$  is the intensity of the galaxy at the pixel,  $S_{PSF}$  is the PSF subtraction scale factor, and  $I(\text{PSF})$  is the intensity of the PSF image at the same pixel location.

Propagating these three uncertainties through, I arrive at the equation used to generate the uncertainty maps for the galaxy-only images:

$$[\delta I(\text{galaxy})]^2 = [\delta I(\text{drizzled})]^2 + (\delta S_{PSF})^2 [I(\text{PSF})]^2 + S_{PSF}^2 [\delta I(\text{PSF})]^2 \quad (2.6)$$

where  $\delta S_{PSF}$  is the uncertainty in the PSF scale factor and  $\delta I(\text{galaxy})$ ,  $\delta I(\text{drizzled})$ , and  $\delta I(\text{PSF})$  are the uncertainties in the galaxy-only images, the drizzled quasar+galaxy images, and the PSF star images, respectively.

The second step, the removal of the continuum contribution to each galaxy-only image, is discussed in detail in Section 2.6.1. Because the continuum subtraction of the Pa $\alpha$  images relies only on the ratio of the filter widths of the NICMOS filters used for the Pa $\alpha$  and infrared continuum observations, the emission line only Pa $\alpha$  uncertainty maps rely solely on the galaxy-only Pa $\alpha$  and infrared continuum uncertainty maps. The optical emission line images have the additional uncertainty from the computation of the continuum-subtraction scale factor, discussed in Section 2.6.1. As with the quasar PSF subtraction, I propagate the uncertainties in this process through:

$$I(\text{line}) = I(\text{galaxy}) - S_{cont} I(\text{continuum}) \quad (2.7)$$

$$[\delta I(\text{line})]^2 = [\delta I(\text{galaxy})]^2 + (\delta S_{cont})^2 [I(\text{continuum})]^2 + S_{cont}^2 [\delta I(\text{PSF})]^2 \quad (2.8)$$

where  $I(\text{line})$  is the intensity of the emission line only image,  $I(\text{cont})$  is the intensity of the continuum only image, and  $S_{cont}$  is the continuum scale factor (determined using the method described in Section 2.6.1). As before,  $\delta I$  and  $\delta S$  represent uncertainties. The final processing step, extinction correction, is discussed thoroughly in Section 2.6.2. In addition to the uncertainty maps for the emission line only images, the uncertainties in the H $\beta$  to Pa $\alpha$  line ratio maps also contribute to the uncertainty maps for the extinction-

corrected images. The uncertainty in each bin in the H $\beta$  to Pa $\alpha$  line ratio maps is the uncertainty in the average of all the pixels contributing to that bin. This uncertainty, propagated through Equation 2.1, determines the uncertainty in the extinction:

$$\delta A_V = \frac{2.5}{\left[ \left[ \frac{A_{\text{Pa}\alpha}}{A_V} \right] - \left[ \frac{A_{\text{H}\beta}}{A_V} \right] \right] \log_e 10} \sqrt{\left( \frac{\delta I(\text{H}\beta)}{I(\text{H}\beta)} \right)^2 + \left( \frac{\delta I(\text{Pa}\alpha)}{I(\text{Pa}\alpha)} \right)^2} \quad (2.9)$$

I then combine this uncertainty with the uncertainty computed in the uncertainty map of the emission line only image, propagating the uncertainties through Equation 2.4 to create an uncertainty map of the extinction-corrected image:

$$\left( \frac{\delta I_0(\text{line})}{I_0(\text{line})} \right)^2 = \left( \frac{\delta I(\text{line})}{I(\text{line})} \right)^2 + (\delta A_V)^2 \left[ \frac{\log_{10} \left[ \frac{A_\lambda}{A_V} \right]}{2.5} \right]^2 \quad (2.10)$$

where  $\delta I_0(\text{line})$  denotes the uncertainty for each pixel in the extinction-corrected emission line only host galaxy images. With the extinction correction complete, the original photometric errors are thus propagated through to uncertainty maps of the final science images; all emission line luminosities and emission line luminosity dependent quantities quoted hereafter, such as the line ratios described in Section 2.8.1, draw their uncertainties from the uncertainty maps of the science images.

Typical uncertainty maps are shown in Figure 2.6. In each case the object is visible because the higher count rate results in greater absolute uncertainty, albeit with a higher signal-to-noise ratio (S/N). In all cases, the two main contributions to the uncertainty are the removal of the quasar PSF, which primarily affects pixels near the center of the image, and the extinction correction, whose uncertainty is greatest near the edge of the object where the H $\beta$  S/N ratio drops off. Typically, the removal of the quasar PSF causes the net S/N to fall by a factor of two, usually ending up in the low tens, while the correction for extinction decreases the signal-to-noise by anywhere from ten percent to factors of a few, typically giving a final S/N of a few.

## 2.8 Results

### 2.8.1 Line Ratios

Using the images of the quasar hosts after continuum subtraction and extinction correction, I characterize the power source of line emission in the host galaxies on a region-by-region basis through the use of emission line ratio diagnostics. Specifically, I determine whether the line emission in a region is powered by the hard ultraviolet and X-ray flux from the central quasar or the softer ultraviolet flux from young stellar populations (???) by placing emission from that region in a [O III] to H $\beta$  versus [O II] to [O III] plot in Figure 2.7, a variant of the diagnostic line-ratio diagram in ?. Because the relative strengths of the emission lines reflect the ionization states of the species involved, line-ratio diagrams distinguish between hard and soft ionizing power sources (??). The particular diagram that I use is taken from Figure 1 of ?, where the authors observe that star-forming complexes fall near the curved track seen in Figure 2.7, while AGN narrow-line regions,

favoring [O III] with their harder ionizing flux, fall above the track, and shocks fall to the side of the track near  $[\text{O III}]/[\text{O II}] \approx -1$ .

By comparing the location of the line emission in my diagnostic diagrams to line-ratio delineation curves, I identify the power source of the line emission; specifically, a region with elevated  $[\text{O II}]/[\text{O III}]$  or depressed  $[\text{O III}]/\text{H}\beta$  is characteristic of gas irradiated by hot stars, while a region with high  $[\text{O III}]/\text{H}\beta$  is more characteristic of an AGN narrow-line region. These line-ratio diagrams are shown in Figure 2.7.

The background of each line-ratio diagram is shaded with a color corresponding to the different sources of line emission; red for AGN narrow-line regions, blue for star forming regions, and green for shocks. To identify intermediate or ambiguous cases, the colors fade smoothly from one to another. Shown along side the line-ratio diagrams in Figure 2.7 is a line-ratio map of the host galaxy. These maps were created by multiplying a greyscale  $\text{H}\beta$  image of the host galaxy by the color vector from each pixel's location in the diagnostic diagram. In this manner, I map out the emission line morphology of each host galaxy.

I plot, in the upper left corner of each diagnostic diagram, average error bars for all the pixels included on the plot. While the uncertainty on each pixel is significant, typically around a few tenths in log-log space, the physical significance of pixels with similar line ratios that are adjacent in the host galaxy is much greater. For example, in every diagnostic diagram presented there is a cloud of pixels around the star-formation track. The thickness of the cloud is dominated by measurement error, but, as it is highly unlikely that random chance would conspire to move all the pixels in a particular direction, the centering of the cloud on the star-formation track is highly indicative. Considering statistical significance in this fashion is effectively the same as binning the pixels, except that every pixel in the images can be easily identified in the diagnostic diagrams.

In Section 2.7, I noted that the extinction correction adds significantly to the uncertainty of each emission line image. In the line-ratio diagnostic diagrams, this contribution is not as severe as both quantities in each ratio are affected, albeit not equally. The y-axis,  $[\text{O III}]/\text{H}\beta$ , is particularly robust against errors from extinction-correction because the wavelengths of the [O III] and  $\text{H}\beta$  lines are fairly close. The x-axis,  $[\text{O III}]/[\text{O II}]$ , is more vulnerable. In each diagram in Figure 2.7 I have plotted an extinction track of two magnitudes in  $\text{A}_V$ , pointing to the lower left. Fortunately, this track is nearly parallel to the lower left portion of the star-formation track, making the results of PG 1626+554, the object for which I do not have extinction values, robust.

As noted above, there is a cloud of pixels around the star-formation track (blue) in each of the diagnostic diagrams. For several objects, PG 0026+129, PG 1244+026, PG 1448+273, and PG 2214+139, there is a tail of pixels in the shock region of the diagram (green) which are also adjacent and near the object center in the shaded galaxy image. For one object, PG 0026+129, there are a number of pixels in the AGN region (red) which are also adjacent and near the object center in the shaded galaxy image. These and other findings will be discussed in greater depth in Section 2.9.

Additionally, I also plot azimuthally averaged (averaged within concentric annuli) line-ratios as a function of radius from the galactic center for each of my objects in Figure 2.8. The azimuthal average has the merit of greater signal-to-noise than a direct

line-ratio map as in Figure 2.7, yet still bears out any trend in harder ionizing radiation toward the nucleus, as one might expect if a narrow-line region is present in the middle of a star-forming galaxy.

### 2.8.2 Emission Line Region Sizes

Spatially resolved host galaxy images enable this study to address narrow-line region size vs. luminosity issues from earlier works. By comparing the sizes of their quasar host galaxies to each other and to the sizes of narrow-line regions in Seyfert Galaxies, ? find a narrow-line region size vs. luminosity relationship that spans almost three orders of magnitude in luminosity. Meanwhile, ? argue that the emission line luminosity is most likely powered by star formation at large distances from the quasar on the grounds that extrapolating this relationship to large quasar luminosities yields narrow-line regions larger than many galaxies. In Section 2.9, I use the line-ratio diagnostics from Section 2.8.1 to address the power source of line emission; here I describe the procedure used to determine galaxy sizes.

I report the 90% and 95% light radii in Tables 2.3 and 2.4, respectively. The values were determined by taking successively larger apertures around the quasar host galaxies and finding the asymptotic flux rate, and then repeating that procedure to find a fraction of that flux (in this case 90% and 95%).

The sizes quoted range from several tenths to several kpc, and are generally very similar for 90% and 95% light radii, indicating that these estimates of size are convergent and represent reasonable metrics for the sizes of the emission line regions. In each of the emission line images I see the object centered on the location of the quasar; with the exception of small features, there are no displaced concentrations of star formation.

## 2.9 Discussion

I report at least some galaxy light in each filter for each quasar. The host galaxies are, typically, bright and easily seen in the infrared images, and faintest in the optical continuum images. With a few exceptions, I see little evidence of structure other than smooth, azimuthally symmetric light profiles. The charge transfer inefficiency streak is visible in many of the WFPC2 images, even after removal of the quasar PSF, especially in cases where the telescope roll angle was not the same for the PSF and quasar images. Near the center of the majority of the images there is noise from the PSF subtraction, visible as mottled dark and light pixels. Even with a correctly aligned PSF (described in Section 2.3) and a correctly computed PSF scale factor (described in Section 2.4, verified in Section 2.5), counting noise in the PSF image as well as minute variations in the telescope optics (?) still unavoidably cause some differences between the quasar and model PSF, resulting in imperfectly subtracted pixels.

I find that the continuum does not significantly contribute to the optical narrow-band images. I expected relative faintness of the galaxies in the optical continuum because the galaxy flux density is much higher in the emission lines. The flux density of the infrared continuum is much higher compared to the Pa $\alpha$  emission line than the optical

continuum is compared to the optical emission lines, making it a larger contamination, though still small contribution to the Pa $\alpha$  emission line flux.

The morphological character of the galaxies (best seen in the infrared continuum images) is typically unaffected by extinction correction. Even though the computed luminosities are larger after extinction correction, the signal-to-noise is lower due to the large uncertainty in the extinction correction (as described in Section 2.7). The background noise in the images takes on a cobbled appearance, partly due to the larger NICMOS pixels in the Pa $\alpha$  images, and partly due to the need to bin the line-ratio maps (as described in Section 2.6.2).

Morphologically, these objects are nearly featureless, consistent with the expectation (??) and the observation (?) that the majority of quasars are hosted either in ellipticals or in galaxies which are evolving toward ellipticals. I detect one edge-on spiral, PG 0838+770; this dramatic example of late-type galaxy morphology was not specifically known until these observations, although ? find two spirals in their sample of quasar host galaxies. It also consistent with ?, who find roughly one third of their 32 quasar hosts galaxies to be late-type. The disk structure of PG 0838+770 is clearly visible in the Pa $\alpha$  and the infrared continuum image, and the Pa $\alpha$  brightness indicates star-forming activity along the disk as well as in the nucleus.

Additionally, a galaxy near PG 1613+658 reported by ? is easily visible in the Pa $\alpha$  and infrared continuum images. Without redshift information neither I nor ? can confirm an association between these objects. However, a number of indirect indicators suggest that the two galaxies are related: The separation is quite close (1 arcsecond), the angular size is comparable (0.5 vs. 0.8 arcseconds), and the companion is also Pa $\alpha$  bright (suggesting rapid star formation), implying that these objects have suffered a recent interaction. This is in line with theoretical works (e.g. ???), which indicate that quasar and star-formation activity can be triggered by interactions. Additionally, ? report that PG 1613+658 is coincident with a poor cluster of galaxies at the same redshift, providing a pool of potential interaction partners, and that there is a tidal tail to the East of PG 1613+658, suggesting recent interaction.

As described in Section 2.8.1, I use emission line diagnostics, shown in Figure 2.7, to determine at each point in the host galaxy the power source of the line emission. As a caveat, the images in Figure 2.7 have noise from each of the images used to create them; any individual pixel is not significant on its own, but contiguous regions of similar pixels are. I find that the majority of the line emission from my quasar host galaxies has a line-ratio signature consistent with star formation. Moreover, only a few small sections near the nuclei of several of the objects have [O III]/H $\beta$  ratios greater than 10, which is the only unambiguous signature of AGN narrow-line regions. In particular, I see high [O III] to H $\beta$  ratios near the nucleus of PG 0026+129, my most luminous quasar (see below for further discussion).

This result comes down decidedly in favor of the interpretation of quasar host galaxy line emission discussed in ?, and suggests that the narrow-line region size to luminosity relation put forth in ? does not extend into the high luminosity regime of quasars. I do see sizes and luminosities consistent with the relations reported in ?, plotted in Figure 2.9, but I conclude that only small portions of these emission line regions are quasar narrow-line regions. As a confirmation, the azimuthally averaged line ratios shown in Figure

2.8, which have a much higher signal-to-noise than the line-ratio diagnostic diagrams and maps in Figure 2.7, also indicate  $[\text{O III}]/\text{H}\beta$  ratios too low for narrow-line regions, except near the very centers of several objects, and have overall line-ratios more consistent with star-formation.

Taking the line emission as an indicator of star formation, I use the prescription in ? to compute star-formation rates. I list these, along with luminosities in each band, in Table 2.5. I find typical rates of a few  $M_\odot/\text{yr}$ , but ranging from less than one to over twenty  $M_\odot/\text{yr}$ , a result which is broadly consistent with theoretical works, such as ? and ?, which predict that rapid star formation coincides with quasar activity. These star-formation rates are on the low end, though, of those predicted by ? and ?, and are, oddly enough, in line with the observations of ?, who note that quasars often have relatively weak  $[\text{O II}]$  lines, and thus probably do not have enormously high star-formation rates. ? proceeds to conclude that quasar activity does not coincide with starburst activity; as discussed above, the line-ratios indicate that star formation is powering the line emission, albeit at a somewhat lower rate than expected for starburst galaxies. The one exception in this sample is PG 1626+554, which I measure to have a star-formation rate of around  $25 M_\odot/\text{yr}$ . This is particularly true when I plot star-formation rates against quasar luminosities in Figure 2.10(a); I see that the least luminous quasar, PG 1244+026, also has the lowest star-formation rate.

The picture that is painted by my sample of eight quasar host galaxies appears intermediate between the paradigm of quasar hosts as starburst galaxies and the post-starburst E+A host galaxies described in ?. It is possible that the majority of my objects are simply passed their peak star-formation rates. Supporting this hypothesis, the brightest quasar, PG 0026+129, does not have a particularly high star-formation rate for this data set, suggesting that it may have passed its peak of star formation.

In Figure 2.10(b) I plot star-formation rate against host galaxy stellar mass, determined from the infrared continuum luminosities using established mass-to-light ratios (?). I find that, in addition to having the lowest star-formation rate, PG 1244+026 also has the lowest stellar mass, suggesting that it is a overall small object. Meanwhile, six of the host galaxies show a trend of increasing star-formation rate with increasing stellar mass, the exception being PG 0026+129, whose star-formation rate is similar to the next most massive galaxy, PG 1448+273, even though it is over thirty times as massive.

To quantify this trend, I performed a Spearson Rank-Order correlation test (?) on the SFR vs. galaxy mass data; the rank-order coefficient is 0.54 with confidence is 0.78, indicating that the two parameters are highly likely to be correlated for these seven objects. This is consistent with the models presented in ? and ?, which indicate that accretion rate and star-formation rate evolve with time and, in the cases of mergers, depend on the collision geometry.

The potential significance of these considerations becomes even more apparent in Figure 2.11, where I plot star-formation rate per galaxy stellar mass vs. the Eddington Ratio for the central black holes. Here, the Eddington Ratios are derived from the quasar optical continuum luminosities computed during PSF removal and the central black hole masses listed in Table 2.1. This plot essentially compares how fast each galaxy is growing, for its size, versus how fast its respective black hole is growing, for its size. The trend is less strong but still present, with a Spearson-Rank Order confidence of -0.43 with a

confidence of 0.66. While I cannot draw more precise conclusions from such a small sample, the different mass-specific star-formation rates indicate that these objects are not simply scaled versions of each other.

I see that the objects with the highest Eddington Ratios have the lowest mass-specific star-formation rates. It is possible that these particularly active quasars are more efficiently quenching the star formation within their host galaxies. Or, perhaps the trend in Figure 2.10(b) is driven by a lag between the peak of quasar activity and the peak of star formation, as suggested by ?. This hypothesis is supported by the fact that the quasars with the highest Eddington Ratios, PG 0026+129, PG 1244+026, and PG 1448+273, are also three of the four that are seen to harbor shocked gas in Figure 2.7. My observations here suggest a link between high black hole accretion rates, shocked gas, and diminished mass-specific star-formation rates.

## 2.10 Future Directions

The results of this study represent a first look at the inner mechanisms of quasar host galaxies, but they do not tell the complete story. For example, these results suggest that the peak of black hole accretion, as sampled by typical quasars, may not coincide with the peak for star formation. While I speculate here that typical quasars are passed the peak of star formation, only a complete chronology will fully resolve this issue by allowing a direction comparison with models. To this end, I suggest extending the line-ratio study presented here to analogous quasar host galaxies that are near the peak of star formation and prior to the peak of black hole accretion. Logical candidates would be quasar hosts which show clear signs that they are in the early stages of merging, such as those exhibiting tidal tails and double nuclei in ?. More ambitiously, many researchers are investigating signs of binary black holes in quasars. If such an object is ever confirmed, it would warrant a line-ratio study as well since it would represent an intermediate phase in the chronology where the galaxies have fully merged but the black holes have not.

While the space-based emission line study presented here has the advantages of the high angular-resolution and multi-wavelength coverage needed to make line-ratio diagnostics possible, it lacks the depth to return much morphology information about the galaxies detected. With the exception of the edge-on disk in PG 0838+770 and several knots in the [O III] images, the galaxies I detect are featureless and symmetric. Yet, as seen in Figure 2.10, their masses are consistent with the KISS galaxies. This study lacks the depth needed to detect the low surface-brightness extended portions of the galaxies, leaving ambiguous whether these are the cores of spiral galaxies, such as PG 0838+770, or the centers of nascent elliptical galaxies. While deeper HST imaging would certainly be ideal, expected developments in laser guide star adaptive optics at ground-based observatories, such as Gemini, may provide PSFs stable enough to permit detection of quasar host galaxies. Additionally, the contamination of the PSF is less severe near the edges of the galaxies where the deeper imaging is badly needed. Observations with eight-meter class telescopes and adaptive optics could quickly achieve the depth needed to detect low surface brightness features.

Even deep observations in the optical and near-infrared do not directly address heav-

ily obscured star formation. While the work presented here puts great emphasis on correctly accounting for dust extinction, complementary far-infrared observations address this issue directly by recapturing the ultraviolet energy lost to extinction. However, without line-ratio maps, such as those presented here, maps of far-infrared emission in quasar host galaxies remain ambiguous; the warm dust could be heated by the central AGN or by star-formation. I propose to make far-infrared observations of the quasar host galaxies studied here using instruments such as ALMA or Herschel and, using far-infrared luminosity images, map out heavily obscured star formation. Observations such as these will fill in the missing gaps in our understanding of the dynamics of active galaxies.

Finally, I intend to run my own line-ratio simulations with CLOUDY and expand upon the results presented here in a forthcoming paper. While the line-ratio diagnostic diagram I borrow from ? is sufficient to distinguish between regions whose line emission is powered by star formation, shocked gas, or AGN irradiation, I wish to explore the details further. For instance, it will be possible to remove in a precise way the AGN and shocked gas contribution to intermediate points. Also, a point's location on the star-formation track in the line-diagnostic diagram is driven by metallicity; with my own line-ratio diagram I can use the line-ratios to estimate the metallicities of regions within the quasar host galaxies, thereby constructing a metallicity map for the star-forming portions of these galaxies just as I constructed reddening maps. A modern, up-to-date line-ratio diagram will resolve the fine details in these issues and allow a complete analysis of these objects.

Ambitiously, if the signal-to-noise in the metallicity maps is high enough, I may be able to track metallicity gradients through the galaxies. Comparing the metallicity distribution with the locations of the shock features or the near-infrared morphology, possibly in deeper images, could give the community some idea of how metals are distributed through quasar host galaxies. This information could, in principle, be an asset to theorists modeling the evolution of these galaxies; in this way my observations could have a significant impact on our understanding of the evolution of quasar host galaxies.

## 2.11 Conclusions

The eight quasar host galaxies presented in this work have emission line ratios primarily consistent with star formation. Additionally, I see several objects, PG 0026+129, PG 1244+026, PG 1448+273, and PG 2214+139, which show line-ratios consistent with shocked gas, and one object, PG 0026+129, which shows evidence of a narrow-line region near its center. However, even in this case, the narrow-line region is less than a kpc in size, indicating that the size-luminosity relationship presented in ? breaks down at quasar-level luminosities.

I see star-formation rates of less than  $10 M_{\odot}/\text{yr}$  for all objects except PG 1626+554, whose star-formation rate is over  $25 M_{\odot}/\text{yr}$ . PG 1244+026 has the lowest star-formation rate,  $0.2 M_{\odot}/\text{yr}$ ; I believe that this is a very small galaxy, around  $10^{10} M_{\odot}$ . The remaining six quasar hosts are most likely passed their peak star-formation rates. If so, this fact will help constrain models of quasar+galaxy evolution as well as hydrodynamic models of AGN outflows. It could also guide early universe studies by putting observations of

high redshift quasars in context.

I also see evidence that these objects are heterogeneous in character and not simply scaled versions of each other. I find a trend that quasars with higher Eddington Ratios are more likely to have low mass-specific star-formation rates; the presence of shocked gas in extreme examples suggests that the central black holes are in the process of quenching star-forming activity.

In a forthcoming paper I intend to run our own line-ratio simulations with CLOUDY, and confirm these results with our line-diagnostic diagrams. I also wish to use far-infrared observations, potentially with ALMA, to explore obscured star formation in these objects.

Table 2.1. Target Quasars and Their Basic Properties

Quasar	$z$	$m_V$ (mag)	$M_V$ (mag)	$L_{\text{PAH} 7.7\mu\text{m}}^{\text{a}}$ (erg s $^{-1}$ )	$L_{[\text{Ne II}] 12.8\mu\text{m}}^{\text{a}}$ (erg s $^{-1}$ )	$L_{\text{FIR}}^{\text{b}}$ (erg s $^{-1}$ )	$M_{\text{BH}}$ (log $\frac{M}{M_\odot}$ )
PG 0026+129	0.1420	14.78	-24.18	$< 4.28 \times 10^{42}$	$1.13 \times 10^{41}$	$3.17 \times 10^{44}$	$7.4 \pm 0.07^{\text{c}}$
PG 0838+770	0.1310	15.70	-23.08	$4.38 \times 10^{42}$	$1.73 \times 10^{41}$	$5.73 \times 10^{44}$	$8.2 \pm 0.08^{\text{d}}$
PG 1244+026	0.0482	16.20	-20.37	$3.18 \times 10^{41}$	$4.97 \times 10^{40}$	$1.37 \times 10^{44}$	$6.5 \pm 0.08^{\text{d}}$
PG 1307+085	0.1550	15.32	-23.84	$< 1.28 \times 10^{42}$	$2.45 \times 10^{41}$	$9.72 \times 10^{44}$	$8.5 \pm 0.1^{\text{c}}$
PG 1448+273	0.0650	15.01	-22.22	$1.49 \times 10^{42}$	$4.86 \times 10^{40}$	$8.28 \times 10^{43}$	$7.0 \pm 0.08^{\text{d}}$
PG 1613+658	0.1290	15.49	-23.26	$1.56 \times 10^{43}$	$1.57 \times 10^{40}$	$2.15 \times 10^{45}$	$7.4 \pm 0.2^{\text{c}}$
PG 1626+554	0.1330	16.17	-22.64	$3.08 \times 10^{42}$	$3.00 \times 10^{40}$	$2.28 \times 10^{44}$	$8.5 \pm 0.08^{\text{d}}$
PG 2214+139	0.0658	14.66	-22.59	$1.21 \times 10^{42}$	$2.11 \times 10^{40}$	$2.32 \times 10^{44}$	$8.6 \pm 0.09^{\text{d}}$

<sup>a</sup>PAH and [Ne II] 12.8  $\mu\text{m}$  luminosities from the Spitzer spectra of ?.<sup>b</sup> 8-1000  $\mu\text{m}$  FIR luminosity based on ISO fluxes (from ?).<sup>c</sup> black hole masses from ?<sup>d</sup> black hole masses from ?

Table 2.2. Filters &amp; Exposure Times in Seconds

Object	WFPC2					NICMOS	
	Optical Cont.	H $\beta$	[OII]	[OIII]	[OIII] Cont.	Pa $\alpha$	Cont.
PG 0026+129	F467M 184	FR533N 3000	FR418N 4620	FR533N18 <sup>b</sup> 2400	F588N <sup>b</sup> 240	F215N 2112	F237M 144
PG 0838+770	F467M 80	FR533N18 800	FR418N 3400	FR533N18 800	...	F212N 2112	F237M 336
PG 1244+026	F467M 240	FR533N 920	FQUVN 2240	FR533N 1200	...	F196N 1984	F222M 288
PG 1307+085	F467M 400	FR533N18 820	FR418N 1840	FR533N33 <sup>b</sup> 1500	F588N <sup>b</sup> 240	F216N 2048	F237M 224
PG 1448+273	F467M 320	FR533P15 3600	FQUVN 3800	FR533P15 1760	...	F200N 2048	F222M 240
PG 1613+658	F467M 240	FR533N18 440	FR418P15 1380	FR533N18 440	...	F212N 2112	F237M 288
PG 1626+554	F467M 320	FR533N18 1660	FR418N 6100	FR533N33 1800	...	...	...
PG 2214+139	F467M 320	FR533P15 2840	FQUVN 1800	FR533P15 1300	...	F200N 1824	F222M 192

<sup>a</sup>The exposure time is given below each filter in seconds.<sup>b</sup>These data provided by ?.

Table 2.3. 90% Light Radii [kpc]

Object	Opt.	[O II]	H $\beta$	[O III]	Pa $\alpha$	IR
PG 0026+129	1.6 ± 0.1	4.4 ± 0.1	3.7 ± 0.2	4.7 ± 0.2	0.9 ± 0.2	4.3 ± 0.1
PG 0838+770	0.5 ± 0.1	4.6 ± 0.1	0.6 ± 0.1	3.2 ± 0.1	0.9 ± 0.3	3.65 ± 0.09
PG 1244+026	1.24 ± 0.04	0.28 ± 0.06	0.6 ± 0.3	0.5 ± 0.1	1.0 ± 0.2	0.5 ± 0.2
PG 1307+085	5.1 ± 0.2	1.4 ± 0.7	3.3 ± 0.2	0.7 ± 0.1	1.0 ± 0.2	5.0 ± 0.1
PG 1448+273	0.4 ± 0.5	0.3 ± 0.1	1.8 ± 0.1	0.9 ± 0.1	1.3 ± 0.7	1 ± 1
PG 1613+658	2.9 ± 0.1	1.2 ± 0.6	5.4 ± 0.2	3.2 ± 0.1	1.4 ± 0.5	1.2 ± 0.5
PG 1626+554	1.1 ± 0.7	0.6 ± 0.1	0.6 ± 0.1	0.9 ± 0.7	...	...
PG 2214+139	1.5 ± 0.1	2.8 ± 0.1	1.5 ± 0.1	0.5 ± 0.3	1.2 ± 0.5	0.9 ± 0.2

Table 2.4. 95% Light Radii [kpc]

Object	Opt.	[O II]	H $\beta$	[O III]	Pa $\alpha$	IR
PG 0026+129	1.6 ± 0.1	4.4 ± 0.1	3.7 ± 0.2	4.7 ± 0.2	0.9 ± 0.2	4.3 ± 0.1
PG 0838+770	0.5 ± 0.1	4.6 ± 0.1	0.6 ± 0.1	3.2 ± 0.1	0.9 ± 0.3	3.65 ± 0.09
PG 1244+026	1.24 ± 0.04	0.28 ± 0.06	0.6 ± 0.3	0.5 ± 0.1	1.0 ± 0.2	0.5 ± 0.2
PG 1307+085	5.1 ± 0.2	1.4 ± 0.7	3.3 ± 0.2	0.7 ± 0.1	1.0 ± 0.2	5.0 ± 0.1
PG 1448+273	0.4 ± 0.5	0.3 ± 0.1	1.8 ± 0.1	0.9 ± 0.1	1.3 ± 0.7	1 ± 1
PG 1613+658	2.9 ± 0.1	1.2 ± 0.6	5.4 ± 0.2	3.2 ± 0.1	1.4 ± 0.5	1.2 ± 0.5
PG 1626+554	1.1 ± 0.7	0.6 ± 0.1	0.6 ± 0.1	0.9 ± 0.7	...	...
PG 2214+139	1.5 ± 0.1	2.8 ± 0.1	1.5 ± 0.1	0.5 ± 0.3	1.2 ± 0.5	0.9 ± 0.2

Table 2.5. Integrated Emission Line Luminosities, SFRs, and Masses

Object	$[O\text{ II}]$ $10^{40}\text{erg s}^{-1}$	$H\beta$ $10^{40}\text{erg s}^{-1}$	$[O\text{ III}]$ $10^{40}\text{erg s}^{-1}$	$\text{Pa}\alpha$ $10^{40}\text{erg s}^{-1}$	SFR $M_{\odot}\text{yr}^{-1}$	<sup>a</sup> Masses $M_{\odot}$	<sup>b</sup>
PG 0026+129	$220 \pm 10$	$138 \pm 4$	$262 \pm 7$	$56.1 \pm 0.5$	$21.64 \pm 0.07$	$11.2 \pm 0.2$	
PG 0838+770	$160 \pm 10$	$70 \pm 5$	$40 \pm 3$	$21.0 \pm 0.3$	$17.03 \pm 0.08$	$10.7 \pm 0.2$	
PG 1244+026	$15 \pm 1$	$7.3 \pm 0.4$	$6.2 \pm 0.3$	$2.95 \pm 0.02$	$2.519 \pm 0.009$	$10.2 \pm 0.2$	
PG 1307+085	$450 \pm 40$	$126 \pm 9$	$62 \pm 3$	$57.0 \pm 0.6$	$37.1 \pm 0.1$	$11.2 \pm 0.2$	
PG 1448+273	$200 \pm 10$	$130 \pm 5$	$102 \pm 2$	$19.7 \pm 0.1$	$22.53 \pm 0.05$	$11.0 \pm 0.2$	
PG 1613+658	$760 \pm 50$	$220 \pm 10$	$220 \pm 10$	$91.1 \pm 0.7$	$71.9 \pm 0.2$	$11.3 \pm 0.2$	
PG 1626+554	$127 \pm 3$	$119 \pm 2$	$50 \pm 2$	...	$21.90 \pm 0.03$	$10.9 \pm 0.2$	
PG 2214+139	$300 \pm 60$	$97 \pm 6$	$85 \pm 5$	$31.6 \pm 0.2$	$27.64 \pm 0.06$	$11.1 \pm 0.2$	

<sup>a</sup>Derived from an average of  $H\beta$  and  $\text{Pa}\alpha$  luminosities<sup>a</sup>Derived from infrared continuum luminosities.

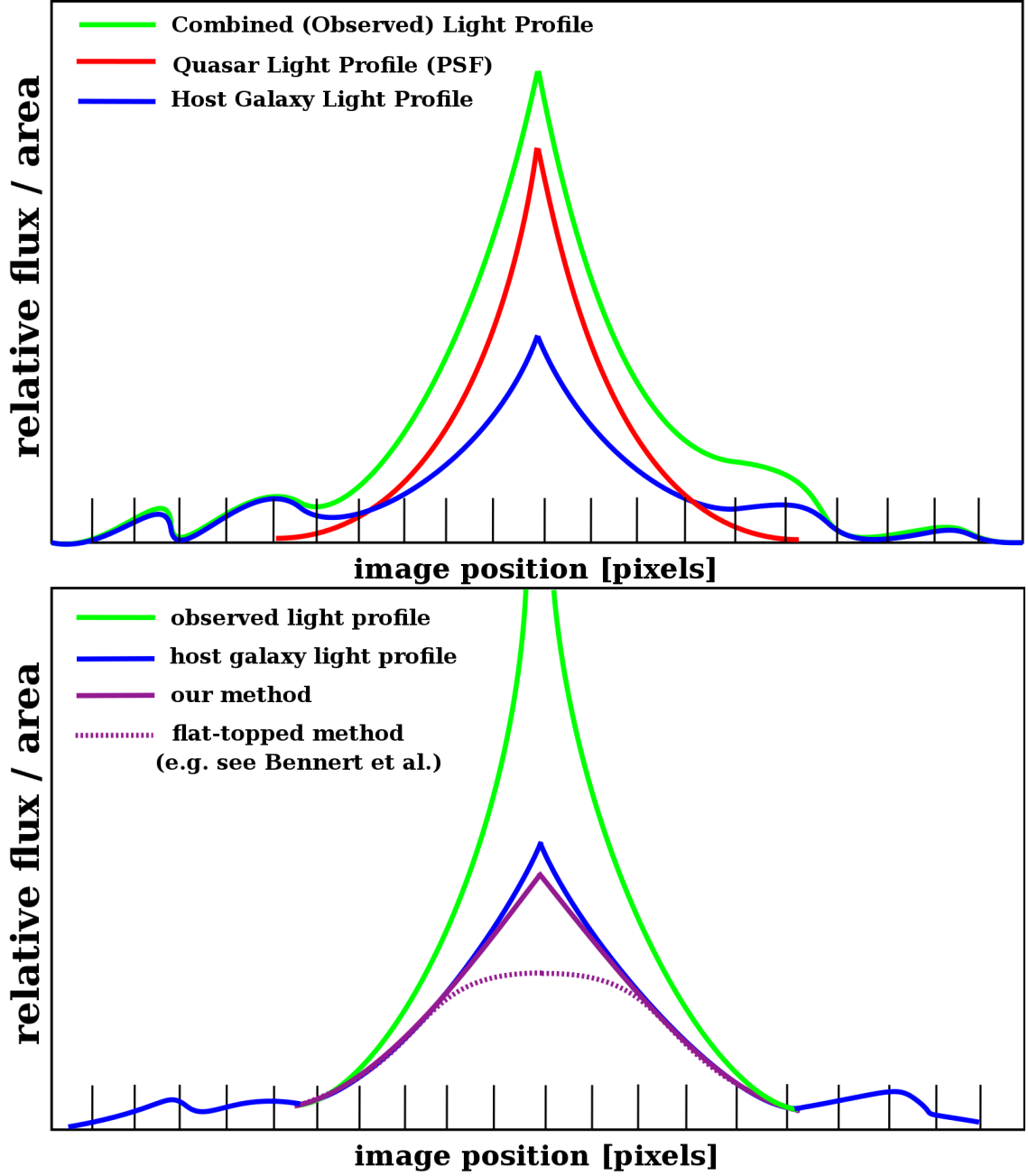


Figure 2.1: A diagram of the light profiles discussed in Section 2.4. **Above:** The observed radial light profile of a quasar + host galaxy is compared to its two components, the quasar PSF and the underlying galaxy light profile. The galaxy light profile is broader, making possible the PSF removal method described in Section 2.4. **Below:** The galaxy light profile from the top figure is compared to its best estimate using two different PSF subtraction methods, the method described in this work, and the method described in ?. Note that the curves presented in this figure are visual aids only, and do not represent actual data. In reality, the quasar PSF profiles are up to 10 $\times$  higher than the galaxy light profiles.

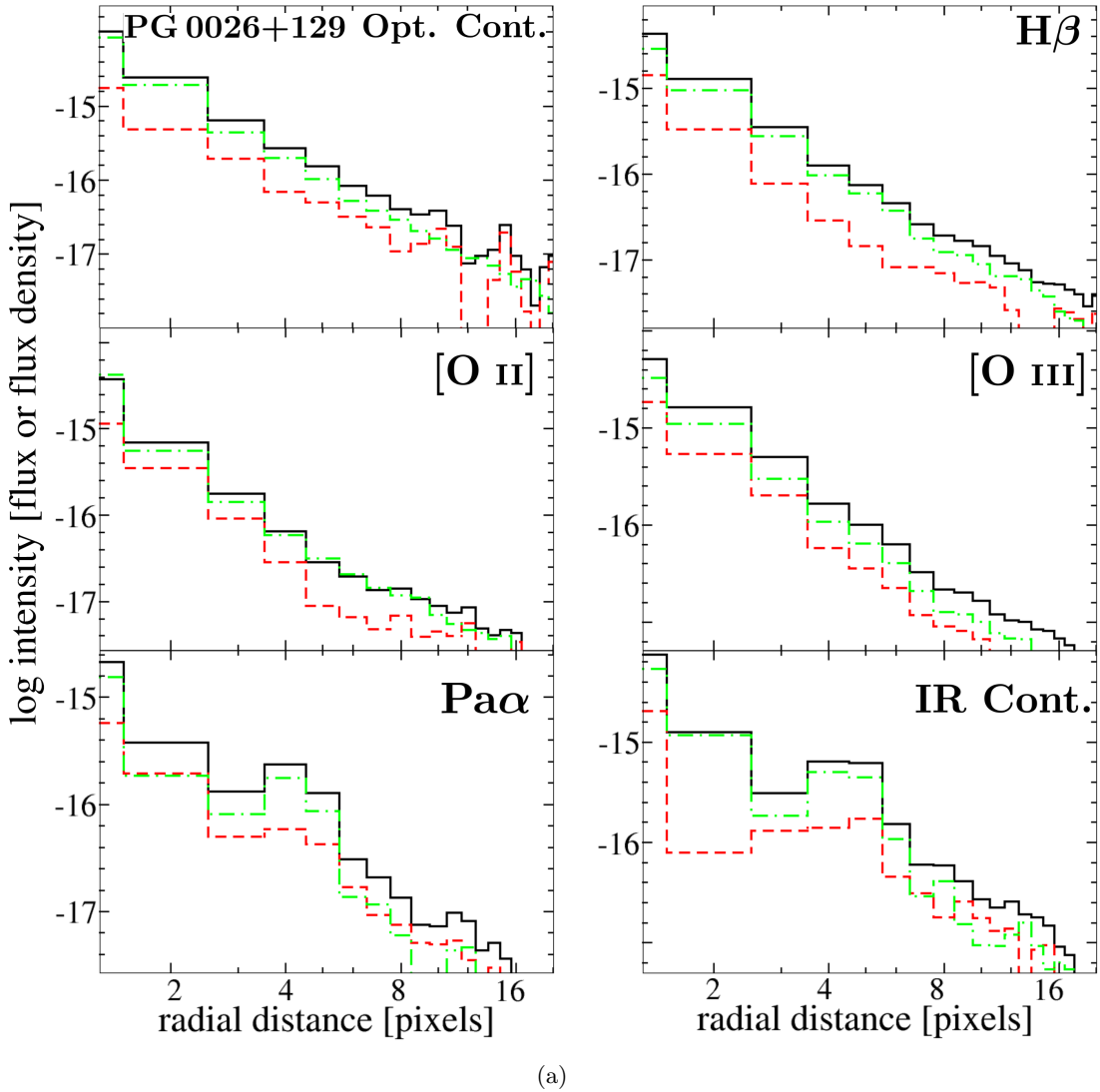


Figure 2.2: Azimuthally averaged light profiles of the PG 0026+129 host galaxy in each wavelength of interest, the corresponding quasar PSF (the light profile of a PSF star properly rescaled), and the residual galaxy after subtraction.

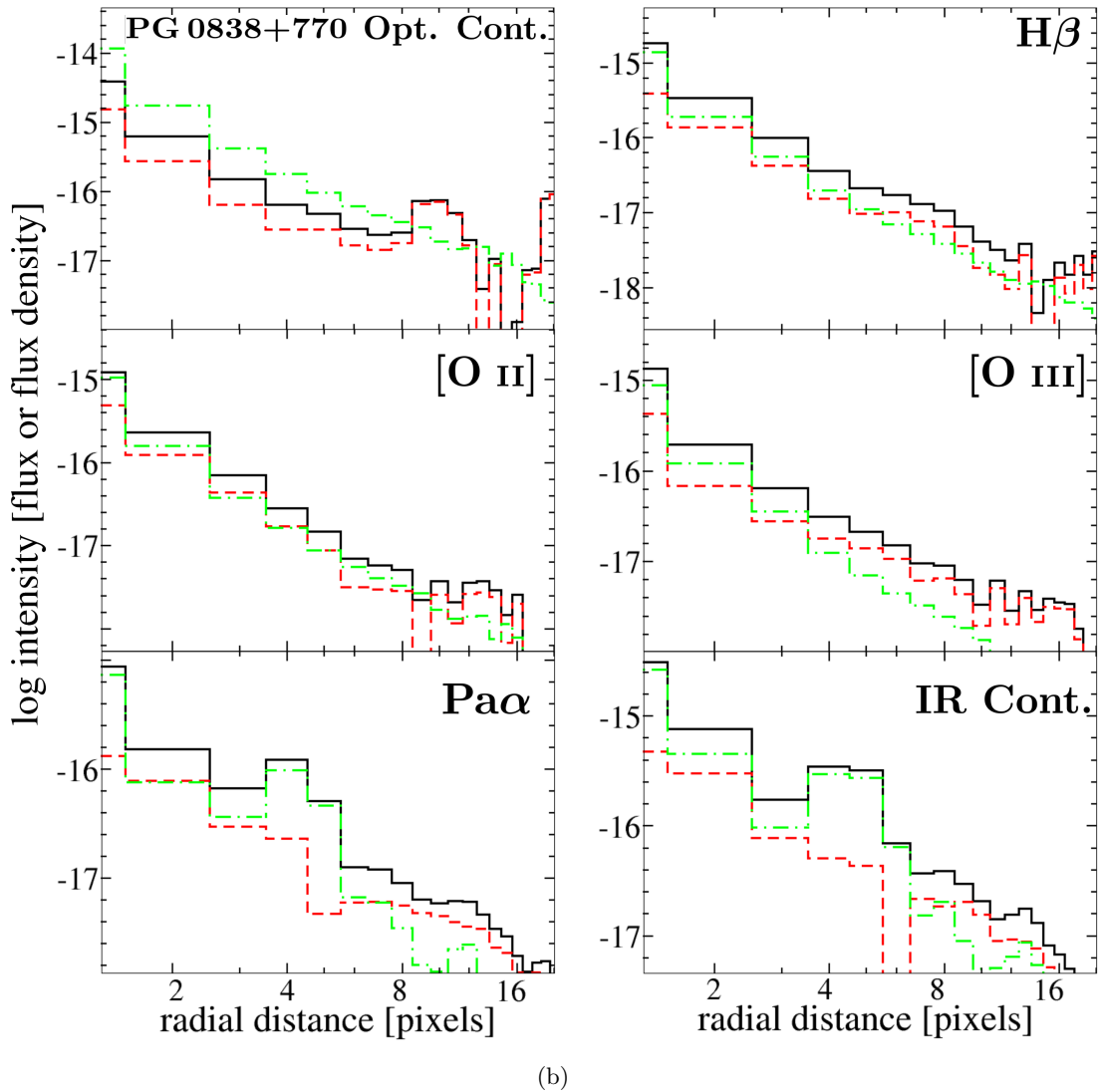


Figure 2.2: Same as Figure 2.2(a), but for PG 0838+770.

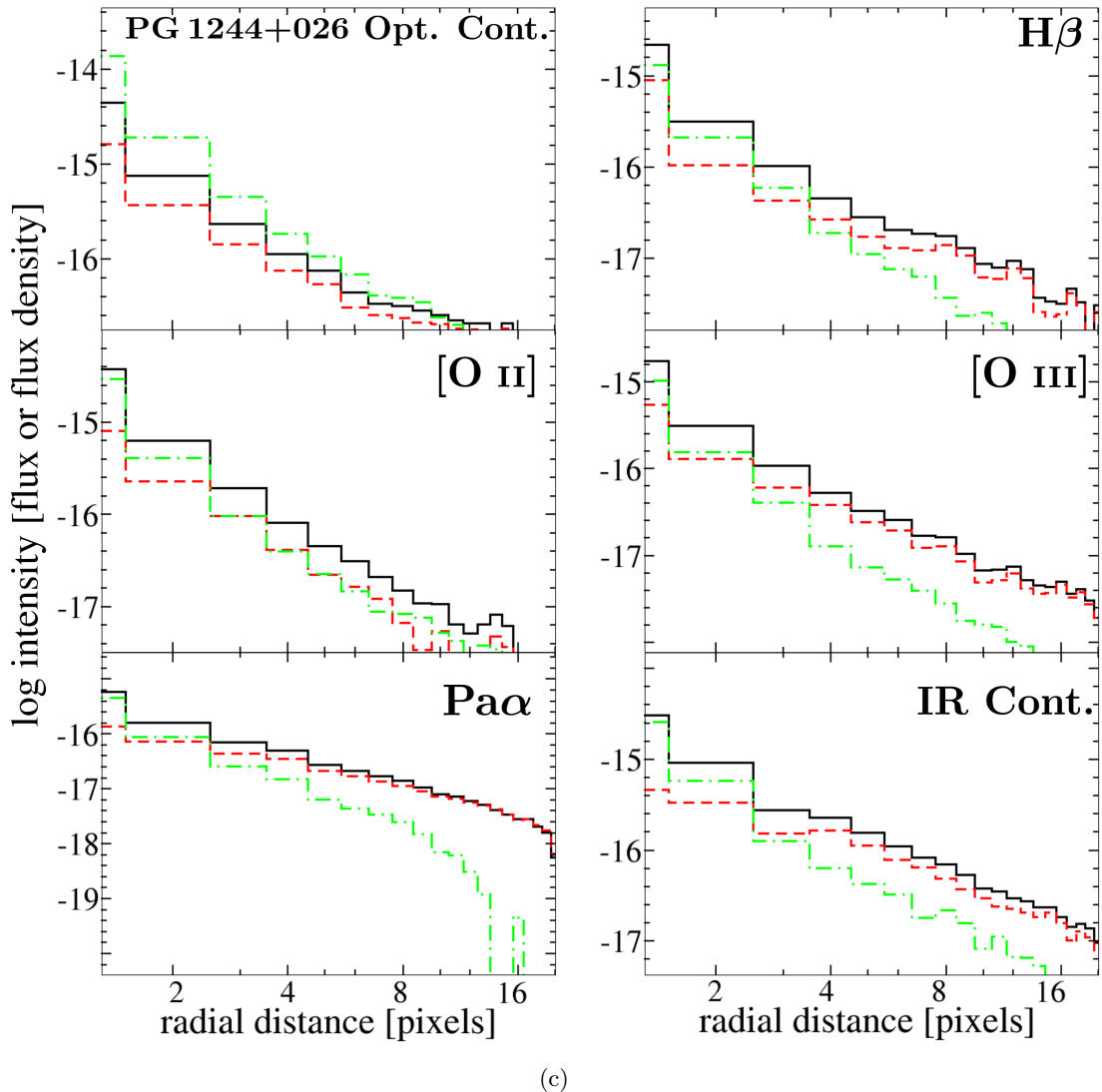
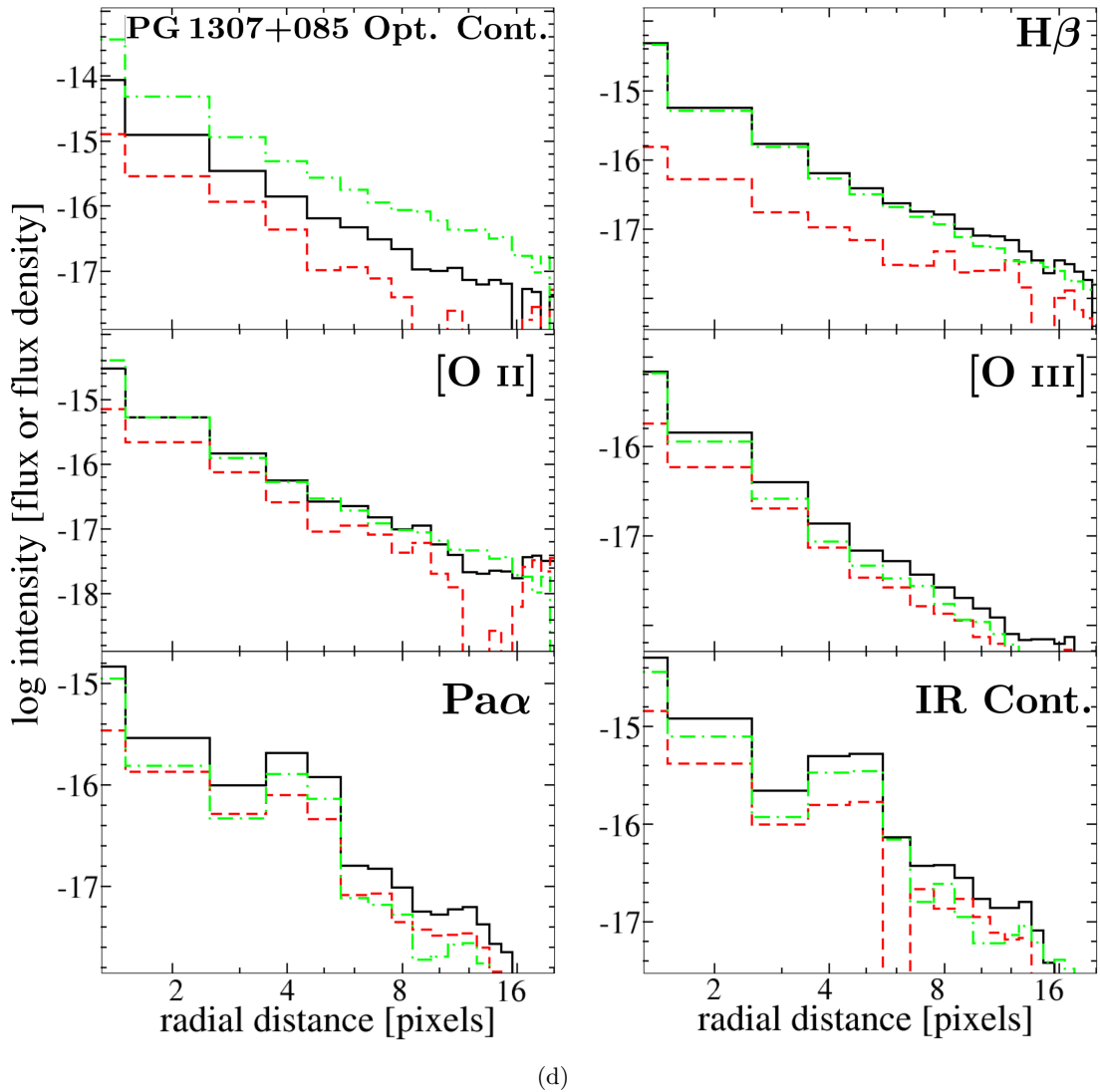


Figure 2.2: Same as Figure 2.2(a), but for PG 1244+026.



(d)

Figure 2.2: Same as Figure 2.2(a), but for PG 1307+085.

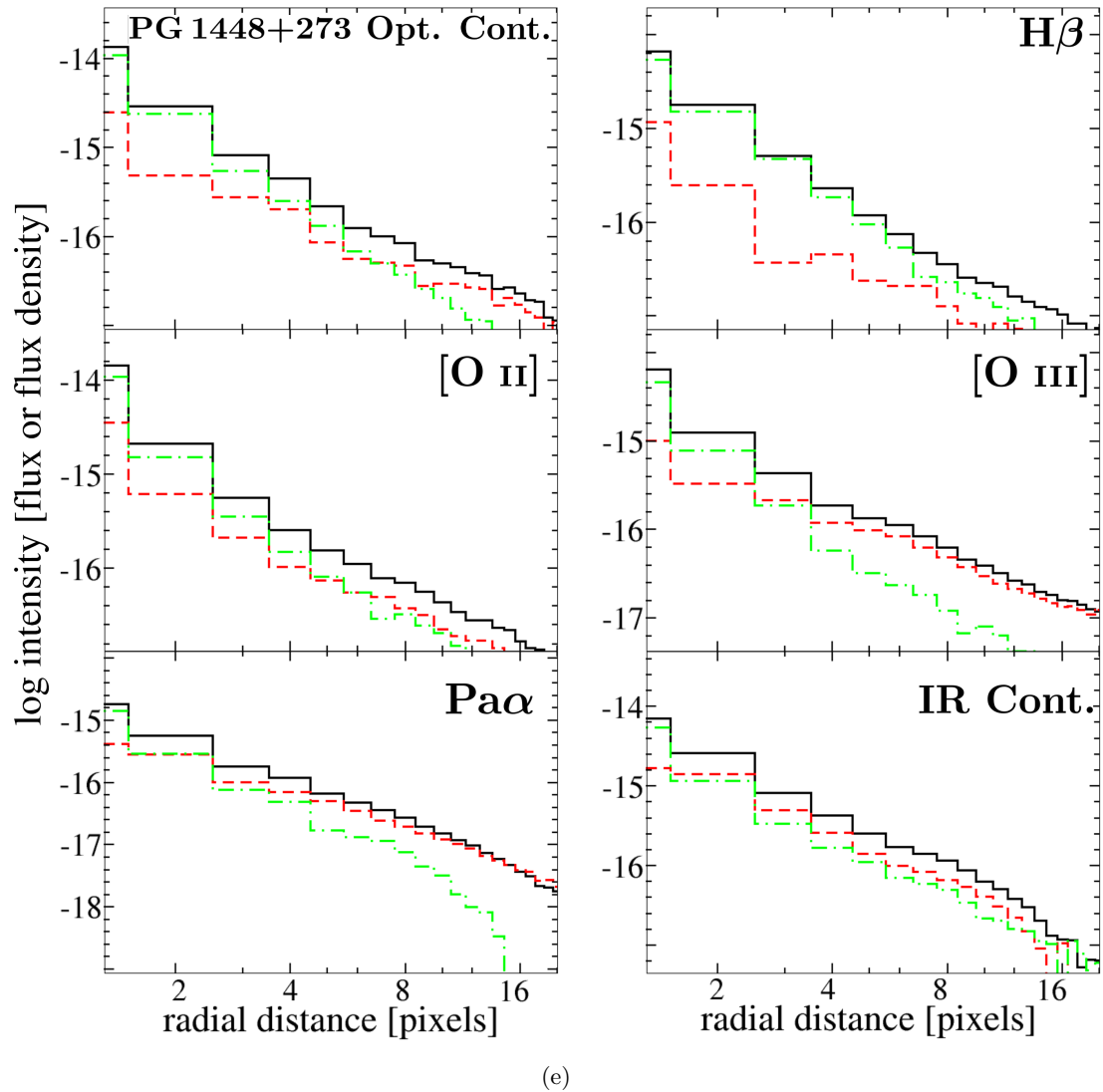
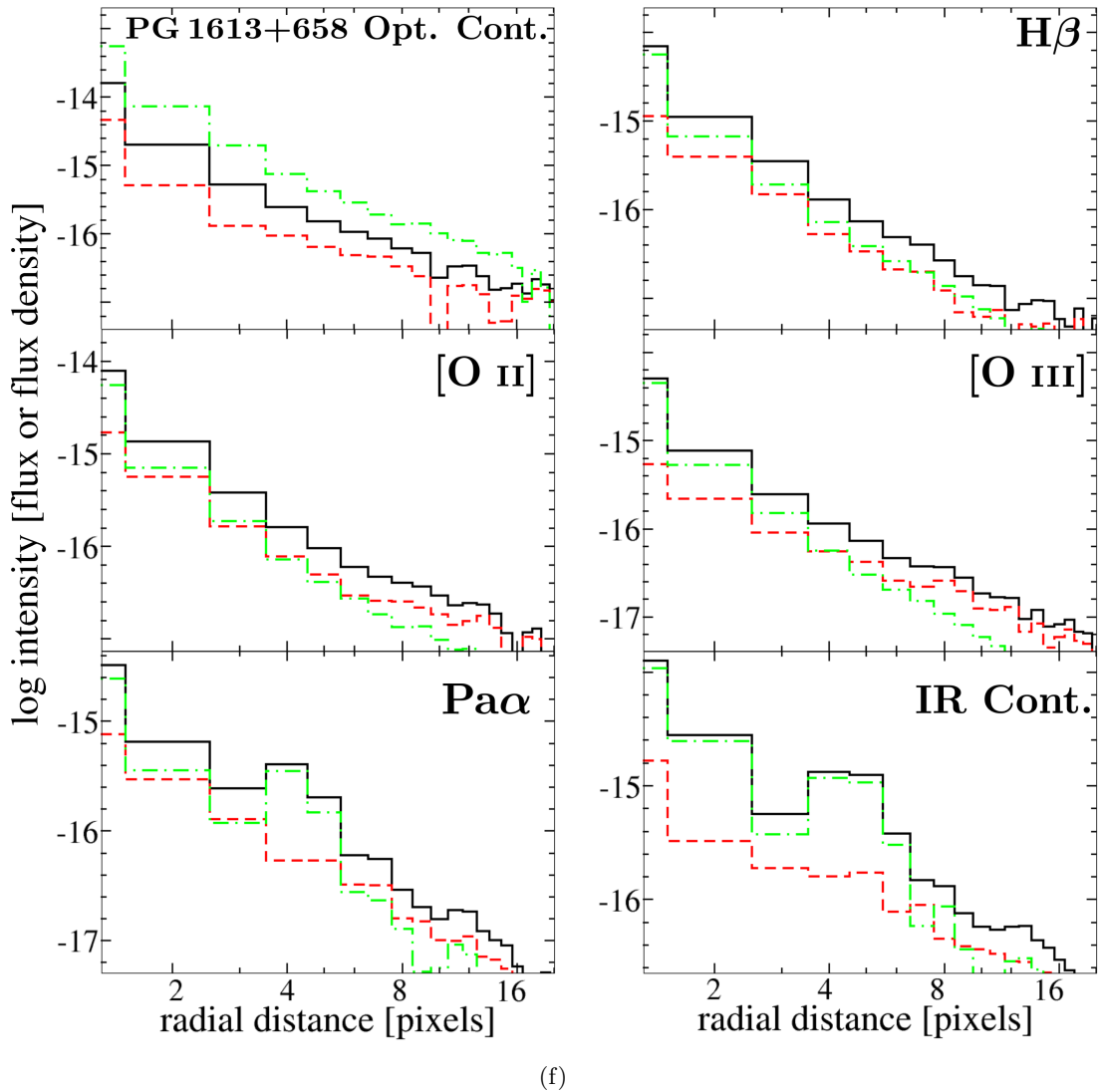


Figure 2.2: Same as Figure 2.2(a), but for PG 1448+273.



(f)

Figure 2.2: Same as Figure 2.2(a), but for PG 1613+658.

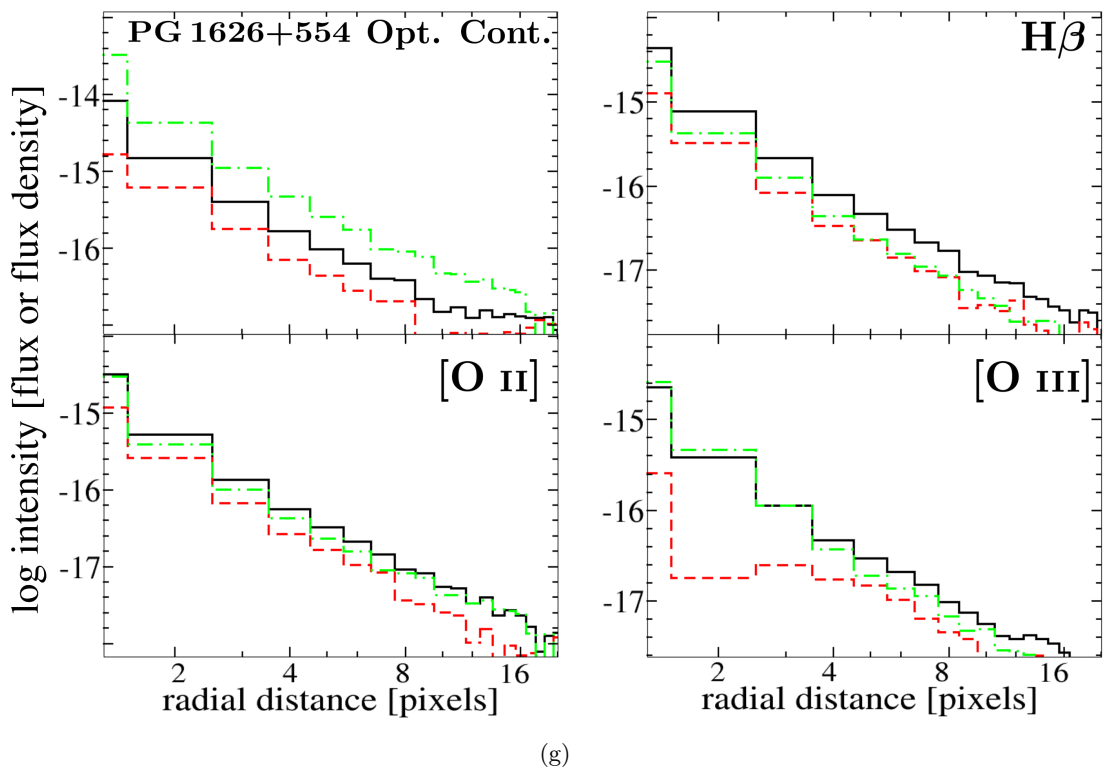


Figure 2.2: Same as Figure 2.2(a), but for PG 1626+554. Note the infrared images are missing due to the failure of the NICMOS instrument.

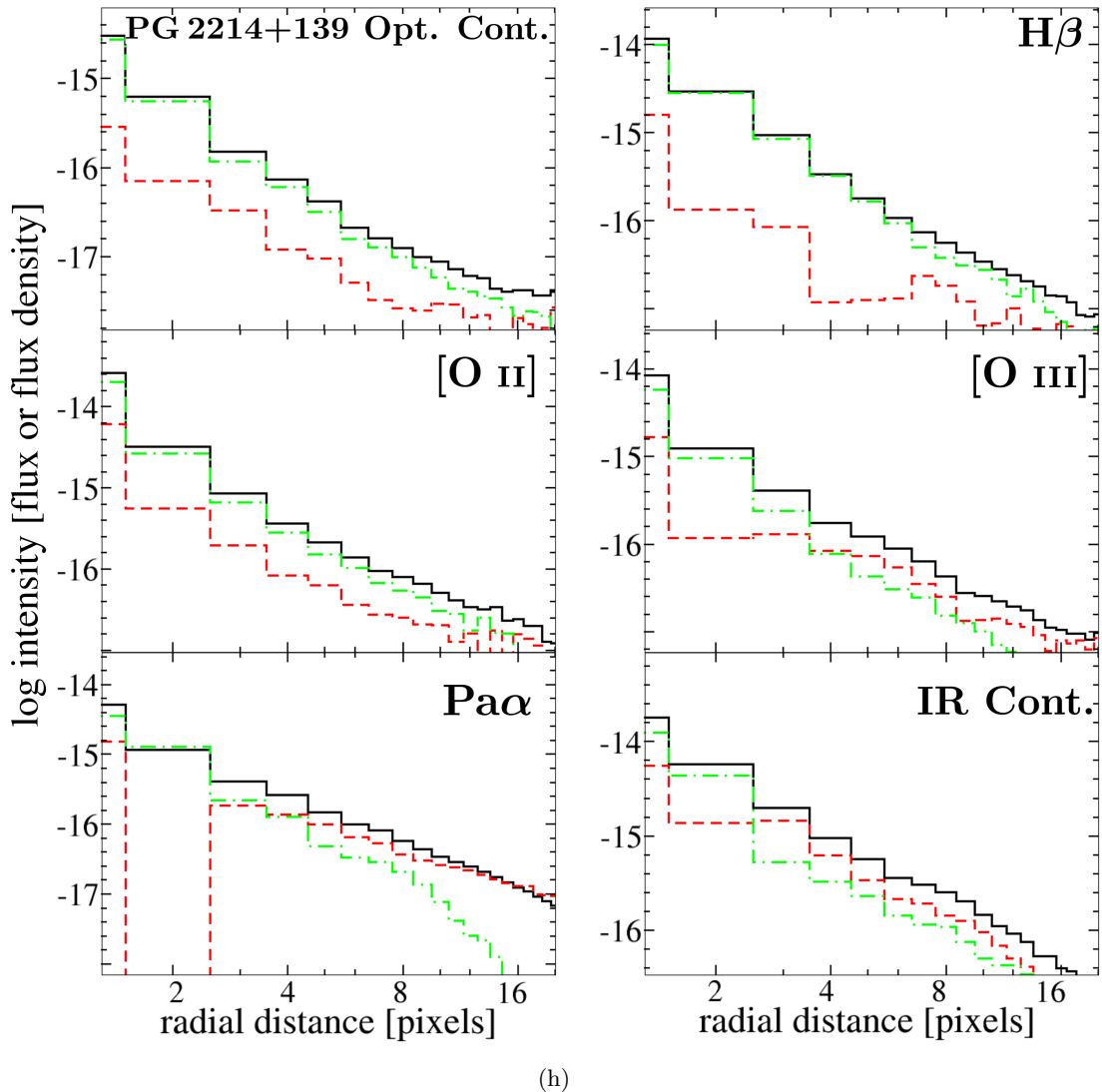
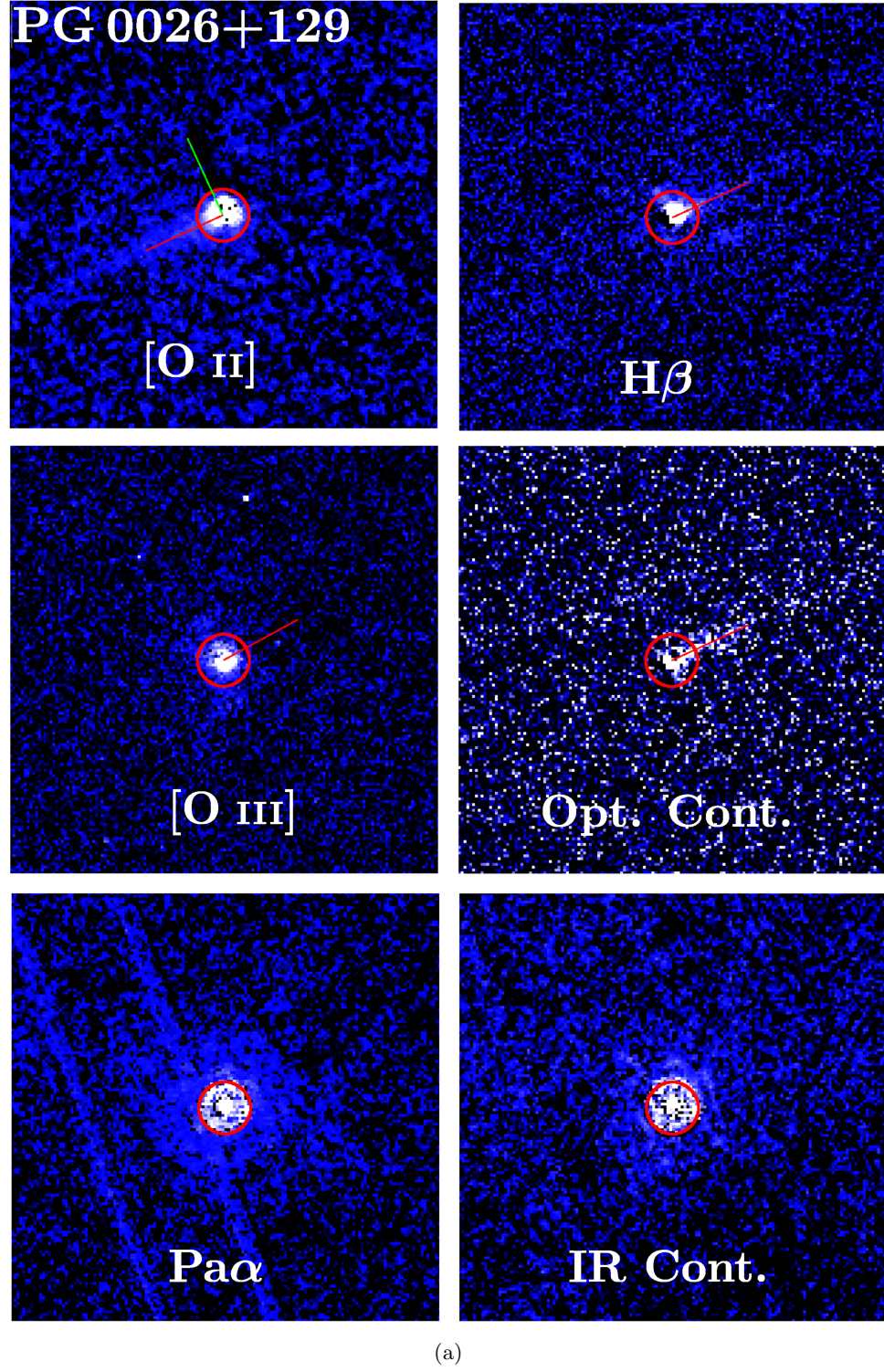


Figure 2.2: Same as Figure 2.2(a), but for PG 2214+139.



(a)

Figure 2.3: PSF-subtracted images of PG 0026+129 in each of the filters used. The red circle is 1 kpc at the distance of the quasar. Each tile is  $7''.5 \times 7''.5$ . The red line indicates the direction of the WFPC2 streak in the quasar images. The WFPC2 streak in the PSF images often aligns with the streak in the quasar images; when otherwise, it is indicated by a green line.

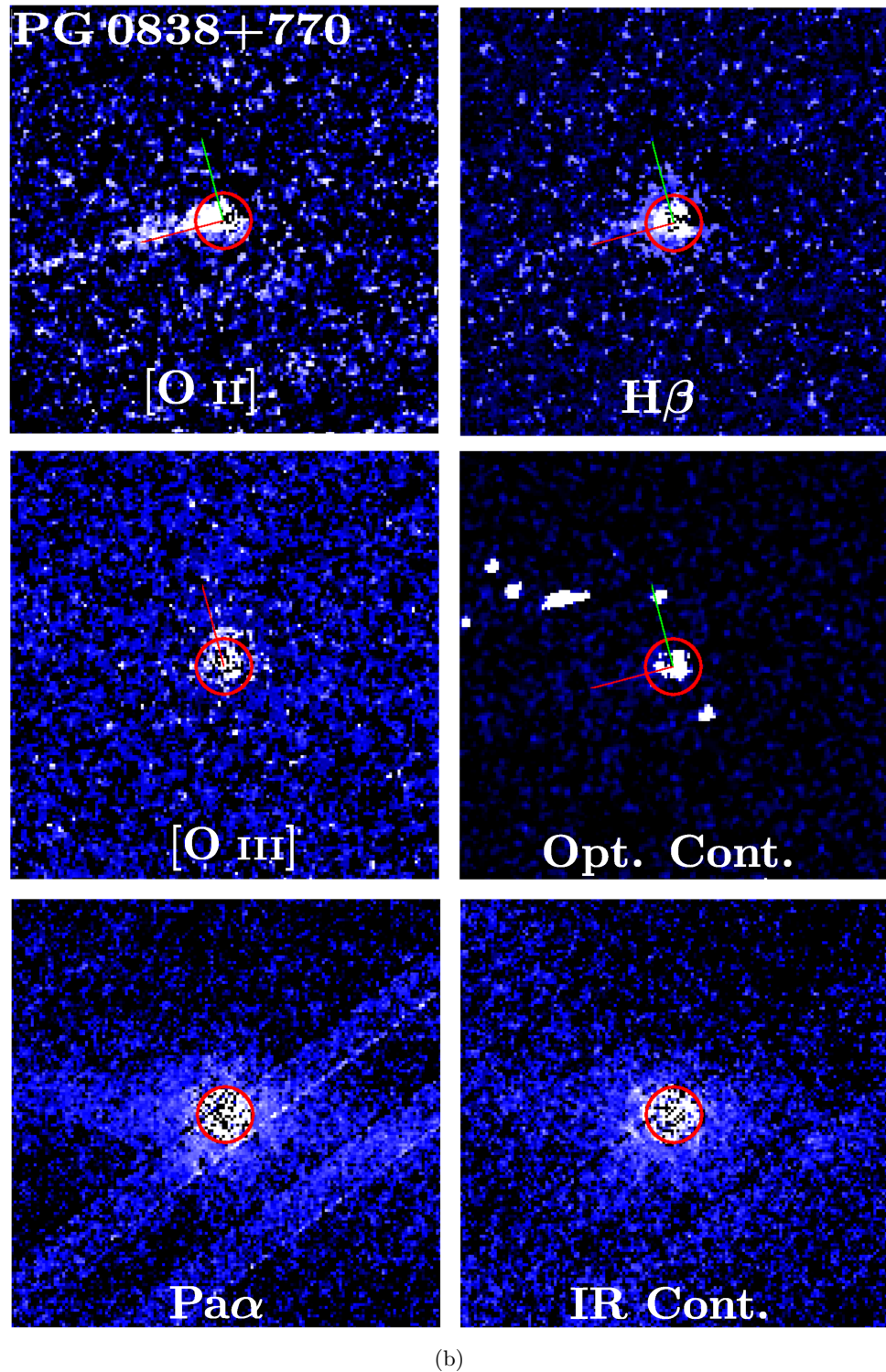


Figure 2.3: Same as Figure 2.3(a), but for PG 0838+770.

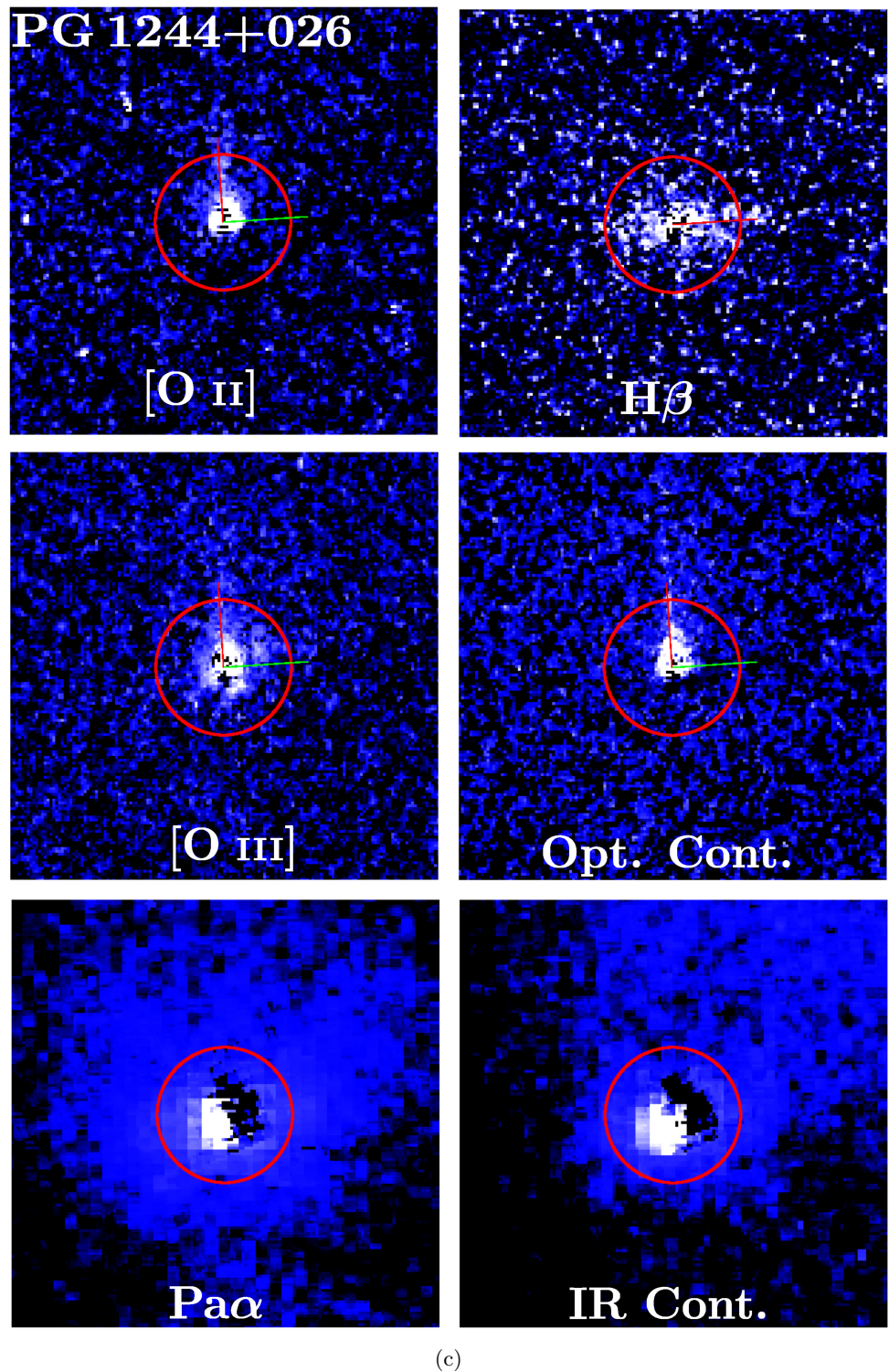


Figure 2.3: Same as Figure 2.3(a), but for PG 1244+026.

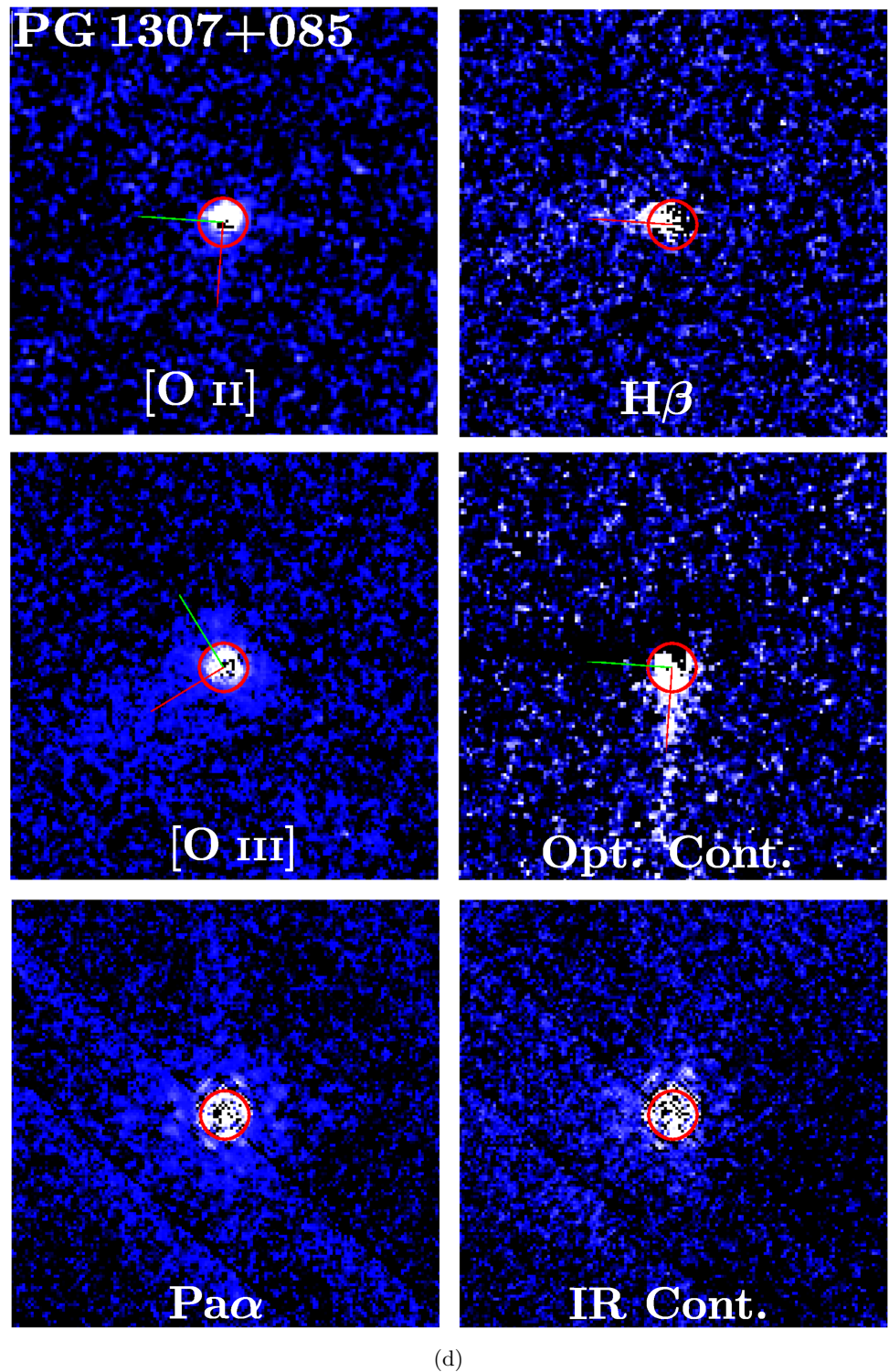


Figure 2.3: Same as Figure 2.3(a), but for PG 1307+085.

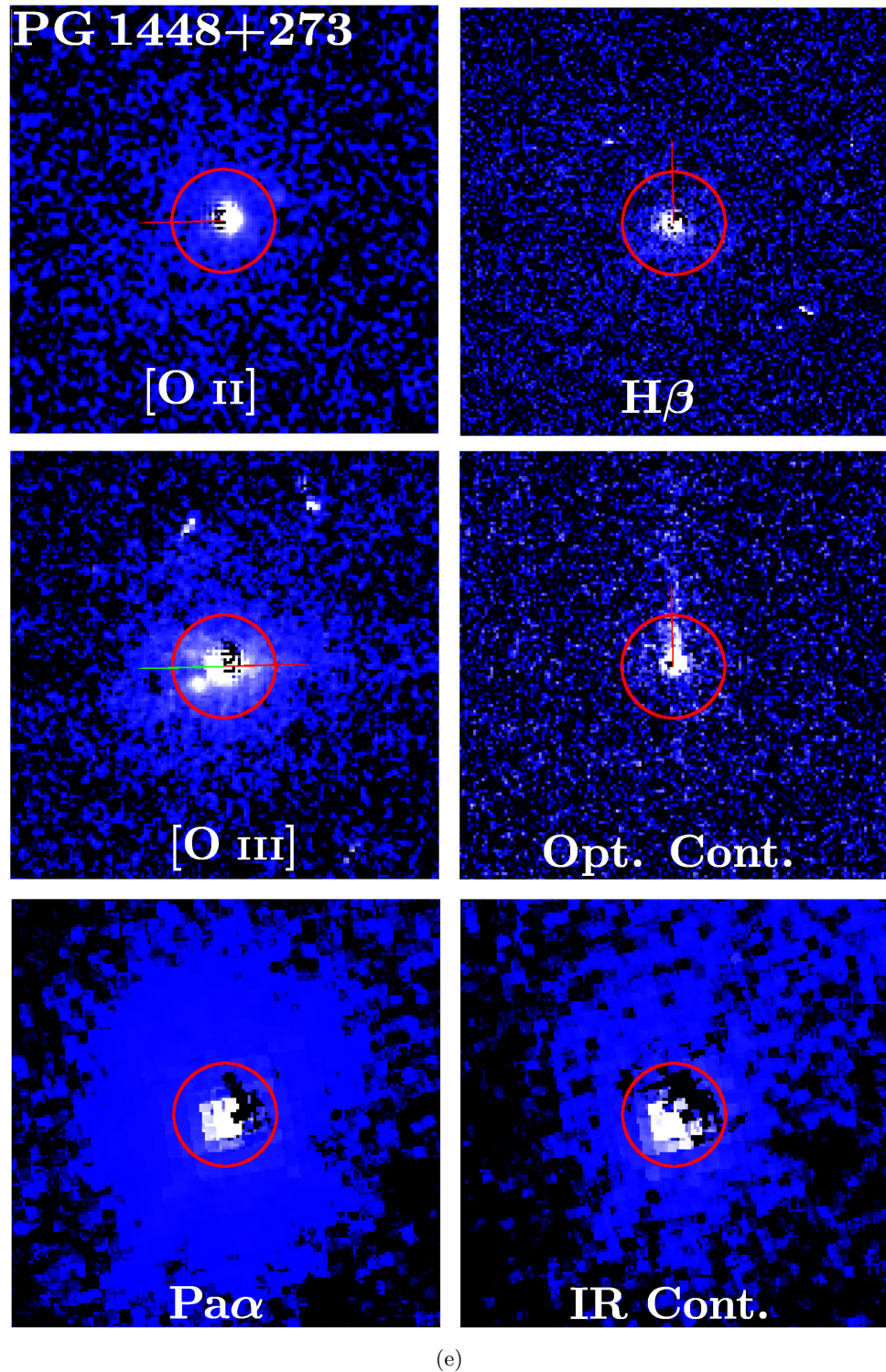


Figure 2.3: Same as Figure 2.3(a), but for PG 1448+273.

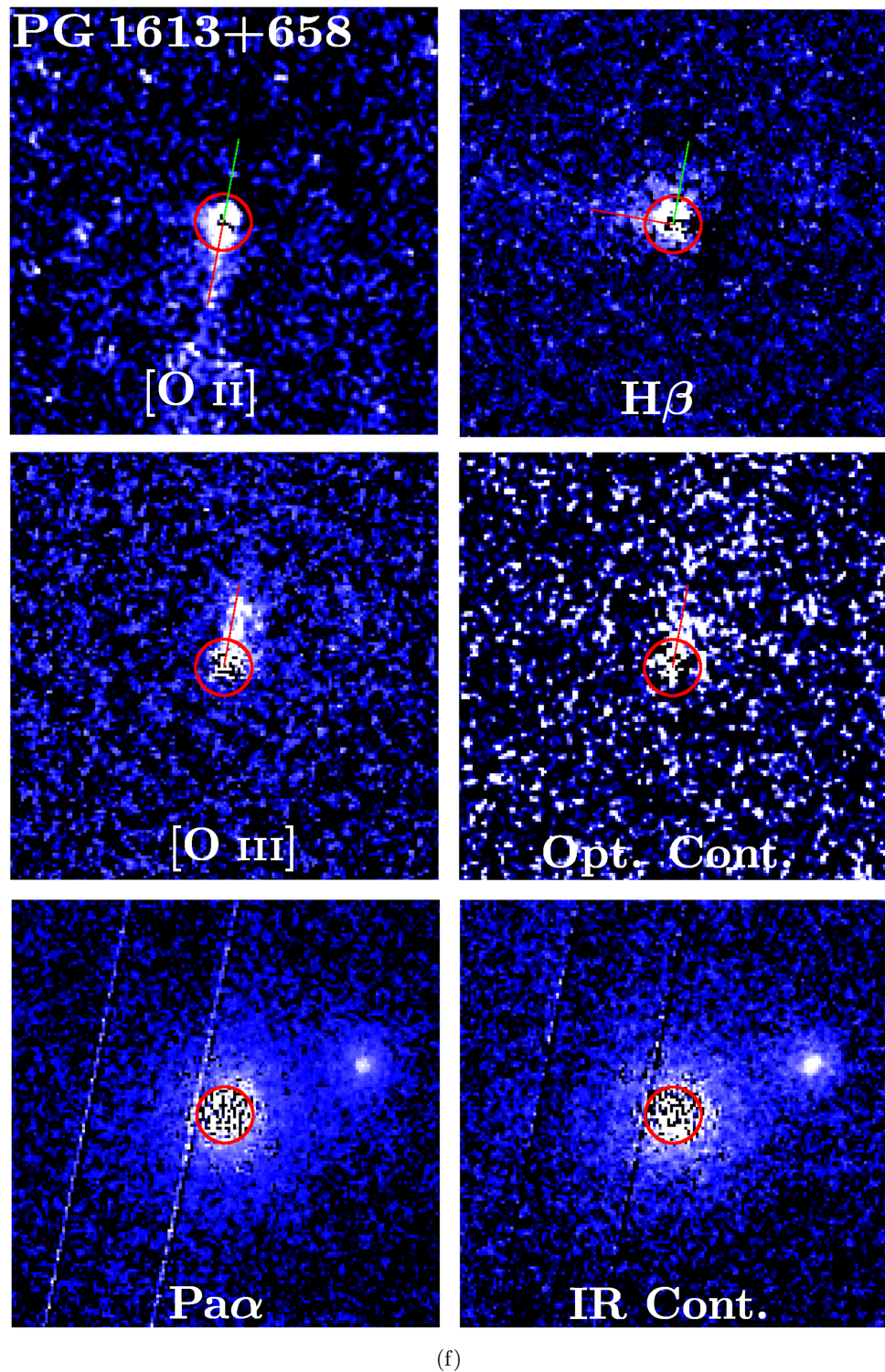
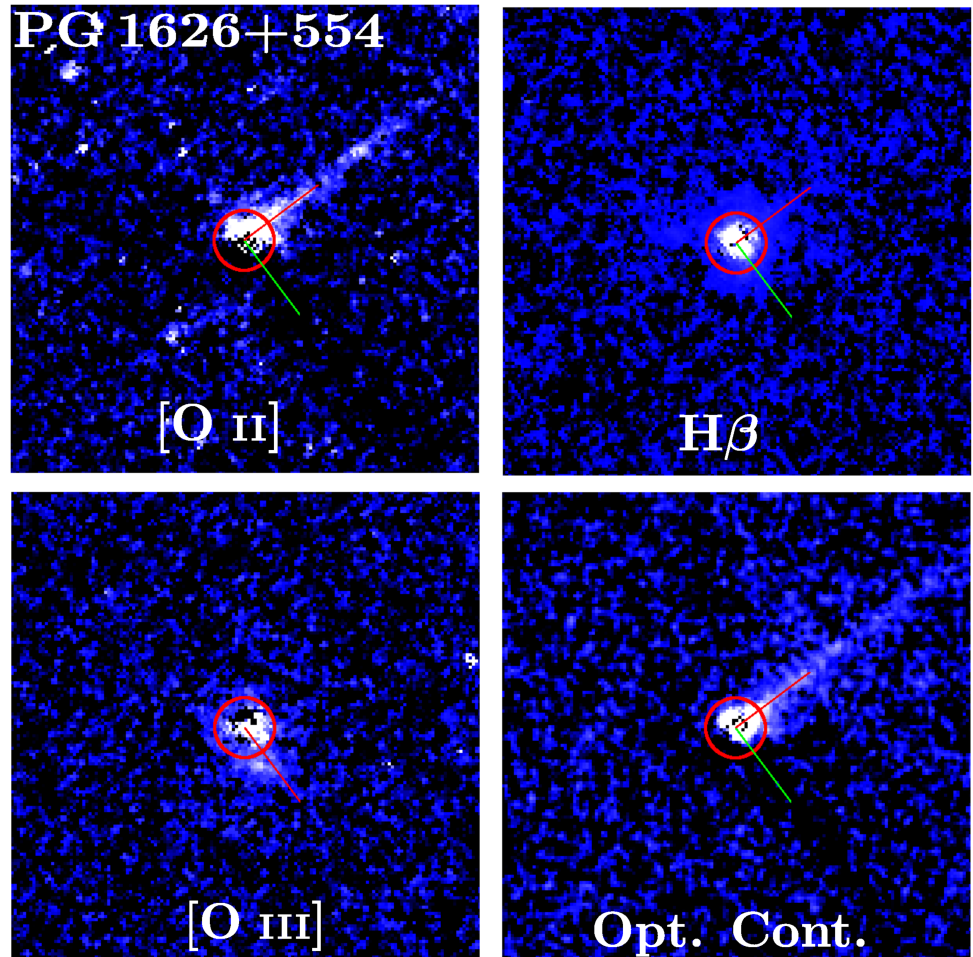


Figure 2.3: Same as Figure 2.3(a), but for PG 1613+658.



(g)

Figure 2.3: Same as Figure 2.3(a), but for PG 1626+554. Note the infrared images are missing due to the failure of the NICMOS instrument.

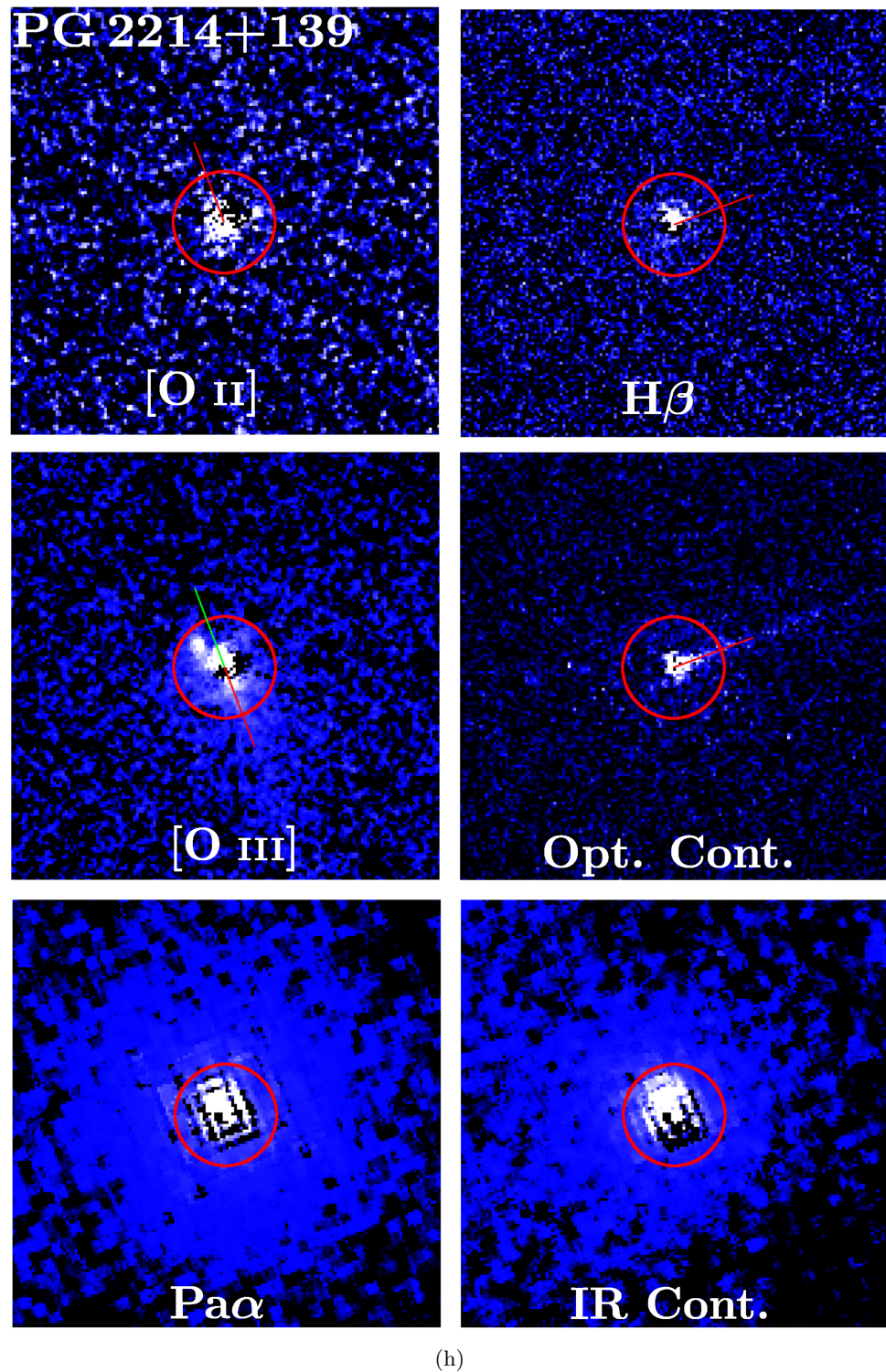


Figure 2.3: Same as Figure 2.3(a), but for PG 2214+139.

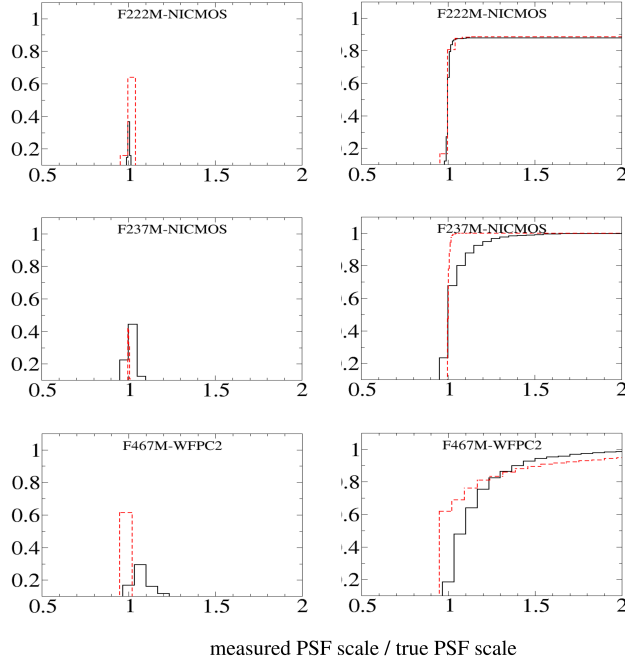


Figure 2.4: For each of the medium-band filters used to sample the quasar host galaxy stellar continuum, a distribution of ratios of computed to true PSF scale factors for 1000 artificial quasar+galaxy pairs using the observed and synthetic (TinyTim) PSF stars. A value of unity indicates the PSF-subtraction algorithm correctly determined, based on image characteristics alone, the intensity of the quasar PSF. In each case the dashed line is the cumulative distribution. Note that the distributions in all three filters peak around unity, indicating that the algorithm is likely to converge on an accurate value. For scale factors ratios less than unity, the median values are 0.99, 0.99, and 0.98 for the F222M, F237M, and F467M filters, respectively, indicating high confidence in host galaxy detections. For scale factor ratios greater than unity, the median values were 1.006, 1.03, and 1.1 for the same filters, indicating photometric uncertainties of 10% or less for worst-case-scenarios; see Section 2.5 for details.

$$\text{SFR } (M_{\odot} \text{ yr}^{-1}) = 7.9 \times 10^{-42} L(H\alpha) \text{ (ergs s}^{-1}\text{)}$$

Figure 2.5: Maps of  $A_V$  for the seven quasars of the eight for which I possess both  $H\beta$  and  $\text{Pa}\alpha$  images; the green circle marks 1 kpc radius.

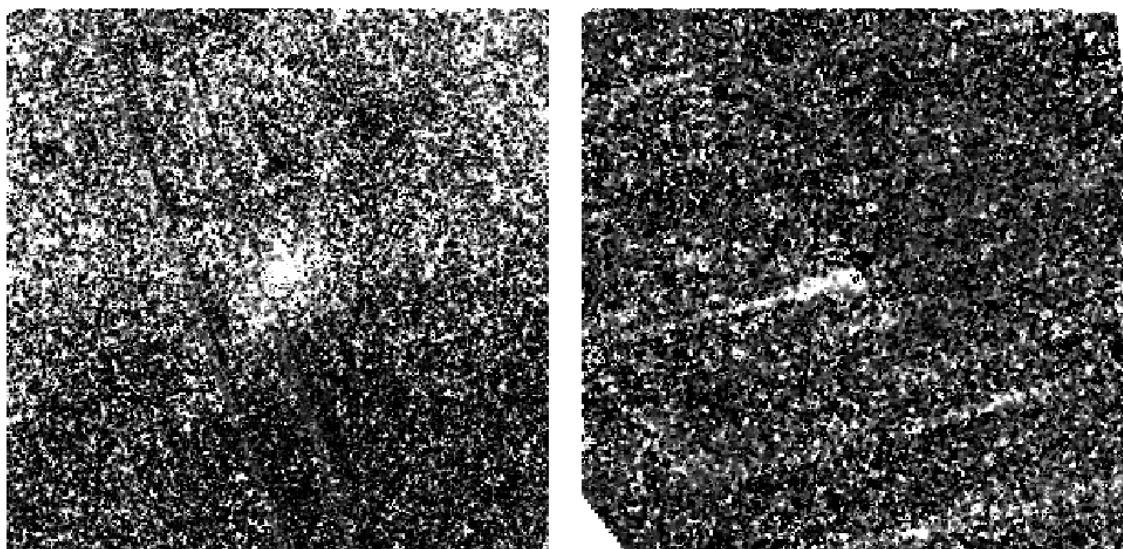


Figure 2.6: Typical uncertainty maps, (left) PG 0026+129 infrared continuum, and (right) PG 0838+770 [O II]. The objects remain visible because the higher count rates result in larger counting uncertainties. Note the cobbled appearance in both images, especially away from the center. This is correlated noise introduced while correcting for extinction. It is produced partly by drizzling the larger NICMOS pixels onto the smaller PC plate scale, and partly produced by the binning of the H $\beta$  and Pa $\alpha$  images in the line-ratio map.

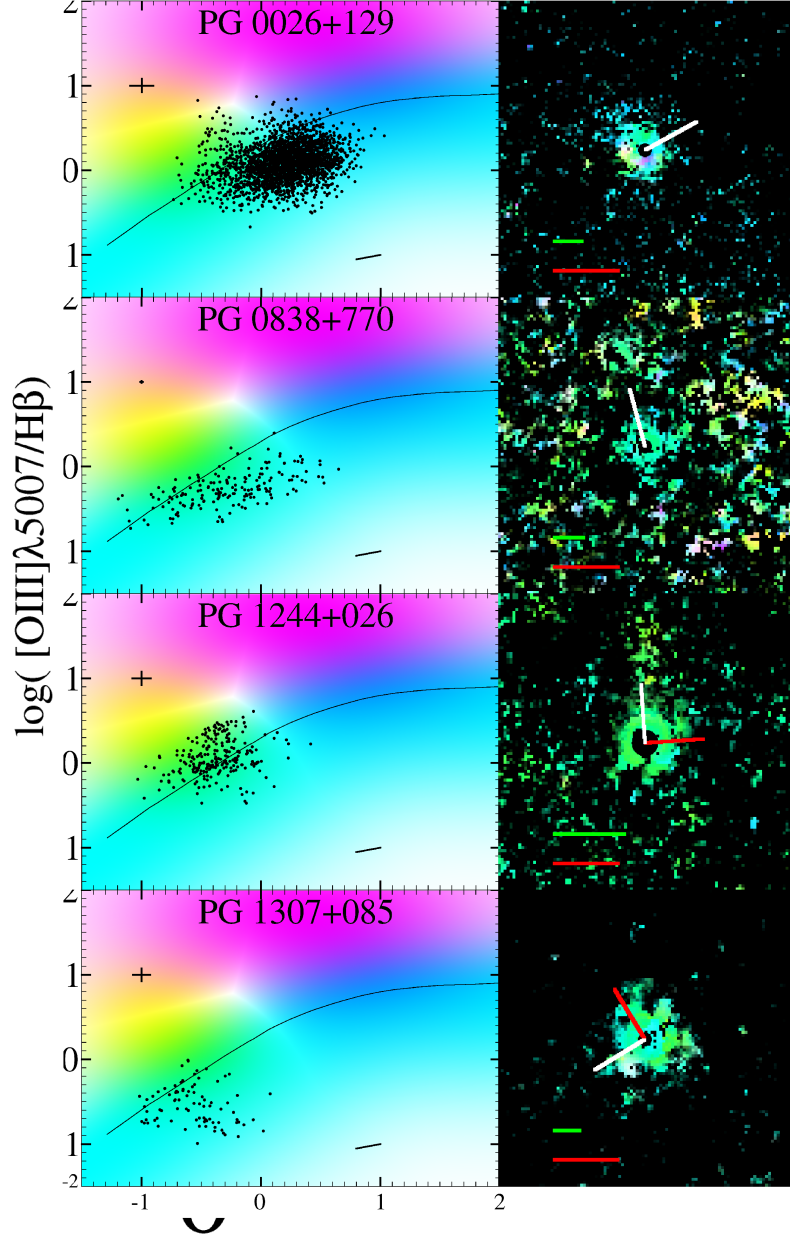


Figure 2.7: Diagnostic Line-Ratio diagrams and maps for the quasar host galaxies. The background of each line-ratio diagram is shaded based on line-emission source: red for AGN, blue for star formation, green for shocks, and intermediate colors for intermediate or ambiguous cases. The line-ratio maps are greyscale  $H\beta$  images of the host galaxies with each pixel multiplied by the color vector from its location in the line-ratio diagnostic diagram. At the bottom of each line-ratio map a red line is drawn to indicate 1 arcsecond, and a green line is drawn to indicate 1 kpc at the distance of the quasar. A black dot is placed at the center of each map to indicate the region where uncertainties in PSF subtraction dominate. A reddening track of two magnitudes in  $A_V$  is plotted near the lower right in each diagnostic diagram; the track points to the lower left.

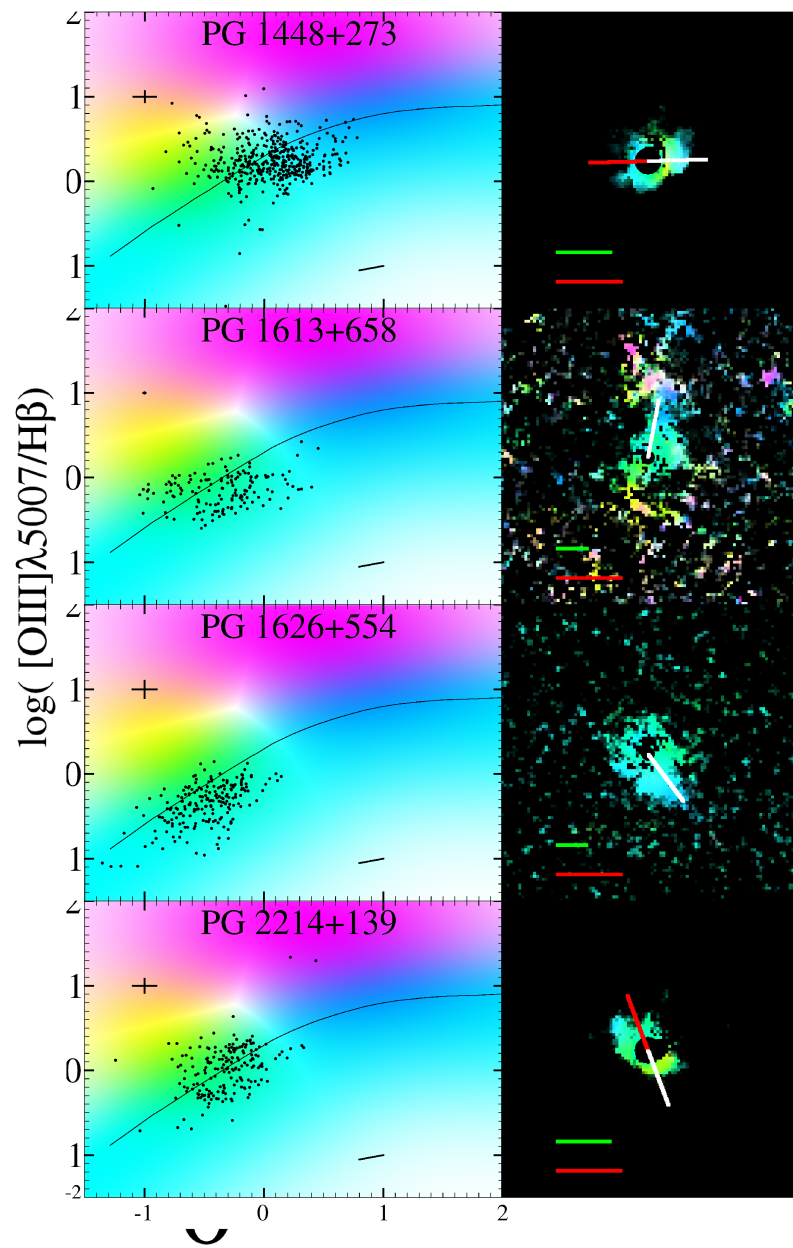


Figure 2.7: Same as Figure 6a, but for the next four objects.

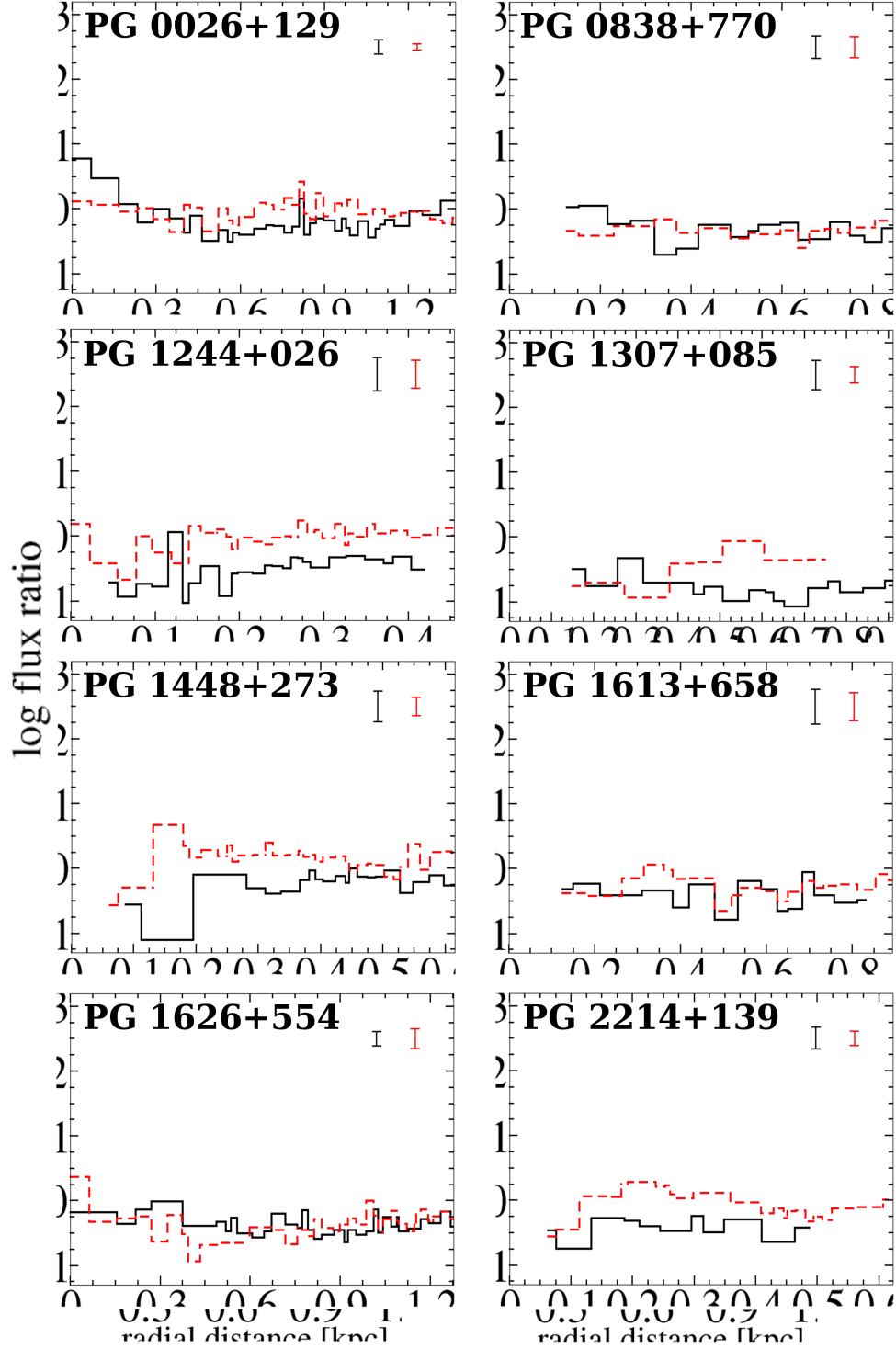


Figure 2.8: Azimuthally averaged line ratios plotted as a function of radius from the galactic center. The black, solid line is the  $[O\text{ III}]/[O\text{ II}]$  ratio, while the red dashed line is the  $[O\text{ III}]/H\beta$  ratio. As in Figure 2.7(a),  $\log[O\text{ III}]/[O\text{ II}] \gtrsim 1$  ratio near the nucleus indicates the presence of a narrow-line region for reasons discussed in Section 2.8.1 and ?.

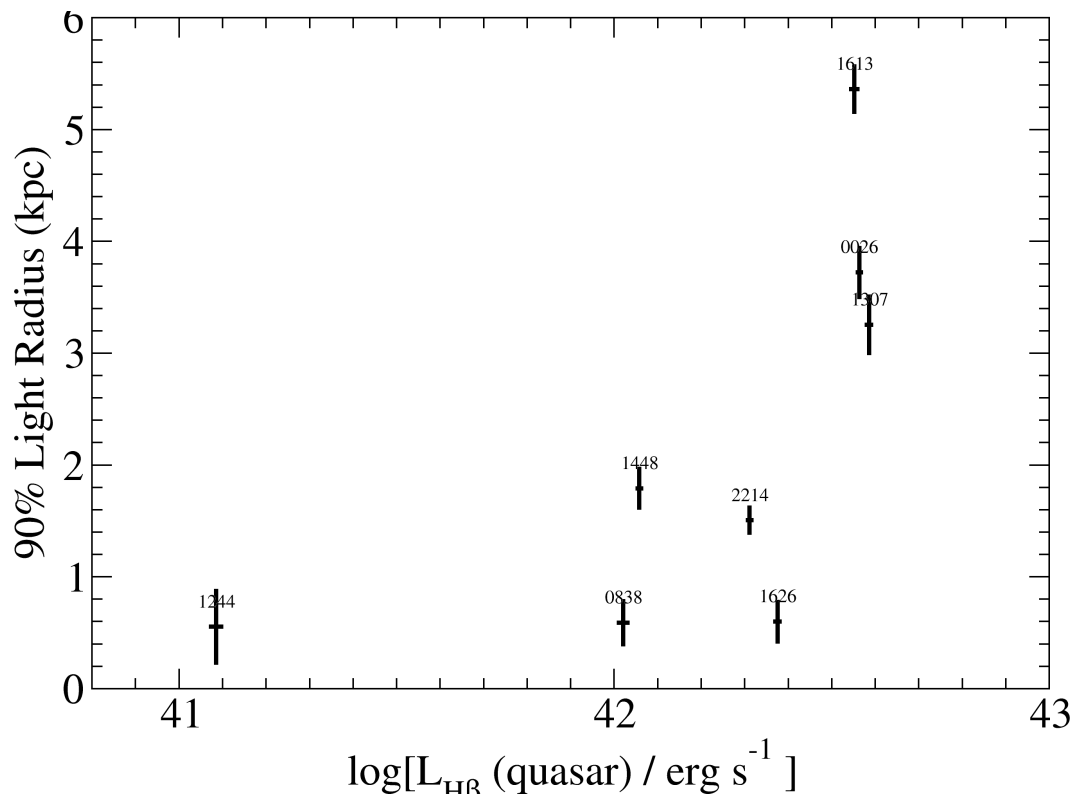


Figure 2.9: H $\beta$  emission line region 90% light radii vs. quasar H $\beta$  luminosities. The quasar luminosities were the portion of the light removed from the H $\beta$  images by the PSF subtraction process.

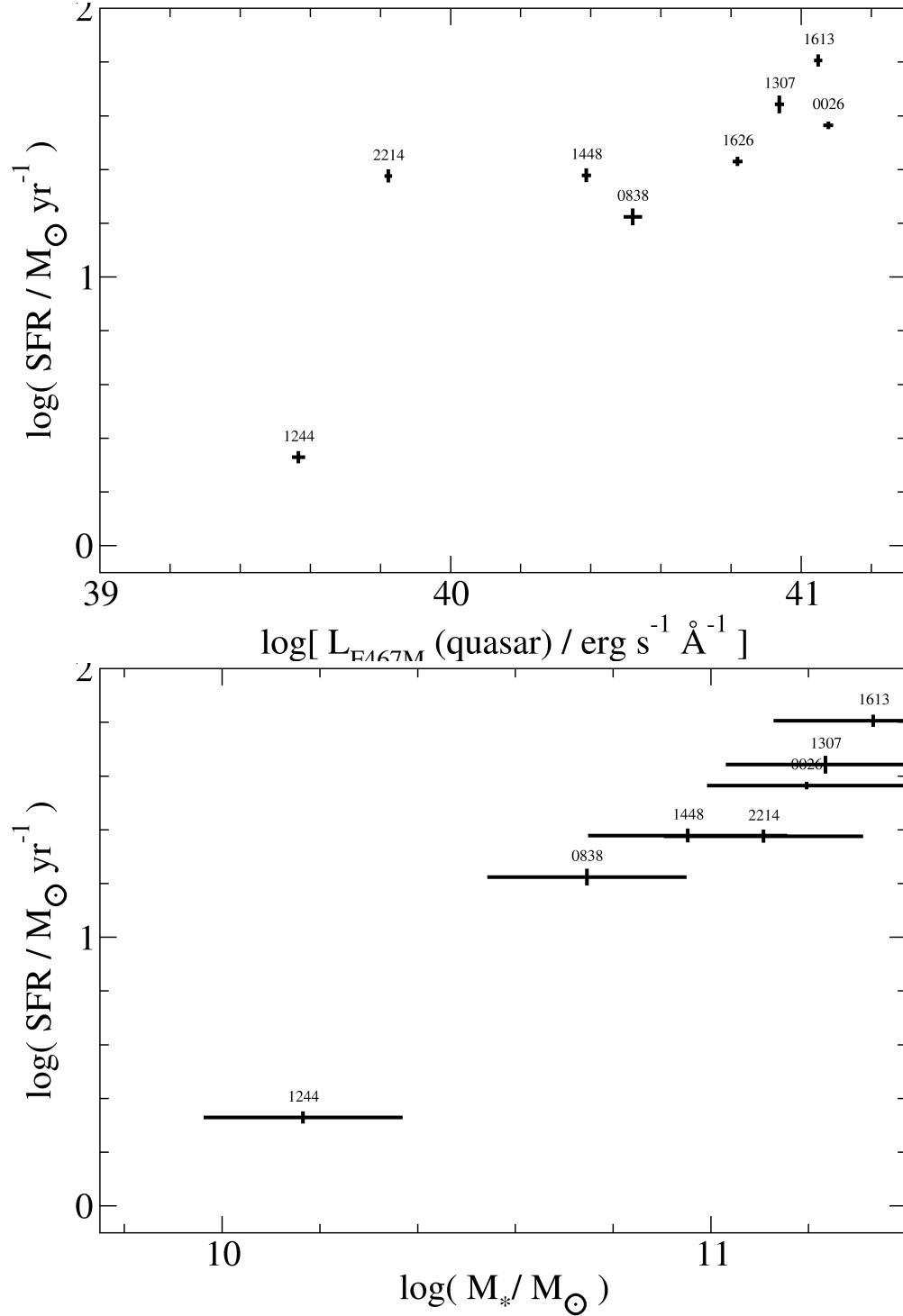


Figure 2.10: Plots of star-formation rates vs. quasar optical continuum luminosity (top) and galaxy stellar mass (bottom). The quasar optical continuum luminosities were the portion of the light removed from the optical continuum images of the quasars by the PSF subtraction. The galaxy stellar masses are infrared continuum luminosities rescaled using mass-to-light ratios.

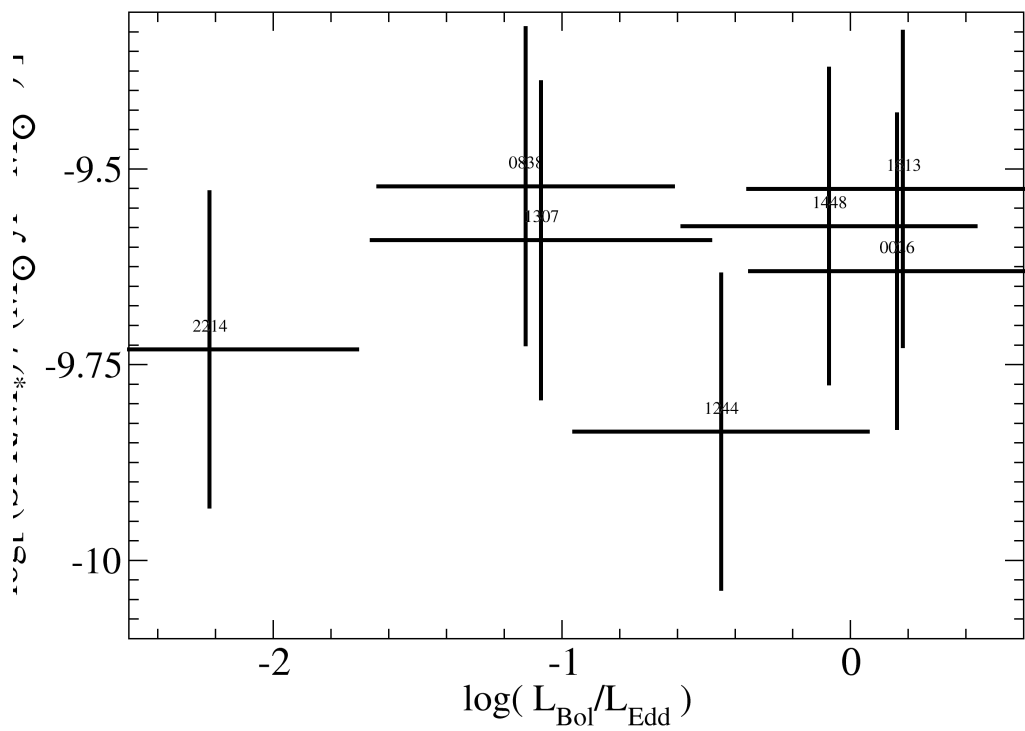


Figure 2.11: Plot of star-formation rate per stellar mass vs. quasar Eddington Ratio. The Eddington Ratios were derived from the black hole masses in Table 2.1 and optical continuum luminosities from the portion of the light removed from the optical continuum images of the quasars by the PSF subtraction. The galaxy stellar masses are infrared continuum luminosities rescaled using mass-to-light ratios.

# Chapter 3

## Conclusions

We now know that the relationship between galaxies and their stellar populations is more complex than previously imagined, but the work presented here sheds some light on the interplay between the two.

In the KISS study, I dispel the idea that PAH emission is a simple tracer of star-formation rate. Mass-specific PAH emission shows very little relationship to mass-specific star-formation rate. Instead, the efficiency of PAH emission scales with galactic stellar mass. This may be a proxy for galaxy size or morphology, as some works indicate that PAH emission is strongest along the edges of star-forming complexes. Regardless of the physical cause, this calibration will aid in the use of PAH emission as an indicator of star-forming activity in a variety of environments because it makes a simple and straightforward connection between the observable PAH luminosity and star-formation rate.

Far-infrared  $24\mu\text{m}$  emission is a more direct indicator of star-forming activity. I show in Chapter 1 that mass-specific  $24\mu\text{m}$  emission does correlate with mass-specific star-formation rate. Because the physical relationship between star formation and the thermal dust emission that dominates the  $24\mu\text{m}$  band is not as severely complicated by particle destruction due to heating and ultraviolet light, one would expect this calibration to be more straight-forward.

Likewise, the host galaxies of quasars appear to be more complex than anticipated. I detect star-forming activity throughout the host galaxies, albeit at levels lower than expected. I find evidence for a narrow-line region in the center of the quasar with the highest Eddington Ratio, PG 0026+129. The finding that star-forming activity accounts for the bulk of the extended line emission in quasar host galaxies confirms the speculation in ? that the narrow-line region size to quasar luminosity relationship proposed in ? is not robust at the highest luminosities.

The lower-than-expected levels of star-forming activity seen in these quasar hosts, particularly in high Eddington Ratio objects, suggest that many of these objects are transitioning into E+A galaxies, like those described in ?, and have already passed the peak of their star formation. Because the target quasars were selected to be likely sites of star-forming activity, the finding of lower-than-expected star-formation rates suggests that the AGN quenching may be more efficient than previously suspected. This conjecture is supported by the presence of shocked gas in the four quasar hosts with the highest Eddington Ratios. From this evidence, quasar host galaxies appear to be

particularly violent environments.

Despite lower-than-expected star-formation rates, quasar host galaxies are extreme star-forming galaxies. In Figure 3.1, stellar mass-specific star formation rates are plotted against stellar masses for the KISS galaxies, the seven quasar host galaxies for which I have infrared data, and 318 galaxies from the The GALEX Ultraviolet Atlas of Nearby Galaxies (?). The KISS galaxies match the locus of nearby galaxies fairly well; although the KISS sample is more evenly selected, the KISS galaxies and the nearby galaxies from ? have in common that they are normal star-forming objects, so this results is not surprising.

In contrast to the KISS galaxies, five of the seven quasar hosts plotted in Figure 3.1 fall at the upper envelope of the distribution. This finding is significant in that the quasar hosts fall within the distribution of normal star-forming galaxies, suggesting that the processes of star formation in quasar hosts are not completely different, and also in that they are on the upper envelope of the distribution, indicating that they are extreme variants of star-forming galaxies. With a star-formation rate of over  $25 M_{\odot}/\text{yr}$ , PG 1626+554 may be a truly extraordinary object indeed, but, without infrared continuum photometry, it cannot be appropriately placed in Figure 3.1.

Further work in this area will continue to decode the complexities of star formation in different environments. While the KISS survey focused on infrared star-formation indicators in AGN-free galaxies, the infrared SEDs of AGN hosts are also of particular interest. Mid- and far-infrared maps of quasar hosts would allow us to access obscured star formation in this violent environment; ALMA or Herschel observations of these or similar objects may be of service. Using KISS as a reference sample of star-forming galaxies, I can easily put in context any future far-infrared observations of quasar host galaxies. Because the line-ratio diagnostics discussed in Section 2.8.1 indicate which portions of the quasar host galaxies are the sites of star-formation and which are irradiated by the central black hole, I can make direct comparisons between far-infrared observations of the star-forming regions of the quasar hosts and the AGN-free KISS galaxies. As seen in Figure 3.1, the quasar hosts have higher-than-typical mass-specific star-formation rates; it would be interesting to see if their far-infrared emission is also extraordinary. If so, it would suggest that the surplus star formation is occurring in the centers of dense and heavily enshrouded molecular clouds and, if not, it would suggest that the faster-than-average star formation of quasar hosts is a scaled up version of star formation in typical galaxies. Either way, that result would be significant to our understanding of the assembly of galaxies.

Likewise, the metallicities of the KISS galaxies will be a significant asset to my analysis of the quasar host galaxies once I have produced my own line-ratio diagrams with CLOUDY. Because metallicity spreads the locus of star-forming points in the line-ratio diagram along a track, seen in Figure 2.7 and discussed in Section 2.8.1, it will be possible to roughly estimate the metallicity of star-forming locations in the quasar host galaxies. I will then compare these metallicity estimates for the quasar host galaxies with metallicities of KISS galaxies with similar masses. Alternatively, I can compare the masses of the quasar host galaxies to those of KISS galaxies with similar metallicities; the metallicity information essentially gives me a second and very complementary way of relating these extreme objects back to normal star-forming galaxies. Because of its

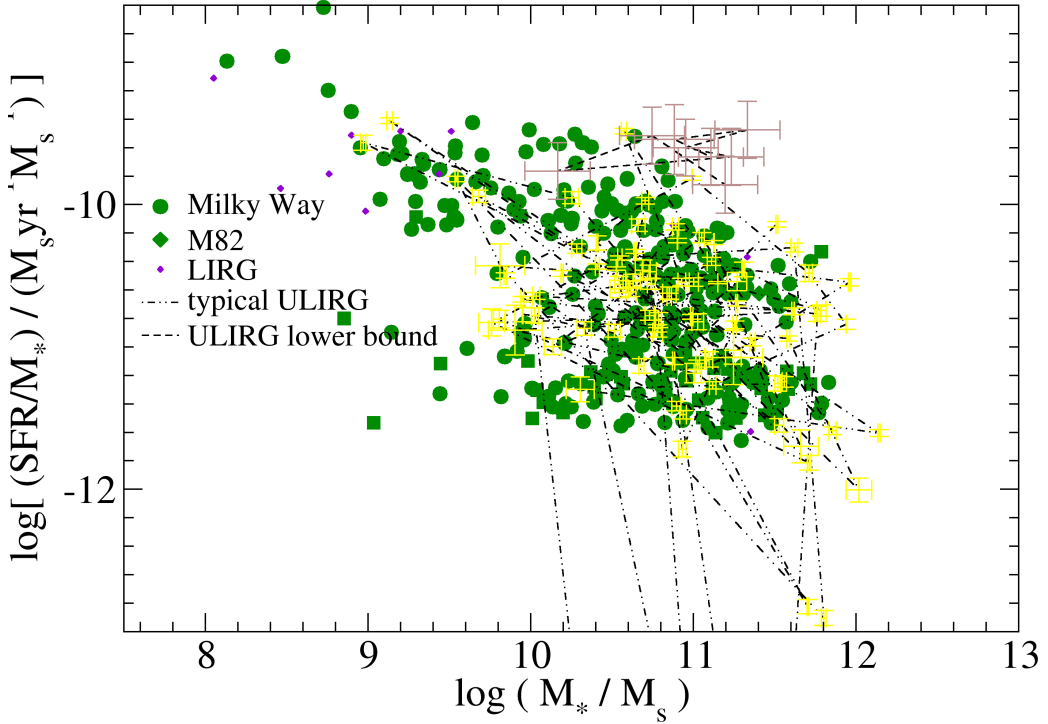


Figure 3.1: Stellar-mass specific star-formation rates vs. stellar mass for the quasar host galaxies (green), the KISS galaxies (red), and the The GALEX Ultraviolet Atlas of Nearby Galaxies (?) (black). The different morphological types of nearby galaxies are marked with different symbols. Note that the KISS galaxies fall on essentially the same area of the plot as the nearby galaxies, while the quasar hosts fall at the upper envelope of this area.

volume-limited collection method, the KISS sample is, by design, an excellent benchmark. These kinds of investigations will allow me to address questions such as: What kind of galaxies were the quasar hosts before the onset of central black hole accretion? Or, what kind of galaxies will they mature into when accretion ends? Putting these quasar host galaxies in context fits into the theme of assembling a chronology of the quasar epoch of a typical galaxy.

The assembly of a chronology of star formation is the ultimate goal of many of the works discussed here, especially my own. With that, our community can address broader issues about the assembly of galaxies and the star-formation history of the universe. Research like this also allows us to ask questions about our own Milky Way: Was it ever a quasar host? What were the stages that it went through? When we see starburst galaxies, are they analogs to an early Milky Way? In the work I present here I have investigated a representative sample of typical star-forming galaxies as well as a class of extreme objects; these investigations flesh out, in complementary ways, interesting aspects of the chronology of star-forming galaxies.

## Vita

### Jason Young

Jason E. Young  
525 Davey Lab  
University Park, PA 16802  
(814) 863-7948  
[jyoung@astro.psu.edu](mailto:jyoung@astro.psu.edu)  
[www.astro.psu.edu/~jyoung](http://www.astro.psu.edu/~jyoung)

---

### Research Expertise

- low surface brightness galaxies
- quasars / AGN
- star-forming and active galaxies
- optical, UV, near-, mid-, and far-IR photometry
- UV, optical, and near-IR spectroscopy
- computational/numerical analysis
- C, C++, Python, Java, IRAF CL, Bash

---

### Education

<b>Pennsylvania State University</b>	University Park, PA
Doctor of Philosophy in Astronomy and Astrophysics	December 2012
<b>University of Arizona</b>	Tucson, AZ
Bachelor of Science in Astronomy and Physics, minor in Latin	May 2005

---

### References

- Chris Palma, cpalma@psu.edu, (814) 865-2255, 525 Davey Lab
- Caryl Gronwall, caryl@astro.psu.edu, (814) 865-2918, 525 Davey Lab
- Michael Eracleous, mce@astro.psu.edu, (814) 863-6041, 525 Davey Lab
- Jane Charlton, charlton@astro.psu.edu, (814) 863-6040, 525 Davey Lab
- Donald Schneider, dps7@psu.edu, (814) 863-9554, 525 Davey Lab

---

<b>Research Experience</b>	
<b>Pennsylvania State University</b>	University Park, PA
<i>Researcher</i>	June 2013 - present
Principle Investigator on a program to determine the star-formation histories of low surface brightness galaxies.	
<i>Research Assistant/Associate</i>	August 2012 - June 2013
Search for close binary supermassive black holes using HST STIS and COS spectra of SDSS quasars.	
<i>Research Assistant</i>	May 2009 - August 2012
Detection and analysis of quasar host galaxies in WFPC2 and NIC-MOS images using narrow- and medium-band filters. Developed a novel technique to perform PSF subtraction on continuum and emission-line images of eight PG quasars. Using the emission-line residual images, star-formation rates and morphologies were estimated for each quasar host galaxy.	
<i>Research Assistant</i>	June 2005 - August 2012
Analysis of multi-wavelength properties of star-forming galaxies in the Kitt Peak International Spectroscopic Survey (KISS). Photometry of star-forming galaxies in the UV, optical, and near-, mid-, and far-IR was compared with star-formation rates in search of novel star formation rate indicators and bulk properties of star-forming galaxies.	
<i>Research Assistant</i>	May 2007 - May 2009
Detection and photometry of star-forming regions and dwarf galaxies in tidal debris and interacting galaxies in Compact Galaxy Groups using ACS images. Stellar evolution models were used to determine age and mass for each object.	
<b>University of Arizona</b>	Tucson, AZ
<i>Research Assistant</i>	September 2002 - May 2005
Helped discover twelve high redshift ( $z \approx 6$ ) quasars by following up photometric candidates from the Sloan Digital Sky Survey using near-IR photometry and spectroscopy.	

---

## Posters & Presentations

- Young, J. E., Eracleous, M., Shemmer, O., Gronwall, C., Netzer, H., Lutz, D., Sturm, E., & Ciardullo, R. “In Search of Star-Forming Regions in the Host Galaxies of Nearby Quasars” 2010, 215th AAS Meeting
- Young, J. E., Gronwall, C., Charlton, J. C., Durrell, P. R., Elmegreen, D., Gallagher, S. C., Johnson, K., & Chandar, R., “ACS Photometry of Tidal Debris in HCG 31” 2008, 211th AAS Meeting
- Young, J. E., Gronwall, C., Rosenberg, J. L., & Salzer, J. J., “Spitzer IRAC Observations

of Nearby Star-Forming Galaxies and Implications for Star-Formation Rates" 2007, 209th AAS Meeting

---



---

## Talks

- Young, J. E. "Quasar Host Galaxies: What's Really Going On?", lunch talk, Space Telescope Science Institute, January 2013
- Young, J. E. "Star Formation Across Galactic Environments", dissertation talk, Winter AAS Meeting, January 2013
- Young, J. E. "Quasar Host Galaxies: What's Really Going On?", lunch talk, Goddard Space Flight Center, December 2012
- Young, J. E. "Quasar Host Galaxies: What's Really Going On?", lunch talk, Cornell, October 2012
- Young, J. E. "In Search of Star Formation in Quasar Host Galaxies," Penn State departmental talk, Spring 2011
- Young, J. E., Eracleous, M., Gronwall, C., Shemmer, O., Netzer, H., Sturm, E., & Ciardullo, R. 2011, in Bulletin of the America Astronomical Society, Vol. 43, American Astronomical Society Meeting Abstracts 217, 421.04-+
- Young, J. E. "Quasar Host Galaxies: The Story of a Hidden Train Wreck," departmental talk, Fall 2009
- Young, J. E. "C++: Object Oriented Programming," Graduate Student Association presentation, Summer 2008

---



---

## Teaching Experience

### Pennsylvania State University

University Park, PA

*Lecturer*

August 2013 - present

Taught an introductory astronomy course focusing on the sky and planets as well as an astronomy overview course.

*Instructor*

August 2005 - August 2012

Taught four sections of an elementary astronomy laboratory for undergraduate non-majors.

*Rooftop Telescope Instructor/Operator*

August 2005 - Present

Taught a rooftop telescope activity for undergraduate non-majors.

*Teaching Assistant*

Fall 2010, Fall 2011

Assisted with the teaching of an advanced observational techniques course for undergraduate astronomy majors.

### University of Arizona

Tucson, AZ

*Telescope Operator*

August 2003 - May 2005

Operated the Steward Observatory telescope for introductory astronomy lab activities.

**Julia-Keen Elementary**

Tucson, AZ

*Tutor*

August 2002 - May 2004

Tutored local elementary school students in math and reading during in-class activities as well as after school.

**Professional Societies**

American Astronomical Society

2005 - Present

Graduate Women in Science (National Nomination Committee)

2010 - Present

Penn State Graduate Student Association (Vice President, Committee Chair)

2008 - 2011

**Outreach Experience****Flandrau Science Center**

Tucson, AZ

*Planetarium Console Operator*

2000 - 2005

Gave sky tours and operated planetarium.

*Planetarium Maintenance Assistant*

2003 - 2005

Performed technical maintenance of planetarium projection equipment.

*Science Education Assistant*

2002 - 2005

Performed science demonstrations and experiments for visiting groups.

*Telescope Operator*

2002 - 2005

Operated the 16-inch observatory for the general public.

**Pennsylvania State University**

University Park, PA

*Volunteer*

2005 - Present

- AstroFest, ~2,000 visitors/year, Volunteer & Organizer, 2005-2012
- Space Day / Exploration Day, ~1,000 visitors/year, Volunteer & Organizer, 2005-2012
- Astronomy Open House, ~200 visitors/year, Volunteer & Organizer, 2005-Present
- Shaver's Creek Environmental Center, Teaching Volunteer & Special Guest Lecturer, 2008-Present

*Night Sky Radio Program*

2008 - 2011

Weekly guest on a public radio program; provided night sky updates and viewing suggestions.